New Interaction Models of Ultra-high-energy Cosmic Rays from a Nuclear Physics Approach

DISSERTATION

zur Erlangung des akademischen Grades
doctor rerum naturalium
(Dr. rer. nat.)
im Fach: Physik
Spezialisierung: Theoretische Physik

eingereicht an der
Mathematisch-Naturwissenschaftlichen Fakultät
der Humboldt-Universität zu Berlin

von

M.Sc. Leonel Morejon

Präsidentin der Humboldt-Universität zu Berlin:
Prof. Dr.-Ing. Dr. Sabine Kunst

Dekan der Mathematisch-Naturwissenschaftlichen Fakultät:
Prof. Dr. Elmar Kulke

Gutachter: 1. PD Dr Walter Winter
2. Prof Dr David Berge
3. Prof Dr Giampaolo Cò

Tag der mündlichen Prüfung: 12. November 2020

Selbständigkeitserklärung

Ich erkläre, dass ich die Dissertation selbständig und nur unter Verwendung der von mir gemäß § 7 Abs. 3 der Promotionsordnung der Mathematisch-Naturwissenschaftlichen Fakultät, veröffentlicht im Amtlichen Mitteilungsblatt der Humboldt-Universität zu Berlin Nr. 42/2018 am 11.07.2018 angegebenen Hilfsmittel angefertigt habe.

Abstract

The origin of the ultra-high-energy cosmic rays (UHECRs) is still unknown. Photonuclear interactions of cosmic rays with astrophysical photons affect their observed spectrum and chemical composition, and produce other 'messengers', such as gamma-ray photons and neutrinos. A multimessenger approach is therefore essential to understand the processes behind the production of the UHECRs, and insights from nuclear physics are a crucial ingredient in building adequately accurate models to interpret this multimessenger data. This thesis presents models that will contribute with a cutting-edge approach to three aspects of high-energy astronuclear physics: photomeson production by cosmic-ray nuclei heavier than protons, gamma-ray emission from unstable nuclei created by the photodisintegration of cosmic rays, and the simulation of extragalactic propagation of nuclei heavier than iron (so-called superheavy isotopes). The photomeson model is the first in the literature to include results from nuclear physics that go beyond the simple principle of nucleon superposition. It provides a more accurate description of the inelastic cross sections, and the emitted spectrum of secondary particles, including secondary isotopes and neutrinos from pion decays. The model is implemented in a numerical software and applied to the simulation of two classes of sources: gamma-ray bursts and tidal disruption events. I show that compared to state-of-the art methods, the new model has a significant impact on the high-energy neutrino emission from these sources, and on the chemical composition of the emitted UHECRs. The second model deals with the emission of photons from decay and de-excitation of unstable nuclei, which are expected to be produced in photo-disintegration of cosmic rays due to interactions with astrophysical photons. To show the impact of the new model, it is deployed in a simulation of cosmic-ray interactions in the galaxy Centaurus A. While current literature proposes that very-high-energy gamma rays observed from this source can be explained by interactions of iron nuclei accelerated in the source, the spectrum obtained with our more realistic approach is actually too soft to explain observations. This shows that astrophysical systems involving high-energy nuclear interactions can display nuanced behavior that must be treated with sufficiently accurate models. Finally, I focus on the modeling of photodisintegration of superheavy nuclei, a topic that is not addressed in current phenomenological works on UHECRs. After developing this model, I have implemented it in an existing numerical code for extragalactic UHECR propagation. I show the first results of this implementation, which represent the first numerical simulation of superheavy cosmic ray propagation. By combining these results with analytical calculations, I illustrate some effects in the behavior of the cosmic-ray mass composition during their cosmological propagation. Finally, I discuss possible future applications of this technology to test a superheavy component in the observed UHECRs. A more detailed analysis of this phenomenon is left as an outlook for future developments, since it requires atmospheric air shower models that do not currently exist. The models developed in this work have been made publicly available as open-source software. The results of this thesis show that more realistic phenomenological models are essential in a new era of data-driven multimessenger astrophysics.

Kurzzusammenfassung

Der Ursprung der ultrahochenergetischen kosmischen Strahlung (UHECRs) ist noch unbekannt. Photonukleare Wechselwirkungen der kosmischen Strahlung mit astrophysikalischen Photonen beeinflussen ihr beobachtetes Spektrum und ihre chemische Zusammensetzung und erzeugen andere "Botenstoffe", wie Gammastrahlenphotonen und Neutrinos. Ein Multi-Messenger-Ansatz ist daher unerlässlich, um die Prozesse zu verstehen, die hinter der Produktion der UHECRs stehen, und Erkenntnisse aus der Kernphysik sind ein entscheidender Bestandteil bei der Erstellung angemessen genauer Modelle zur Interpretation dieser Multi-Messenger-Daten. In dieser Arbeit werden Modelle vorgestellt, die mit einem bahnbrechenden Ansatz zu drei Aspekten der Hochenergie-Astronuklearphysik beitragen werden: Photomesonenproduktion durch kosmische Strahlenkerne, die schwerer als Protonen sind, Gammastrahlenemission von instabilen Kernen, die durch die Photodisintegration der kosmischen Strahlung entstehen, und die Simulation der extragalaktischen Ausbreitung von Kernen, die schwerer als Eisen sind (so genannte superschwere Isotope). Das Photomesonenmodell ist das erste in der Literatur, das Ergebnisse der Kernphysik einbezieht, die über das einfache Prinzip der Nukleonenüberlagerung hinausgehen. Es liefert eine genauere Beschreibung der unelastischen Querschnitte und des emittierten Spektrums von Sekundärteilchen, einschließlich sekundärer Isotope und Neutrinos aus Pionzerfällen. Das Modell ist in einer numerischen Software implementiert und wird auf die Simulation von zwei Klassen von Quellen angewandt: Gammastrahlenausbrüche und Gezeitenzerstörungsereignisse. Ich zeige, dass das neue Modell im Vergleich zu den modernsten Methoden einen bedeutenden Einfluss auf die hochenergetische Neutrinoemission dieser Quellen und auf die chemische Zusammensetzung der emittierten UHECRs hat. Das zweite Modell befasst sich mit der Emission von Photonen aus Zerfall und Entregung instabiler Kerne, die bei der Photozertrümmerung der kosmischen Strahlung aufgrund von Wechselwirkungen mit astrophysikalischen Photonen entstehen dürften. Um die Auswirkungen des neuen Modells zu zeigen, wird es in einer Simulation der Wechselwirkungen der kosmischen Strahlung in der Galaxie Centaurus A verwendet. Während die aktuelle Literatur vorschlägt, dass die von dieser Quelle beobachtete sehr hochenergetische Gammastrahlung durch Wechselwirkungen von in der Quelle beschleunigten Eisenkernen erklärt werden kann, ist das mit unserem realistischeren Ansatz erhaltene Spektrum eigentlich zu weich, um die Beobachtungen zu erklären. Dies zeigt, dass astrophysikalische Systeme mit hochenergetischen nuklearen Wechselwirkungen ein nuanciertes Verhalten zeigen können, das mit ausreichend genauen Modellen behandelt werden muss. Schließlich konzentriere ich mich auf die Modellierung der Photodisintegration superschwerer Kerne, ein Thema, das in aktuellen phänomenologischen Arbeiten über UHECRs nicht behandelt wird. Ich habe dieses Modell in einen bestehenden numerischen Code für extragalaktische UHECR-Ausbreitung implementiert. Ich zeige die ersten Ergebnisse dieser Implementierung, die die erste numerische Simulation der superschweren kosmischen Strahlungsausbreitung darstellen. Indem ich diese Ergebnisse mit analytischen Berechnungen kombiniere, illustriere ich einige Effekte im Verhalten der Massenzusammensetzung der kosmischen

Strahlung während ihrer kosmologischen Ausbreitung. Schliesslich bespreche ich mögliche zukünftige Anwendungen dieser Technologie, um eine superschwere Komponente in den beobachteten UHECRs zu testen. Eine detailliertere Analyse dieses Phänomens wird als Ausblick auf zukünftige Entwicklungen belassen, da es atmosphärische Luftschauer-Modelle erfordert, die derzeit nicht verfügbar sind. Die in dieser Arbeit entwickelten Modelle sind als Open-Source-Software öffentlich zugänglich gemacht worden. Die Ergebnisse dieser Arbeit zeigen, dass realistischere phänomenologische Modelle in einer neuen Ära der datengesteuerten Multi-Messenger-Astrophysik unerlässlich sind.

List of publications

The following articles were published in connection with this dissertation.

Peer-reviewed publications:

- L. Morejon, A. Fedynitch, D. Boncioli, D. Biehl, and W. Winter. Improved photomeson model for interactions of cosmic ray nuclei. *Journal of Cosmology and Astroparticle Physics*, 2019(11):007–007, 2019a. ISSN 1475-7516. doi: 10.1088/1475-7516/2019/11/007. URL https://iopscience.iop.org/article/10.1088/1475-7516/2019/11/007

Contributions to projects currently in preparation:

- X. Rodrigues, L. Morejon, A. Rudolph, S. Gao, and W. Winter. (tentative author order) Nuclear gamma-ray emission from Centaurus A revisited with numerical models (working title). in development
- L. Morejon, J. Heinze, A. Fedynitch, and W. Winter. (tentative author order) Extragalactic propagation of super-heavy UHECR nuclei (working title). in development

Open-source software currently published online as a result of this work:

- L. Morejon. AstroPhoMes: Photomeson models for UHECR interactions with photons, 2019b. URL https://doi.org/10.5281/zenodo.2600177

Acknowledgments

The writing of this thesis would not have been possible without the help and support of a large number of people. Some of these contributors have been active, providing insights into the physics and professional advice, and many more in ways that have no relation to the field, but by providing the social grounding that helped me stay positive and focused on completing this task. With so many people helping me I am unable to mention each individually, but I thank you deeply and I apologize for not including you by name. Some of you are very special: you provided both scientific help and spiritual comfort; to those I dedicate my most profound gratitude – you will forever stay in my thoughts.

I have had the the opportunity to share my training as a PhD with many wonderful researchers, despite the reduced size of the group. This has been made possible Prof. Dr. Walter Winter, who also allowed me to pursue this work within this project. I need to thank the postdoc colleagues Denise Boncioli, Shan Gao, Andrea Palladino, Arjen van Vliet, and especially Anatoli Fedynitch who is a dear friend and supported me in many ways from the beginning, and continues to do so. Finally, I need to thank my PhD colleagues with whom I enjoyed very much sharing this period and who have helped me so much: Annika Rudolph, Jonas Heinze, Daniel Biehl, and very especially to Xavier Rodrigues because without his extensive contribution this task would have certainly been impossible. You have shown in all occasions to be a true friend and a great physicist, I hope to have the time to reciprocate all the time and support I have received from you, but for the moment I will repay you in jam sessions. I would also like to acknowledge Ana Krajinović who has been a great friend and a wonderful discussion partner for the really intellectual aspects that escape most of us. Thank you both for making me a part of your lives.

I want to thank especially Vasundhara Shaw and Annika Rudolph for their great help and concern for my situation, and for their advices and support with my unique problems as a foreign student.

I want to thank the hares Chun-Sung Yao, Daniel Biehl and Xavier Rodrigues, for awesome meals and drinks and amazing Mahjong games. I must admit I still don't understand the game, but I enjoyed the time immensely.

I want to dedicate this thesis to my grandparents, ñaña, abuelo, mima for spoiling me and for being proud even without reasons. I thank my sisters Yanet and Odelay for their support and love. I thank my dearest friend Alis who has always supported and cared for me when I needed

it the most, I can always count on you Osi. I want to thank Mami y Papi for their love and support, and the sacrifices you have made which I have come to understand with time.

I also want to thank all the members of ν **in town** because music is an inseparable fraction of me, and you made me extremely happy just by playing with you, even when I always misname the songs and lose the tempo.

During my work leading to this thesis, I was supported by the European Research Council (ERC) under the European Union's Horizon 2020 research and innovation program (Grant No. 646623)

List of Symbols

α_0 : Fine-structure constant.

A : Nuclear mass number.

B : Magnetic field intensity.

c : Speed of light in vacuum.

ϵ_r, ϵ_{CMB} : photon energy in the nucleus rest frame; the latter related to CMB photons.

ε' : Photon energy in the rest frame of an astrophysical source.

E, E_i, E_j : Cosmic ray energy (species denoted by index).

E_e : Electron energy in beta decay.

γ : Lorentz boost of cosmic ray species.

Γ_i : Interaction rate of species denoted by i.

Γ_i^{decay}, Γ_i^{esc} : Decay and escape rates respectively. Species denoted by i.

G : Lorentz boost for mass shells or jets in models of astrophysical sources.

J_A : Fluence of cosmic rays with mass A.

λ_i : Interaction length of cosmic rays for intergalactic propagation.

Λ : Disintegration distance for UHECRs propagating over cosmic distances.

Λ_D : Interaction length for Extended Air showers in units of depth.

L, L_e : Luminosity related to certain particles in astrophysical sources.

m_e, m_p, m_i : Rest mass of the electron, proton and particle species i respectively.

$n_\gamma = n_\gamma(\varepsilon_r)$: spectral number density.

$N = A - Z$: Nuclear neutron number.

N_i : Number density of particle species denoted by i.

Q_β : Decay energy in beta decay.

Q_i^{ext} : External injection of particle in radiation model.

$Q_{j\to i}$: Re-injection of particle j to particle i in radiation model.

R : Radius of astrophysical object, or radiation region in models of astrophysical sources.

r_0 : Classical electron radius.

R_Z : Magnetic rigidity.

σ_T : Thomson cross section.

$\sigma^{\rm bc}$, $\sigma^{\rm bd}$: Cross section; *boost conserving* and *broad distributed* interactions respectively.

$\sigma_{j\to i}^{incl}$: Inclusive cross section for particle j with production of particle i.

$\sigma_{\gamma p}$, $\sigma_{\gamma N}$, $\sigma_{\gamma A}$: Cross section of photonuclear interactions for protons, nucleons (average of proton and neutron cross sections) and a nucleus of mass A respectively.

$\sigma_{\langle X_{max} \rangle}$: Standard deviation of shower depth at maximum size.

θ : Pitch angle of photon in the rest frame of a cosmic ray.

τ_0 : Decay time of unstable nuclear species.

t'_{dyn} : Dynamical timescale of astrophysical source in its rest frame.

X : Slant depth for Extended Air showers.

$\langle X_{max} \rangle$: Mean value of shower depth at maximum size.

z : Cosmological redshift.

Z : Nuclear proton number.

List of Acronyms

AGN : Active Galactic Nucleus.
CMB : Cosmic Microwave Background.
EAS : Extensive Air Shower.
EBL : Extra-galactic Background Light.
EM : Empirical Model.
ENSDF: Evaluated Nuclear Structure Data File.
FOV : Field Of View.
GDR : Giant Dipole Resonance.
GRB : Gamma Ray Burst.
NRF : Nucleus‘ Rest Frame.
PAO : Pierre Auger Observatory.
PDE : Partial Differential Equation.
RDM : Residual Decay Model.
SED : Spectral Energy Density.
SNR : Super-Nova Remnant.
SPM : Single-Particle Model.
SRF : Source Rest Frame.
SSC : Synchrotron Self-Compton.
TDE : Tidal Disruption Event.
TRK : Thomas-Reiche-Kuhn.
UHECR : Ultra-High-Energy Cosmic Ray.
VHE : Very High Energy.

Contents

Chapter 1

Introduction

Cosmic rays are high-energy atomic nuclei of astrophysical origin. With energies up to some 50 joules[1] (Bird et al., 1995), cosmic rays travel almost at the speed of light, and are the most energetic form of radiation to be found in nature. In fact, their energy surpasses by up to a million-fold the most energetic gamma rays ever detected from the cosmos (Amenomori et al., 2019).

The existence of cosmic rays was established in the beginning of the 20th century with the measurement of radiation at different water depths by Pacini (1912), and at different heights in the atmosphere by Hess (1912). The observed increase in radiation levels with height pointed clearly to an extraterrestrial origin. Additionally, their solar origin was ruled out by observing that the profile of the radiation intensity was unchanged for daily or nightly measurements, as well as during a solar eclipse (Hess, 1912).

By the time V. Hess was awarded the Nobel Prize in 1936, the term *cosmic rays* was already in use, an estimate of their energy flux had been made, and the first evidence of their isotropy had been found (Regener, 1933). Soon after, Kolhorster et al. (1938) and Auger et al. (1939), among others, reported on the first observation of secondary particles from cosmic ray interactions in the atmosphere, now known as Extensive Air Showers (EASs, see *e.g.* Kampert et al., 2012). The detection of a cosmic ray event with energy above 10^9 GeV (Clark et al., 1961) and another one a few years later with energy 10^{11} GeV (Linsley, 1963) would lay the observational foundations to the physics of ultra-high-energy cosmic rays (UHECRs), a term that refers to those cosmic rays with energies above $\sim 10^9$ GeV.

Below energies of about 100 MeV, the Sun dominates the cosmic ray spectrum, as the solar winds effectively modulate the flux of cosmic rays arriving from beyond the Solar System (Ihongo and Wang, 2016). Above 100 MeV, Galactic sources dominate the observed cosmic ray flux over nearly ten decades in energy. The most plausible candidate source class for these cosmic rays are supernova remnants (SNRs, Blasi, 2013), which are large structures left after massive stars go supernova. At energies around 1 GeV, the elemental composition of Galactic cosmic rays

[1] As a comparison, 50 joules is about the kinetic energy of a a baseball thrown at 90 km h^{-1}.

resembles that of the Solar System, except for an excess of some unstable light elements which are produced in spallations of heavier nuclei in the interstellar medium. Above 1 GeV, the flux of CRs decreases steeply, reaching one particle per square meter per day at a few tens of TeV. Up to TeV energies, the flux is still sufficiently high to allow their direct measurement by satellite-based experiments, such as the now retired PAMELA mission (Adriani et al., 2011) and the AMS-02 experiment (Aguilar et al., 2013) on board the International Space Station.

At higher energies the cosmic ray flux continues to decrease as a power law with index between 2 and 3, and in the UHE regime, near the highest energies detected, this flux is reduced to 1-2 particles per day over the entire planet.

Due to this extremely low flux UHECR detection must be made indirectly, by measuring the properties of the EASs produced by cosmic ray interactions with the atmospheric air. On average, every UHECR interaction in the atmosphere leads to about 10^8 secondary particles that reach the ground (Anchordoqui and Soriano, 2019). As a means of comparison, this means that only one UHECR per day hitting the entire surface of the atmosphere yields a rate of secondary particles on ground level that is comparable to the average rate of precipitating raindrops [2].

As discussed in Chapter 2, these EASs are currently detected with a variety of methods, including the direct detection of charged secondaries using Cherenkov water tanks or scintillators, the detection of radio signals produced by the charge distributions created by the shower in the atmosphere, and the detection of the fluorescence light produced by the nitrogen molecules in the atmosphere that are excited by the passage of the charged secondaries. These signals are then used to reconstruct properties of the primary cosmic rays such as their energy, chemical composition and arrival directions.

The two major ground-based UHECR observatories currently in operation are the Pierre Auger Observatory (Aab et al., 2015b, Veberic, 2017, Unger, 2018), in Argentina, and the Telescope Array (Abu-Zayyad et al., 2013, Tokuno et al., 2012, Matthews, 2018), in the USA. In spite of the low UHECR flux, the large area covered by these experiments and their years of operation constantly provide new data, steadily reducing the uncertainties in the UHECR spectrum. However, more than a hundred years after their discovery, the precise chemical composition of the UHECRs is still disputed (Alves Batista et al., 2019c) and the more fundamental question of their origin remains largely unanswered.

From the theoretical point of view, Galactic sources like SNRs do not have the capability of accelerating cosmic rays up to the ultra-high energy regime, nor does the Galaxy have the necessary size or magnetic field strength to retain cosmic ray nuclei with those energies (Hillas, 1984, see also Chapter 2 where the bases of this argument are explained). We therefore expect that at ultra-high energies the sources of the cosmic rays must transition from Galactic to

[2] Assuming an annual precipitation in the whole planet of $\sim 10^5$ km^3 and a volume of 10^3 mm^3 per rain drop.

extragalactic. This seems to be confirmed by a recent observational result by (Aab et al., 2017) that shows a dipole anisotropy in the arrival directions of cosmic rays above 8 EeV, or 8×10^9 GeV, pointing away from the Galactic center.

Several classes of extragalactic objects seem to be able to power the UHECRs given their cosmological abundance and characteristic luminosities (Anchordoqui, 2019, Alves Batista et al., 2019c), such as gamma-ray bursts (GRBs), active galactic nuclei (AGNs) and starburst galaxies (see Chapter 2 for a review on these source classes). However, direct evidence in favor of any of these sources is difficult to obtain because cosmic rays, as charged particles, are susceptible to deflections by both extragalactic and Galactic magnetic fields, scrambling their arrival directions. This effect becomes less severe the higher the energy of the cosmic rays since their Larmor radius increases with energy. In theory, such effect could allow us to eventually pinpoint directly the sources of the UHECRs (Aab et al., 2018). However, the degree of diffusion depends strongly on the properties of the intergalactic magnetic field, which are still poorly known, and it remains a major challenge to this kind of direct detection.

Given the challenges in directly determining the direction of the UHECR sources, we must base ourselves on other observables, such as the spectrum and chemical composition, as indicators of the mechanisms behind their origin. This kind of study involves numerically simulating cosmic ray acceleration and interactions, and comparing the results of these simulations with observations, potentially constraining the underlying theoretical model.

As a recent example, Biehl et al. (2018b) studied cosmic ray emission by a population of GRBs and concluded that under certain conditions, the observed UHECRs can be explained by that class of objects. This kind of study includes a simulation of the interactions between the UHECRs and the photon fields that they encounter, both inside the sources, and during propagation in the intergalactic space.

Inside the source, these target photon fields may include thermal emission, for example from a kilonova (as in the recent GRB 170817A, Cowperthwaite et al., 2017) as well as non-thermal radiation emitted by high-energy electrons or by the cosmic rays themselves. After escaping the source, cosmic rays additionally encounter photon background fields that permeate the intergalactic space, such as the cosmic microwave background (CMB), leading to additional photointeractions. These interactions, both inside the sources and on the path to Earth, lead to energy losses of the UHECRs, and to their fragmentation into lighter isotopes. By simulating these processes, the predicted spectrum and chemical composition of the UHECRs arriving at Earth can be compared with experimental data in order to test the model.

Additionally, photointeractions can in some cases produce secondary meson particles, such as pions, which subsequently decay, emitting gamma rays and high-energy neutrinos. These additional "messengers" can also be used to constrain the source model (Section 2.1.3 provides

an overview of high-energy neutrino detection with the IceCube experiment (Aartsen et al., 2013), which has now been active for over a decade).

Obviously, this kind of phenomenological study relies heavily on an accurate description of the physics behind high-energy cosmic ray interactions, which affect their energy distribution, their composition, and the energy distribution of secondary particles produced. However, the phenomenology of high-energy photonuclear interactions currently relies on simplified models that reduce the accuracy of the predictions.

While we have a good understanding of the interactions of protons with photons (Mucke et al., 2000), current interaction models for nuclei are less accurate and they rely on simplified assumptions (Anchordoqui et al., 2008, Murase et al., 2008, Kalashev and Kido, 2015, Alves Batista et al., 2016). Moreover, the cross sections of crucial photo-nuclear processes have been poorly measured and in some cases their uncertainties have been shown to be large enough to impact astrophysical models (Boncioli et al., 2017).

At the same time, the importance of accurate nuclear interaction models has never been higher for the field of astrophysics, because we now have an unprecedented amount of data not only on UHECRs, but other related messengers like neutrinos and multi-wavelength radiation. The main objective of this thesis is to provide a more accurate description of the interactions of UHECR nuclei in order to improve UHECR modeling and the more general field of theoretical multimessenger astrophysics.

In this thesis I discuss the present methods for treating UHECR photo-nuclear interactions, and explain their limitations. I then present improved models that are beyond the current state-of-the-art, and explain in depth their underlying physics. For each model I also illustrate the effects of the improved accuracy in relevant astrophysical scenarios. One of these models has been deployed in a published study (Morejon et al., 2019a) that I have lead in collaboration with colleagues at DESY. Two other models are also discussed in this thesis, whose respective articles are currently in preparation (Rodrigues et al., in development, Morejon et al., in development).

The model developed in (Morejon et al., 2019a) is an improved model for photomeson interactions of nuclei, *i.e.* photointeractions that result in the emission of meson particles. This model is shown to reproduce experimental data more accurately than the state-of-the-art models, while preserving the ease of computation and flexibility.

The second project discussed in this thesis relates to the production of unstable isotopes through photonuclear interactions, and more specifically the photons that are emitted by the de-excitation of these unstable products. I introduce new models that improve on the current treatment of these processes, by combining compiled data and insight from nuclear physics. I show that these secondary photons from nuclear decay may actually play a role in explaining the high-energy emission from this source (Rodrigues et al., in development).

I will also discuss the possibility that UHECRs include a component of super-heavy elements, *i.e.* nuclei heavier than iron. In order to reconstruct the chemical composition of UHECRs based on experimental data, hadronic interaction models are required that so far have only included nuclei with masses up to iron-56 (Abreu et al., 2013, Kampert and Unger, 2012). I have extended current nuclear cross section tables to include nuclear species with masses up to lead, and then used those data to expand the software PriNCe (Heinze et al., 2019), a code for the simulation of extragalactic UHECR propagation. This is the first numerical study of UHECR propagation to include ultra-heavy elements (Morejon et al., in development).

After developing each model and applying it to an astrophysical case study, I have made them available to the community in the form of open-source software tools (Morejon, 2019b, currently available, additional modules in preparation). The purpose is to facilitate the usage of more accurate models by other astrophysics research groups, as well as to allow the reproducibility of the results presented here.

This thesis is organized as follows: in Chapter 2 I introduce the phenomenology and experimental detection of UHECRs and other cosmic messengers. A special emphasis is put on the current interpretation of the spectrum and the composition of UHECRs, which are some of the observables most directly impacted by the models that are discussed. I also present an overview of the most relevant astrophysical source classes that are discussed in later chapters in the deployment of the interaction models.

Chapter 3 introduces the physical interactions of UHECRs, with special emphasis on those improved by this work. I then briefly introduce some numerical codes that are used to simulate these interactions in astrophysical environments, and that are employed later on in this work for testing the interaction models, namely NeuCosmA (Hummer et al., 2010), AM^3 (Gao et al., 2017), PriNCe (Heinze et al., 2019) and CRPropa 3 (Alves Batista et al., 2016).

In Chapter 4 I discuss the novel nuclear photomeson interaction model (Morejon et al., 2019a). The impact of the model's improvements is shown in the context of specific astrophysical scenarios, where the simulation results are shown to to be sensitive to this more accurate treatment.

In Chapter 5 I focus on photon emission from unstable products of photodisintegration and I explain the details of the model I have developed. I then illustrate the impact of these processes in astrophysics using the case of Centaurus A, an active galaxy that has been widely studied in the literature. I show that these secondary photons from nuclear decay may actually play a role in explaining the high-energy emission from this source (Rodrigues et al., in development).

Chapter 6 is dedicated to the topic of UHECR propagation including the new interaction tables for ultra-heavy nuclei (Morejon et al., in development).

Finally, in Chapter 7 I summarize the main conclusions of this thesis and present an outlook into future developments of the work presented here.

Chapter 2

UHECR observations and origins

This chapter introduces basic experimental and theoretical elements to understand the origin, propagation and detection of UHECRs. Section 2.1 introduces the the experimentally accessible quantities and detectors related to UHECR and multimessenger astrophysics. Section 2.2 presents the candidate sources and the processes behind the synthesis, acceleration and propagation of UHECRs.

2.1 Phenomenology and detection

Multimessenger astrophysics employs the relations of high energy emissions from astrophysical objects to infer their properties. The emissions (messengers) include photons, neutrinos, UHECRs and gravitational waves. In Figure 2.1 the general concept of multimessenger astronomy is illustrated concisely. A source of UHECRs with enough power for acceleration will also radiate photons and neutrinos. The charged UHECRs, unlike the other messengers, are susceptible of magnetic deflections in their propagation towards Earth as well as other interactions which result in associated photons and neutrinos (cosmogenic neutrinos) (see Chapter 3). All these particles connected by the production mechanisms are referred to as cosmic messengers. Multimessenger astrophysics relies on these connections to provide a consistent framework of study for the origins of the messengers. Detection of such extremely energetic particles at Earth requires a multitude of detectors (high-altitude ground-based observatories, under-ground experiments, satellites, planes, globes, *etc.*). This section presents the detection methods of UHECRs (Section 2.1.1) and the other messenger particles (Section 2.1.3).

2.1.1 UHECR detection and observables

Cosmic rays of energy above 10^6 GeV penetrate the atmosphere and undergo a hadronic interaction with a nucleus of the medium, typically Nitrogen which makes up to 78% of the atmosphere. This first interaction produces a number of secondaries which in turn interact with other nuclei in the atmosphere producing more particles. This cascade of particles constitutes the phenomenon

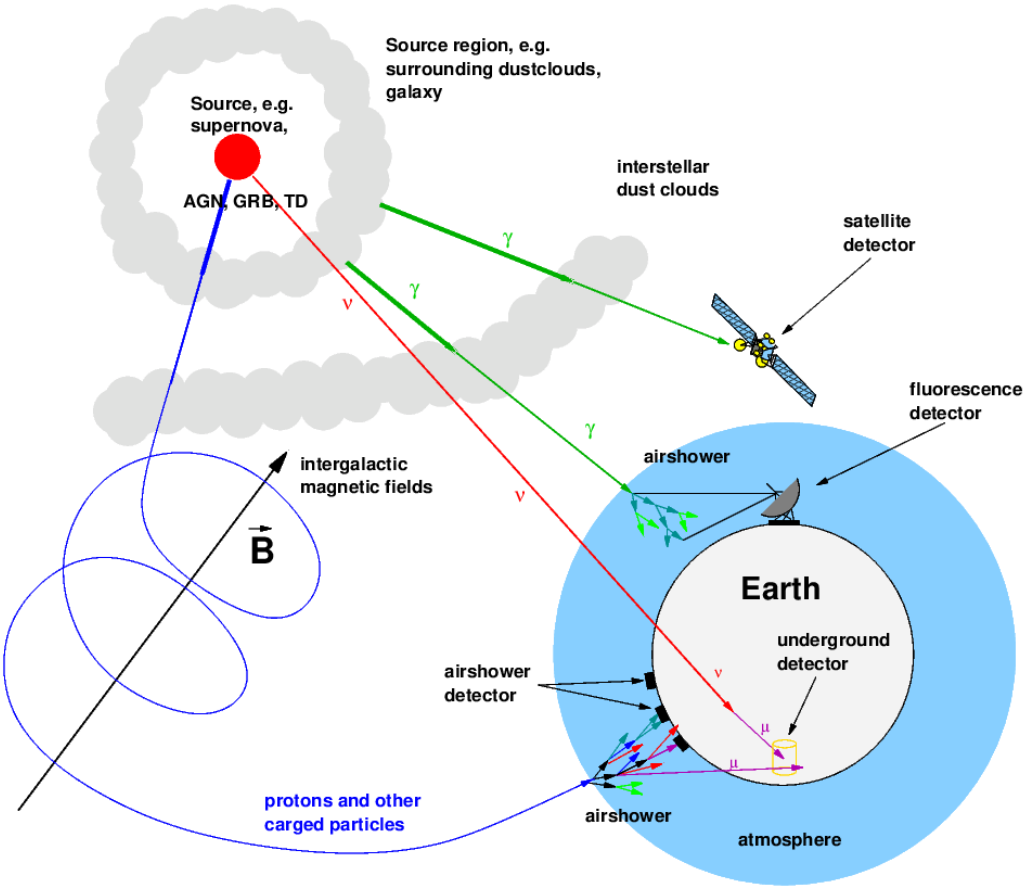

Figure 2.1: The multimessenger picture in one view. A powerful event (source) may produce several messengers (photons, neutrinos, UHECRs and gravitational waves) connected in their origin. Gamma rays, neutrinos and gravitational waves may arrive directly while UHECRs suffer magnetic deflections. At Earth, the messengers are detected with a variety of telescopes and other types of detectors. Source: Wagner (2005).

known as Extensive Air Shower (EAS) represented in Figure 2.2. As the number of particles produced increases, the mean particle energy decreases and the ionization losses dominate, leading to a decrease of particles in the shower. The ionization of the air molecules caused by the shower's particles is employed as a measure of the lateral shape of the shower. Using the features of the EAS as a proxy, the properties of the initial UHECR can be reconstructed.

The EAS developes with the depth along the direction of propagation defined by the incident particle (slant depth X). The number of particles vs slant depth $N(X)$ can be described by the

Gaisser-Hillas distribution,

$$N(X) = N_{\max} \left(\frac{X - X_1}{X_{\max} - X_1} \right)^{\frac{X_{\max} - X_1}{\Lambda_D}} \exp \frac{X_{\max} - X_1}{\Lambda} \tag{2.1}$$

which is represented in Figure 2.2 on the right. In this relation, X is the atmospheric thickness traversed by the shower, and it is the product of the distance crossed and the matter density. At 10^{11} GeV, a proton has an interaction length Λ of roughly $40\,\mathrm{g/cm^2}$, while for a nucleus it will be A-times larger (A being the nucleon number (Anchordoqui, 2019)).

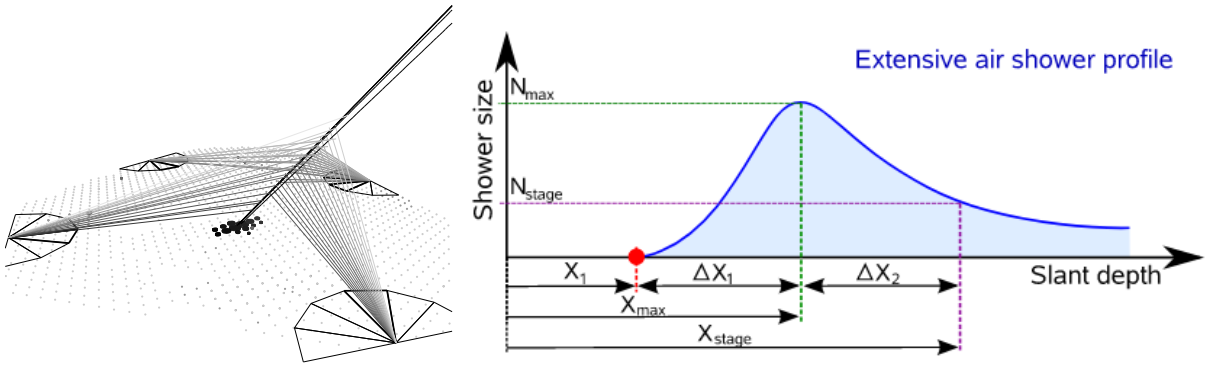

Figure 2.2: Extensive Air Shower represented schematically. On the left, an EAS event (dark lines) observed by PAO (dots and semicircles represent detectors, see text for details). On the right, the EAS particle number as a function of the slant depth X. The first interaction is signaled by a red dot, after which the number of particles grows rapidly with increasing depth reaching a maximum at depth $X_{\max}$. Figures reproduced from (Aab et al., 2015b)(left) and (Ulrich et al., 2009) (right).

The chain of interactions in an EAS is thus a sequence of stochastic events with variable number of secondaries produced per interaction. Therefore, there is an inherent uncertainty associated with EAS events, and many events are necessary to relate the EAS quantities to the properties of UHECRs. The total energy of the EAS is reconstructed from the collected particles through different methods. $\langle X_{\max} \rangle$ shows a dependence on the CR's energy and mass as $\ln E/A$ (Linsley and Watson, 1981) which is a fundamental component in determining the composition of UHECRs in addition to the shower variance $\sigma_{X_{\max}}$ (see Section 2.1.2).

The most important detectors of cosmic rays at the highest energies are the Pierre Auger Observatory and the Telescope Array.

The Pierre Auger Observatory (PAO)(Aab et al., 2015b) uses a hybrid detector to study cosmic rays above 10^{17} eV. PAO is located in Argentina, at an atmospheric depth of $875\,\mathrm{g/cm^2}$ (mean altitude $\sim$ 1400 m), and it has field-of-view (FOV) covering predominantly the southern hemisphere. The detectors are spread over an area of $\sim$ $3000\,\mathrm{km^2}$ as shown schematically

in Figure 2.2 (left). The portion of forward particles of the EAS (darker lines) that arrives at ground level is detected by the Surface Detector (SD). The SD is an array of water-tanks Cherenkov detectors represented in Figure 2.2 by lighter dots (passive detectors) and darker dots (active detectors). The lighter lines emanating from the EAS represent the fluorescence signal that typically accompanies the EAS, and which is collected by the Fluorescence Detector (FD). The FD are optical telescopes located at the center of the semicircles in the drawing, where the semicircles represent their angular coverage.

The Telescope Array (TA)(Abbasi et al., 2018) also uses hybrid detection methods similar to Auger with a limiting minimal energy of 10^{17} eV. TA is situated in Utah (USA) at a mean altitude $\sim$ 1400 m with a FOV covering predominantly the northern hemisphere, although there is an overlap with PAO's FOV. The surface covered by the SD is $\sim$ 700 km^2 and it is schematically very similar to the drawing in Figure 2.2 (left). However the SD array is composed of scintillation surface detectors which are more sophisticated and precise compared to Cherenkov detectors. The FD are composed of three optical telescopes (PAO employs four) also located in the periphery of the SD and overlooking the atmosphere above it.

2.1.2 Spectrum and composition of Ultra High Energy Cosmic Rays

The energy distribution of the UHECR flux at Earth has been established in very solid grounds. Figure 2.3 shows the measurements from a multitude of detectors located in different regions of the planet. Some important features of the spectrum are the changes of spectral index denoted as the "knee" (at $E \sim 10^{15.5}$ eV) and the "ankle" (at $E \sim 10^{18.7}$ eV). At energies below the knee, the CR flux follows a power law of the energy with index $\gamma \approx 2.7$.

While the knee and ankle point to clear changes in the flux, there is no agreement on their explanation. Some models of the knee relate it to the maximal acceleration achievable in supernova shocks (Kobayakawa et al., 2002), while others relate it to the limit of magnetic confinement of the Galaxy (Leaky Box models, Candia et al. (2003)). Interactions have also been used to explain the knee, either with target particles in the Galaxy (*e.g.* photons (Candia et al., 2002), relic neutrinos (Dova et al., 2001)) and more hypothetical atmospheric interactions which produce undetectable products (Kazanas and Nicolaidis, 2001, 2003).

For the ankle, an origin mechanism proposed is the transition of the UHECR flux from a galactic-dominated to an extragalactic-dominated contribution (Aloisio et al., 2012). There are alternative explanations (De Marco et al., 2003, Berezinsky et al., 2006a, Aloisio et al., 2007) attributing the ankle to the strong suppression of the proton component caused by the increase of losses due to interactions with the Cosmic Microwave Background (CMB) (see Section 3.1.1). However these seem disfavored because it would imply a violation of upper limits on the cosmo-

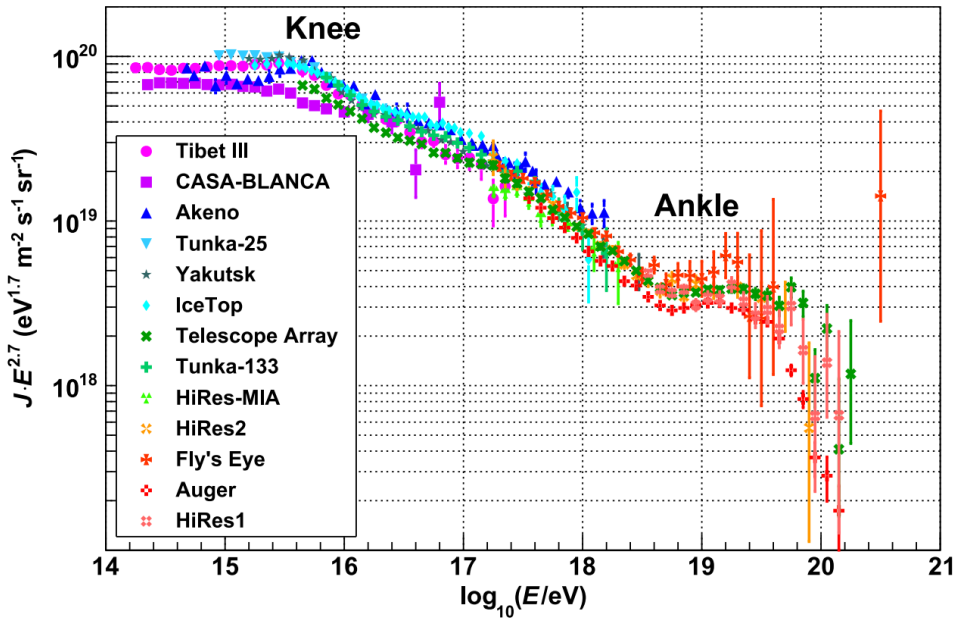

Figure 2.3: The spectrum of cosmic rays as measured by different experiments. The features of the spectrum where the index changes are indicated. At the highest energies there are some differences between the data from PAO and TA. Figure reproduced from (Abbasi et al., 2018).

genic neutrinos derived from measurements Heinze et al. (2016).

The extragalactic origin of UHECRs above certain energy has been argued from theoretical grounds (Hillas, 1984), pointing that no object in the Galaxy could magnetically confine protons up to the observed energies. Recent works provide additional elements: Abbasi et al. (2017) established a 1.5% limit on the galactic contribution to the UHECR flux at EeV energies; Aab et al. (2017) finds a dipolar anisotropy in the arrival direction of UHECRs, which is consistent with galactic deflections of a flux from extragalactic origin.

CR composition can be measured directly up to about 10^{14} eV where the event rate is still accessible for balloon-borne or satellite-borne spectrometers. For higher energies the composition must be inferred from EAS measurements from detectors like TA and PAO. The composition is usually inferred from the EAS using the mean and standard deviations of $X_{\max}$ ($\langle X_{\max} \rangle$ and $\sigma_{(X_{\max})}$, see Section 2.1.1).

Using hadronic models that simulate the interactions of UHECRs in the atmosphere, relations for the dependence of $X_{\max}$ and $\sigma_{(X_{\max})}$ on the UHECR's mass and energy are obtained (Aab et al., 2016). These relations can then be used to infer the primary UHECR's mass. Figure 2.4 shows the comparison of the measured values with model calculations assuming the UHECR

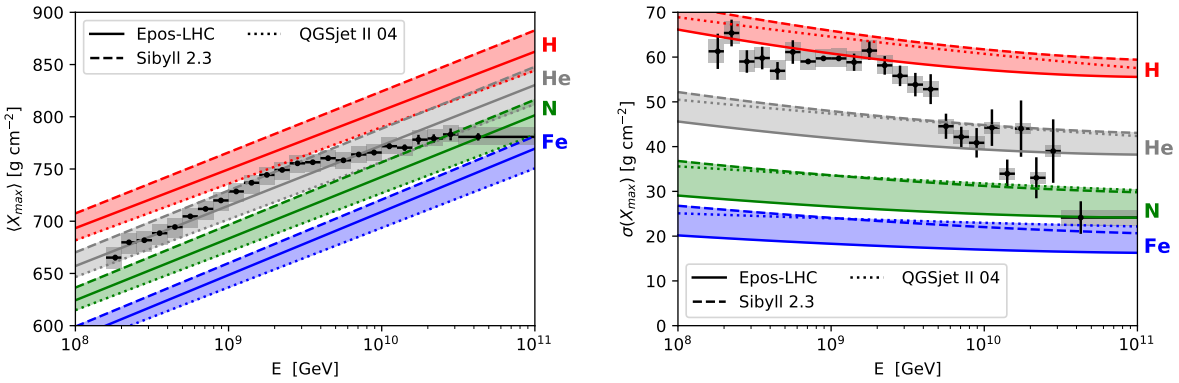

Figure 2.4: Hadronic models expectations of $\langle X_{\max} \rangle$ (left) and $\sigma_{(X_{\max})}$ (right) versus experimental data (Bellido, 2017b) obtained from hadronic interactions. The colors indicate the species assumed for single composition UHECRs, and the shaded area cover the range between the models with minimum and maximum values. Figures reproduced from Heinze et al. (2019).

is composed of a single mass. The different models show similar behavior with energy but present different offsets. Nevertheless, the data shows indications that the spectrum of UHECRs becomes heavier with increasing energies. $X_{\max}$ and $\sigma_{(X_{\max})}$ are related to the composition of the UHECRs employing relations obtained from through simulations of EAS. EAS simulations rely on interaction models based on LHC data, which reaches only to 10^{17} eV, hence the cross sections are extrapolated by several decades. (Aab et al., 2015a, 2016) found that hadronic interaction models are in disagreement with model-independent experimental observations from PAO. Additionally, the models have not been run for masses heavier than that of iron nuclei (A=56) and may produce potentially unphysical behavior for heavier nuclei (see Section 6.2). New detectors are currently being deployed to improve the measurement of the EM part of the EAS by improving the separation of muons and electrons, which would reduce the dependency of measurements on the interaction models.

Different studies attempt to explain the composition of the cosmic rays by making assumptions on the sources, the distributions, and the spectral index of the outgoing spectrum. Additionally they need to make assumptions on the interstellar medium mass density and Extra-galactic Background Light (EBL). For example in Aloisio et al. (2011) a two component model is used to fit the spectrum, with a rigidity dependent acceleration assumption, leading to a "disappointing" scenario where no multimessenger connection could be established.

2.1.3 Other messengers connected with UHECRs

Neutrinos Neutrinos of very high energies (VHE) are produced in interactions of UHECRs with photons both in the sources and through propagation. They are produced dominantly in the decay of pions which are the most common direct products of photomeson interactions of UHECRs (see Section 3.1). Neutrinos can also result from pions produced in hadronic proton-proton and proton-nucleus interactions. However, environments where such interactions are efficient require high matter densities which would limit the acceleration of UHECRs. Therefore, it is expected that the astrophysical neutrinos are produced in regions of low matter density and high photon density.

Neutrinos escape the production zones easily and are barely attenuated because of their low interaction cross sections. This means they directly point back to the sources over large distances. At the same time, their small interaction cross sections make neutrino detection difficult. Neutrino detection at the highest energies requires interaction volumes in the order of cubic kilometers. Neutrino detectors are commonly made of Digital Optical Modules (DOMs) that measure the Cherenkov radiation produced by the secondaries from a neutrino interaction with a nucleus in the instrumented transparent medium. Some neutrino telescopes like ANTARES (Ageron et al., 2011) and KM3NeT (Adrián-Martínez et al., 2016) use water as the active medium, while IceCube (Aartsen et al., 2017b) employs the continental ice in Antarctica.

IceCube reported the first measurement of high energy neutrinos of extraterrestrial origin (Aartsen et al., 2013). The flux reported corresponds to a spectrum with spectral index -2, ranging in energies from 30 TeV to 1.2 PeV. Since they are extremely relativistic, they could reach the Earth faster than other messengers, which means they can be used as a triggers for multimessenger events. Recently a 290 TeV neutrino was detected in coincidence with flaring photons consistent with the direction of the blazar TXS 0506+056 (Aartsen et al., 2018b). This coincident detection marked the first serious possibility of multimessenger studies of a source including neutrinos. Models of UHECRs imply predictions of the related neutrino fluxes which can be used to constrain them. For example, Aartsen et al. (2017a) established constrains on the production of UHECRs and neutrinos based on the weak correlation between neutrino events and observed GRBs.

Gamma rays Photomeson interactions of UHECRs also produce photons in addition to neutrinos, as decay products from mesons. These "hadronic" photons often carry a significant fraction of the energy of the UHECR, typically well beyond TeV. However, the opacity of most astrophysical environments to high energy photons is high, which causes them to cascade down to lower energies via photon-photon pair production. Additionally, the observed GeV-TeV photons

from most astrophysical objects can be explained by electron synchrotron and inverse Compton scattering (leptonic interactions). It is thus difficult to discern the hadronic photons (after cascading) from those produced by leptonic interactions. Dedicated radiation treatment modelling both the photomeson interactions subsequent cascading of photons are used to estimate the contributions from the leptonic and the hadronic components (Gao et al., 2017). However, in most cases large degeneracies in the parameter space mean that often the photon spectrum can be fit using only the leptonic component. When photons around TeV and above are detected, the purely leptonic models are severely constrained and hadronic components are often necessary, making such sources strong candidates for producing UHECRs. The search for hadronic signatures in the photon spectrum is part of the methods to identify UHECRs' source candidates. In Chapter 5, photons from nuclear decays are employed in explaining the highest energy photons from an AGN.

The photons from astrophysical sources are observed via a multi-wavelength campaign spanning more than 20 orders of magnitude in energy. Detectors employed include radio telescopes such as those forming the Very Long Baseline Array, X-ray telescopes such as Chandra, Swift and FermiLAT (Ackermann et al., 2012) measuring low energy gamma rays, and Cherenkov telescopes such as VERITAS (Weekes et al., 2002), H.E.S.S. (Hinton, 2004), MAGIC (Baixeras et al., 2004), and in the future CTA (Vercellone, 2014)) which measure Very High Energy (VHE) gamma rays.

2.2 UHECR nuclei origins: nucleosynthesis, acceleration and propagation

The measured composition of UHECRs does not allow for a precise determination of the species as discussed in Section 2.1.1. There is a considerable amount of studies that achieve a fit of the UHECRs spectrum by assuming different compositions, several including nuclei up to iron (*e.g.* Unger et al. (2015), Heinze et al. (2019)). The recent first-ever multimessenger measurements of a merger of neutron stars GW170817 (Abbott et al., 2017a) brought us first direct evidence of nucleosynthesis of heavy elements in this type of event. The almost certain possibility of forming a jet (Beniamini et al., 2019), and association to gamma-ray bursts, provides all the ingredients associated with UHECR acceleration, possibly with heavy nuclides as seeds.

This section presents some of the mechanisms believed to be responsible for the synthesis and for the acceleration of UHECR nuclei.

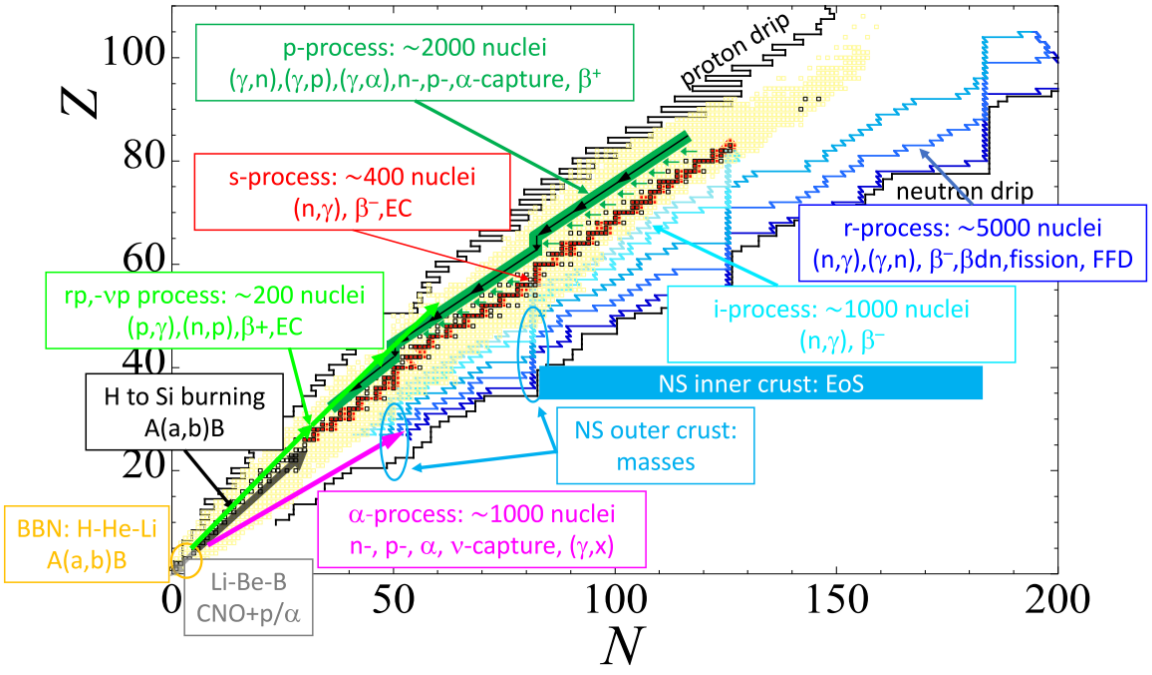

Figure 2.5: The nuclear chart with an overview of the processes proposed for the synthesis and the resulting nuclides. See the text for a discussion of the most important ones. Figure reproduced from Arnould and Goriely (2020).

2.2.1 Nucleosynthesis

The mechanisms for nucleosynthesis can be grouped as thermal and non-thermal. Thermal nucleosynthesis occurs in thermalized plasmas such is the case in the Big Bang (Big Bang Nucleosynthesis) and in the interiors of stars. Non-thermal nucleosynthesis refers to conditions non suitable for thermalization (*e.g.* too low density, too low temperature) as is the case of nuclei produced in spallations of Galactic CRs by interactions with the interstellar medium. The disintegration of UHECRs in photonuclear interactions could be considered an instance of such non-thermal nucleosynthesis, leading to unstable fragments that can only be explained through this mechanism (for example, unstable nuclides which could not propagate the astronomical distances from the sources before decaying).

Certain nuclei have been classified into s-, r- and p-nuclides according to the s-, r- and p-process proposed to explain their synthesis (see Figure 2.5). s-process consists of "slow" capture of neutrons in which stable seed nuclei incorporate neutrons at a rate comparable to beta decays, producing nuclei with a balanced neutron to proton ratio. In the r-process, the neutron capture occurs faster than the beta decays which leads to nuclei enriched with neutrons, located towards

the neutron drip line. The neutron drip line is a limit line in the Z-N diagram where nuclear forces cannot prevent nucleons from escaping the nucleus, hence denoting the neutron number limit for each given proton number. Finally, p-process referred initially to proton captures leading to proton-rich nuclei near the proton drip-line, but it is currently attributed to the photodisintegration process of s- and r-nuclides.

Most stars produce nuclei up to certain mass number which is limited by the star's total mass. Young stars' composition is dominated by hydrogen and helium produced in the Big Bang Nucleosynthesis, and in the course of their lives nuclear reactions consolidate nuclei into heavier species (*i.e.* increasing their metallicity). The stellar nucleosynthesis occurs as nuclei fuse and decay in thermal conditions, giving rise to different "burning" stages (H-burning, He-burning, C-burning, *etc.*). Low to intermediate mass stars ($0.8 - 10 M_{\odot}$) are the most abundant and exhibit a large diversity of nucleosynthesis. The largest changes in composition occur when they reach a late stage in their evolution, known as asymptotic giant branch (AGB). Many observations have detected an enrichment of s-process elements in the surfaces of low-mass AGB stars ($M < 3 M_{\odot}$) implying in-situ synthesis (Arnould and Goriely, 2020). Such nuclei include masses much heavier than iron, (*e.g.* Zr, Y, Sr, Ba, and even Tc, Karakas and Lattanzio (2014)). The interstellar medium is enriched with these nuclei as they are carried away by stellar winds and strong outflows which can produce mass loss rates between $10^{-7} - 10^{-4} M_{\odot}/y$. Additionally, s-process nucleosynthesis could also take place in AGB stars with heavier masses ($3 - 8 M_{\odot}$(Shingles et al., 2015)) as well as in massive super-AGB stars (Doherty et al., 2017).

The r-process is credited for the production of most of the stable nuclei and neutron rich nuclei heavier than iron. The r-process is related to neutron fluxes larger than $10^{20}\,\mathrm{cm}^{-3} s^{-1}$ which restrict the possible production sites to a few extreme scenarios such as neutron star (NS) mergers and neutron star-black hole mergers. Simulations have shown that shock acceleration and tidal stripping can take away $10^{-3} - 10^{-1} M_{\odot}$ in a duration comparable to the dynamical timescales. The subsequent stages of these mergers (a hot transient hypermassive NS (Baumgarte et al., 2000), followed by a stable supermassive NS, or a black hole-torus system), will further lose mass through outflows (Perego et al., 2014, Siegel et al., 2014).

Simulations of growing sophistication have confirmed that the ejecta from NS mergers are viable strong r-process sites up to the third abundance peak and the actinides (Roberts et al., 2011, Wanajo et al., 2014). During the dynamical phase of the merging scenario, the high number of free neutrons leads to production of heavy fissioning nuclei (transuranics) (Bauswein et al., 2013). The ejected mass of r-process material can account for most of r-nuclides in our Galaxy if the predicted event rate holds (around $10\,\mathrm{My}^{-1}$, Dominik et al. (2012)). The recent multimessenger measurements of a NS-NS merger (Abbott et al., 2017a) and associated gamma ray burst GRB170817A, have confirmed r-nuclide presence (Drout et al., 2017, Pian et al., 2017,

Watson et al., 2019)

Additionally, models of different types of supernovae (SNe) have been found to produce and eject neutron-rich nuclei heavier than iron and up to cadmium (Wanajo et al., 2011, 2018). A special case are collapsars which are highly magnetized stars whose SNe are believed to produce long gamma ray bursts and jets. r-nuclide production in collapsars is associated to the jets (Nishimura et al., 2015) and/or to the accretion disk after the black hole is formed (Halevi and Mösta, 2018, Siegel et al., 2019).

Models of AGB stars of different metallicities have also found efficient production of p-nuclei in the range A=90-208 (Goriely and Mowlavi, 2000). p-nuclei are also produced in all types of supernovae Kroupa et al. (1993) which are expected to accelerate cosmic rays. Additionally p-nuclei are produced in pre-SN stages and they have been found to survive the explosion in several cases (Rauscher et al., 2002)(Langanke et al., 2019).

2.2.2 Acceleration and candidate sources

The mechanism responsible for the acceleration CRs to ultra-high energies is not known, although theoretical insights are available. The acceleration of cosmic rays may occur rapidly through extended electrical fields or more slowly via multiple collisions with shocks of magnetized plasmas.

The acceleration via electrical fields generated by varying magnetic fields were first proposed by Swann (1933) considering electrons acceleration in Sun spots. This mechanism has been considered in detail in compact magnetized objects such as white dwarfs, neutron stars and black holes (*e.g.* for UHECR acceleration in neutron stars see Blasi et al. (2000), Fang et al. (2012)). This mechanism has the advantage of being fast but the high energy density characteristic of such environments might lead to energy losses that considerably reduce the acceleration efficiency.

Acceleration by shocks of magnetized plasmas were considered for the first time by Fermi (Fermi, 1949, 1954). This type of acceleration occurs progressively in consecutive stochastic encounters, thus the particles need to be confined to the acceleration region via magnetic fields. The size of the acceleration region along with the magnetic intensity can provide constraints or plausibility conditions for the acceleration potential (see Figure 2.6). The confinement is estimated comparing the particle‘s Larmor radius to the size of the acceleration region. The maximal rigidity R_Z (energy to charge ratio) that can be reached in a source class can be estimated from the characteristic size R and magnetic field B as $R_Z = E/Z = BR$ (Hillas, 1984). Lines with negative slope in Figure 2.6 represent constant rigidity values, *i.e.* the further from the origin the larger values of maximal rigidity. Astrophysical objects on the same line can accelerate to comparable rigidities. The yellow lines in Figure 2.6 represent the rigidities

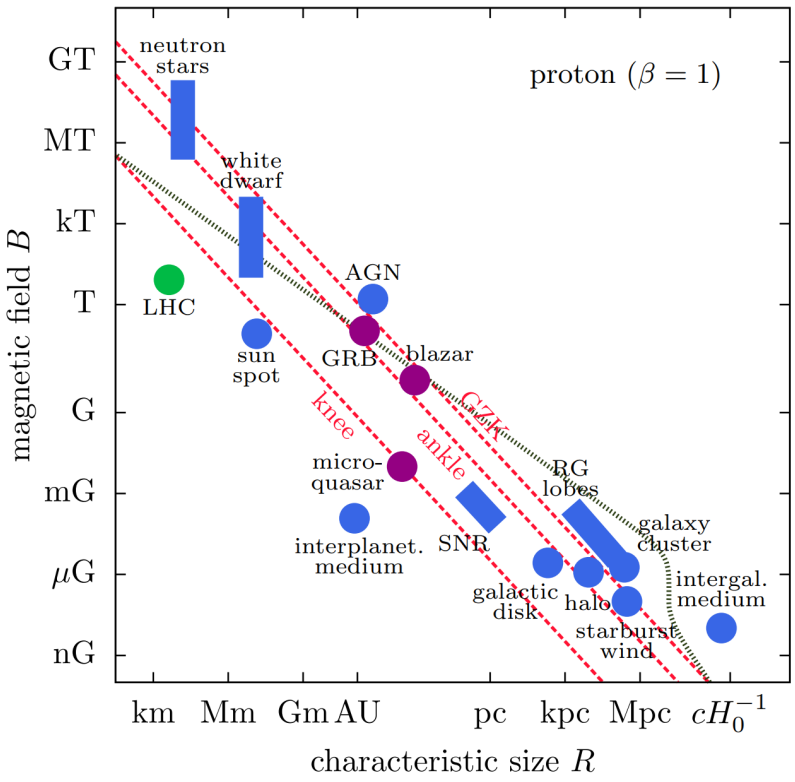

Figure 2.6: Hillas plot representing plausible sources in terms of acceleration capabilities. The yellow lines represent constant rigidity values, the knee ankle and GZK correspond the proton rigidity for those features in the UHECR spectrum. The sources are represented by colored shapes covering the areas of rigidity where they can exert acceleration. Figure reproduced from Aartsen et al. (2018a).

corresponding to the landmarks of the UHECR spectrum. Different acceleration regions and source classes are represented by labeled shapes showing there are plenty of classes that meet this necessary condition.

The diffusive shock acceleration mechanism proposed by Fermi (Fermi, 1954) is commonly considered because it naturally obtains the power law behavior observed in cosmic ray spectra. This is known as Fermi First Order Acceleration because the fractional energy gain is proportional to the first order of the plasma velocity.

In reality, acceleration is likely more complex since it depends on the power law structure of the magnetic field of shocks. The power law index of the CR spectrum is related to the acceleration process, and real scenarios might lead to energy dependent indices as different mechanisms could occur at different energy scales. Magnetohydrodynamics simulations are used

widely for studying instabilities in plasmas and their effects on the CR spectrum. On the other hand, the non-linear effect of the energy losses needs to be kept in mind since they are not native to magnetohydrodynamics simulations. Mastichiadis et al. (2020) shows that extreme losses can occur in super-critical conditions defined by the magnetic field and radius of the source. The physical reason is that photon and electron-positron pairs produced in UHECR losses contribute as target for interactions causing further interaction losses. These feedback losses effectively limit the maximal energy that can be achieved by the accelerated particles.

Other mechanism proposed is the "Espresso" mechanism (Caprioli, 2015) where particles from other regions enter the jet and receive a "one-shot" acceleration proportional to the square of the jet‘s Lorentz boost.

Candidate sources of UHECRs

Although there is currently no consensus on the origin of UHECRs, there is indirect evidence that certain source classes reunite the conditions for the synthesis and acceleration of UHECRs nuclei. The main candidate source classes for the origin of UHECRs are the following:

Active Galactic Nuclei (AGNs) are types of galaxies which have a strong activity in their central region, as evidenced by the presence of relativistic jets of plasma reaching up to 100 kpc (Osterbrock, 1989). The massive blackhole in such regions may develope a hot disk of accreting matter and a surrounding dust torus. The time variability of their electro-magnetic emissions is known to vary in ranges of days to months. Some of the closest AGNs are Markarian (Mrk) 421 and Mrk 501 which are at distances of 133 Mpc and 140 Mpc respectively. There is a wide diversity of The electro-magnetic Spectral Energy Density (SEDs) emitted, which may span several orders of magnitude (from meV to GeV-TeV energies) depending on the relative emissions from its components. Jetted AGNs have been proposed as possible sources of UHECRs given their abundance and typical luminosities. This is supported by recent indications of correlation in arrival directions of UHECRs and extragalactic sources of gamma rays, including AGNs (Aab et al., 2018). The possibility of a common origin of neutrinos and UHECRs protons had been studied (Stecker et al., 1991, Murase et al., 2014, 2012, Gao et al., 2017), while the inclusion of nuclei up to iron in a consistent method has been achieved more recently (Rodrigues et al., 2018). In Chapter 5 the photons from nuclear disintegrations are considered and examined in the context of a explaining the very high energy photons from nearby AGN.

Gamma Ray Bursts (GRBs) are bright bursts of gamma rays whose origin can be associated to multiple astrophysical events. They are believed to originate in relativistic jets powered by a black hole or a magnetized rapidly rotating massive star. Long duration GRBs have been

associated with the collapse of massive stars (Zhang et al., 2003, Mizuta and Ioka, 2013) and short duration GRBs with NS-NS mergers (Murguia-Berthier et al., 2014, Nagakura et al., 2014). In the case of the latter, the association was successfully verified in the recent GW170817/GRB 170817A events (Geng et al., 2019). The potential of GRBs as sources of UHECRs has been investigated in several works (Murase et al., 2006, Waxman and Bahcall, 1997, Boncioli et al., 2019, Biehl et al., 2018a). A similar treatment as in (Biehl et al., 2018a) was employed in studying the impact of UHECR interactions in this thesis (see Chapter 4).

Tidal Disruption Events (TDEs) are disruptions of stars by the tidal forces of companion black holes. Roughly half of the mass from the disrupted star remains in orbit forming an accretion disk, and it is expected the formation of a jet has for sufficiently large accretion rates (Lacy et al., 1982, Rees, 1988). The nuclei present in the disrupted star are thus extracted and can be accelerated by the jet, possibly reaching ultrahigh energies if the acceleration is more efficient than disintegration and other losses (see Chapter 3). The potential of TDEs as sources of UHECRs protons has been investigated in several works (Farrar and Piran, 2014, Alves Batista and Silk, 2017, Zhang et al., 2017) including the corresponding contribution to neutrinos (Wang and Liu, 2016). Biehl et al. (2018d) developed a TDE model with inclusion of nuclei, employing a simplified model for the production of neutrinos. In Chapter 4 this framework is employed to illustrate the impact of an improved model for production of neutrinos developed in this thesis.

Chapter 3

Interactions of UHECR nuclei: physical background and numerical implementation

In the previous chapter, the phenomenology and detection of cosmic rays and related messengers were introduced. The multimessenger connections hold for environments where matter-matter interactions are subdominant compared to photon-photon and matter-photon interactions. This chapter introduces the fundamental interactions of CRs in such conditions.

In Section 3.1 the physical processes of relevance for the intergalactic transport and in-source evolution are mentioned. Following, in Section 3.2, the fundamental equations for the transport and interactions for CRs in the mentioned environments are introduced. A brief description of the relevant codes employed is also included, with emphasis on the quantities that are affected by the new models in this thesis.

3.1 Photo-interactions of nuclei in astrophysics

This section is divided in two parts: Section 3.1.1 discusses processes and photo-interactions of nuclear and hadronic nature whose improved treatment is the focus of this thesis. Section 3.1.2 introduces electromagnetic interactions, which are not the main topic of this work but which co-occur in astrophysical contexts, and are therefore crucial to understand the applications of the models.

3.1.1 Photonuclear interactions and decays

The physical processes relevant for describing CR nuclear transformations in low matter density environments generally involve *(a)* interactions with surrounding photons, and *(b)* spontaneous nuclear decays. The following discussion addresses all nuclear species up to nucleon number $A = 208$ (*i.e.* ^{208}Pb). This includes elements heavier than iron-56 ($A > 56$), because these will be the subject of Chapter 6, although state-of-the-art works consider only UHECR nuclei with mass number up to 56.

Nuclear decays

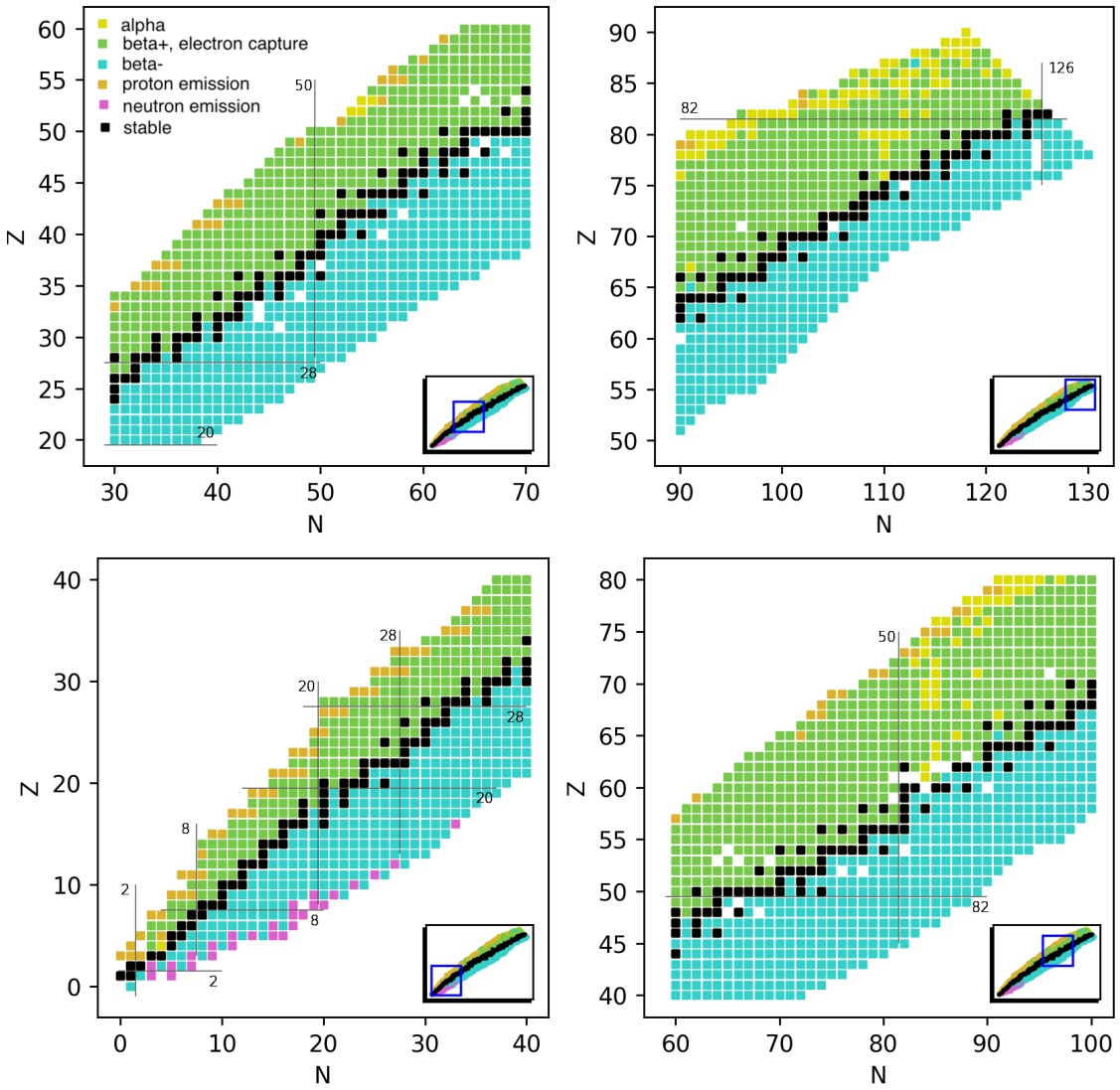

Figure 3.1: Dominant nuclear decay channel (indicated by the box color) of nuclides with mass up to lead-208. The nuclides are identified by their number of protons (atomic number Z) and neutrons (N). Stable elements are shown in black. Data as reported by Audi et al. (2017), Huang et al. (2017), Wang et al. (2017).

When studying photo-interactions of UHECR nuclei, both stable and unstable nuclides need to be considered. Stable nuclides will only change their species through photonuclear interactions leading to disintegrations. Instead, unstable nuclei may disintegrate spontaneously without

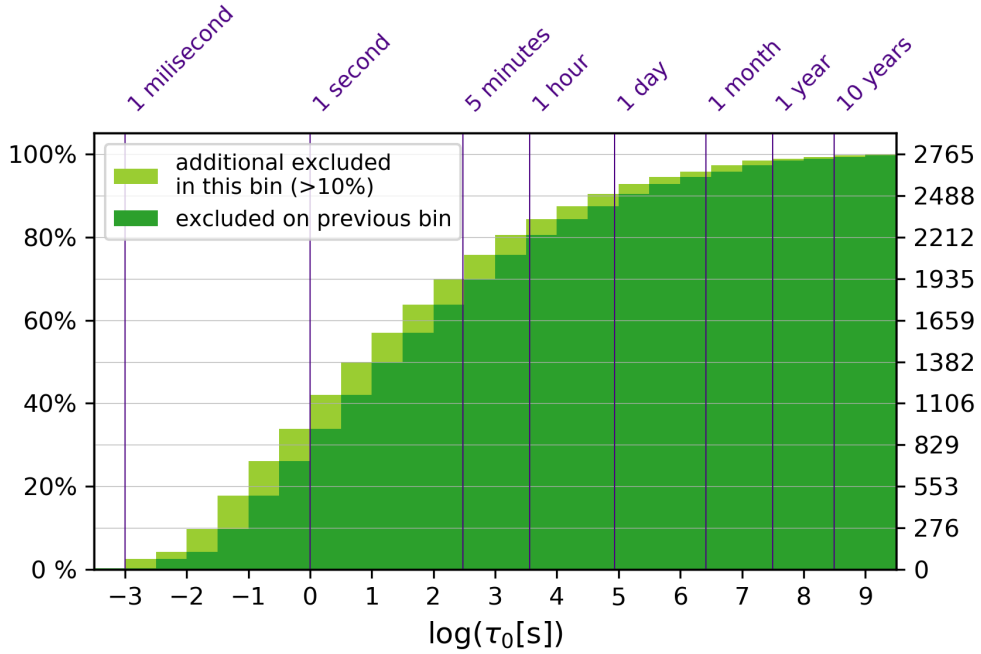

Figure 3.2: Cumulative histogram nuclear species and isomers sorted by the their proper decay times τ_0 given in seconds, as reported in the Atomic Mass Data Center data files (Wang et al., 2017, Huang et al., 2017) (2765 in total). For a given astrophysical system, the species whose decay time is much lower than other competing processes can be integrated out rather than treated explicitly in the differential equations. Thus, for any given lifetime threshold, the histogram shows the number of isotopes that can be excluded from the explicit simulation.

interacting, also producing secondary particles. In general, these unstable nuclei can be the products of photonuclear interactions when the incident photon has sufficient energy to either excite or to break up the target nucleus, which is why photo-interactions and decays are two connected processes.

Figure 3.1 shows the main form of decay for each nuclide considered in this work. It should be noted that some nuclides exhibit more than one form of decay with different probability. The decay products include protons, neutrons, α particles, larger nuclear fragments, photons, neutrinos, electrons and positrons, all of which make these processes relevant for multimessenger astrophysics.

Figure 3.2 shows the nuclide cumulative distribution as a function of proper mean lifetime τ_0. From a total of 2765 nuclides, 132 do not have a reported value (and are excluded here) and 255 are reported as stable. Depending on the dynamical timescale $t'_{\rm dyn}$[1] of the astrophysical

[1]Throughout this thesis, when discussing astrophysical sources, we will follow the convention that primed quan-

system (which typically gives an order-of-magnitude estimate of the timescale of the relevant interaction processes), the number of species explicitly considered in a numerical simulation can be reduced according to their decay time. Namely, the nuclides whose lifetime in the source rest frame (SRF, see footnote 1) is much shorter than the dynamical timescale of the system can be excluded from the explicit simulation ($\gamma\tau_0 \ll t'_{\rm dyn}$, where γ is the Lorentz factor of the nucleus). This reduces computation time because these short lived nuclei are replaced by their decay products directly instead of computing explicitly their photo-interactions (Boncioli et al., 2017). Applying such a decay time cut means drawing a vertical line in Figure 3.2 and thus the number of excluded / included nuclides is obtained. For example, Biehl et al. (2018b) modeled UHECR interactions in GRB shocks, whose estimated light-crossing time was ~ 1 s. A cutoff at $\tau_0 = 10^{-10}$ s excludes nuclei whose decay time in the SRF is shorter than the dynamical timescales of the GRB even at the highest energies $\gamma_{\rm max} \sim 10^9$ ($\gamma_{\rm max}\tau_0 < 1$ s).

In Figure 3.3 the decays are represented in a Segrè chart, where each nuclide represents a dot, and its color represents the mean lifetime. This representation is useful to appreciate large scale regularities. The stability line, is the imaginary line suggested by the arrangement of stable nuclei in the chart. The longer-lived nuclides are concentrated along the 'stability valley', which is the area closely surrounding the stability line. The pairs of Z and N numbers indicated along the diagram are the nuclear magic numbers, which correspond to the neutron and proton numbers associated with maximal stability. Nuclei with such numbers are often stable or longer lived than their neighbors. This phenomenon is understood in the shell model of nuclei by the closing of shells Greiner and Maruhn (1996), analogous to the electron shells in atoms. The mean lifetimes decrease as we move away from the stability valley in the direction of isobars (lines orthogonal to the stability line).Therefore, applying a cutoff on the minimum lifetime means narrowing the area in the chart of included nuclei to a region englobing the stability line.

The nuclear decay processes considered can be described as follows:

β-decay The transformation of one of the nucleons in the nucleus mediated by the weak interaction, leading to the production of charged and a neutral lepton. This includes β^--decay (Eq. 3.1) and β^+-decay (Eq. 3.2). In this process the total nucleon number does not change and the nuclear mass changes only by an amount corresponding to the released energy, which is in general a small fraction of the total rest mass.

tities refer to the value given in the source rest frame (SRF), in contexts where it is necessary to explicitly distinguish it from the observer's frame. In a particle physics experiment, the SRF would be equivalent to the lab frame; in the case of an astrophysical outflow, such as an AGN jet or an internal shock in a GRB, the SRF refers to the rest frame of the outflowing plasma where the interactions take place. In the general case of an outflow in a source located at redshift z viewed with a Doppler factor δ (*cf.* Section 2.2.2), the energy transformation is given by $E = E'\delta/(1+z)$.

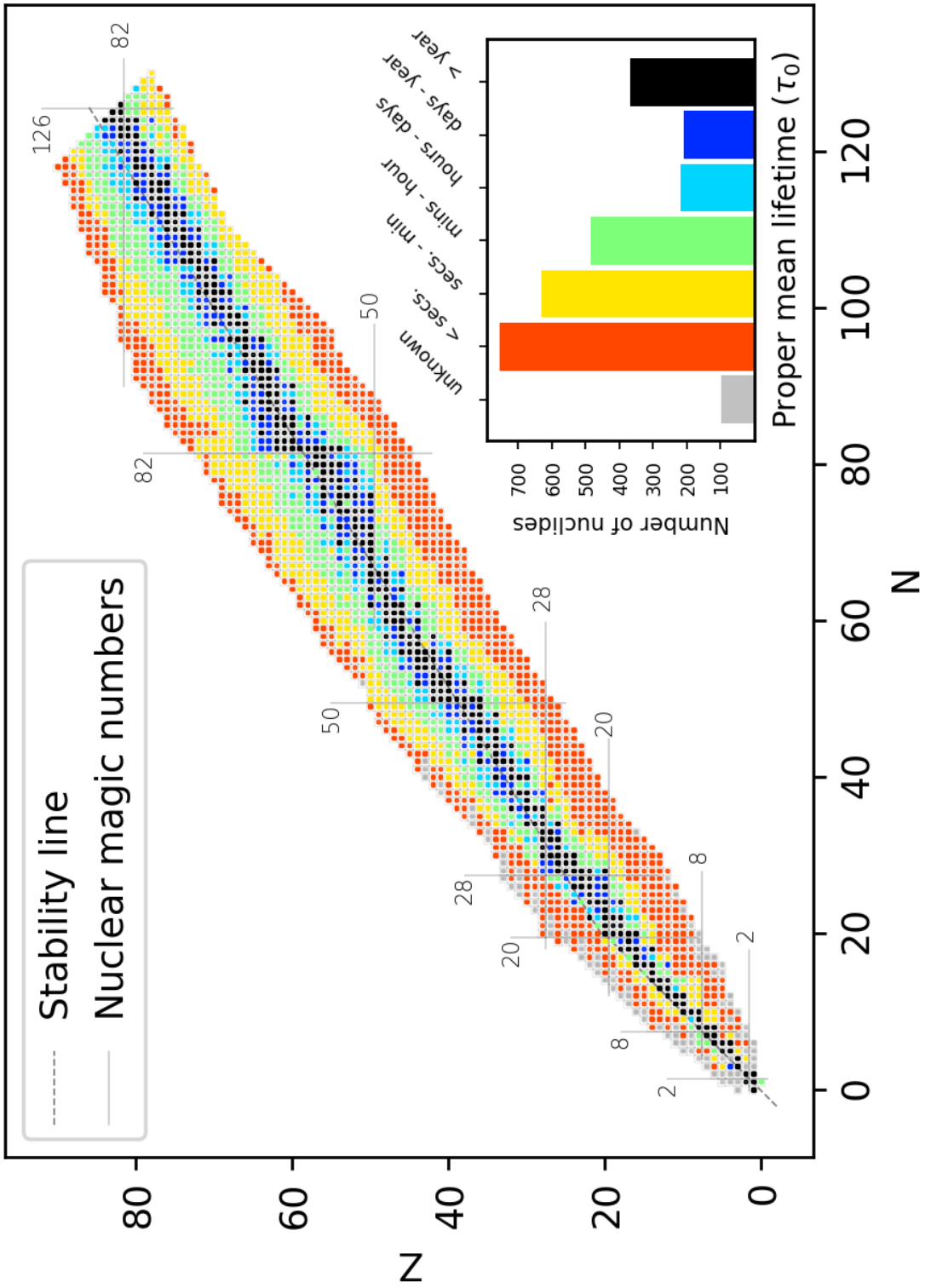

Figure 3.3: Mean lifetime for nuclides with known decays. These constitute tha values implemented in the models presented in this thesis. Data collected from the Atomic Mass Evaluation (AME2016) files (Huang et al., 2017, Wang et al., 2017) and from the ENSDF files (ENSDF, 2019).

$$ {}^{A}_{N}Z \rightarrow {}^{A}_{N}(Z+1) + e^- + \bar{\nu}_e \quad (\beta^-\text{-decay}) \tag{3.1} $$
$$ {}^{A}_{N}Z \rightarrow {}^{A}_{N}(Z-1) + e^+ + \nu_e \quad (\beta^+\text{-decay}) \tag{3.2} $$

The theoretical energy distribution of the products (as obtained by Fermi) is shown in Eqs. 3.3 and 3.4, where $m_k, p_k, E_k, \frac{dN}{dE_k}$ are respectively the mass, momentum, energy and energy distribution of particle k (either the (anti)electron or the (anti)neutrino), and Q_β is the total energy released in the decay. The distribution is represented in Figure 3.4 in the nucleus rest frame (left), and boosted into the lab reference frame. The real form of this distribution can deviate slightly from the theoretical one depending on the properties of the nuclear state of both the initial and final nuclei (*e.g.* energy, parity, angular momentum). However, the extreme relativistic boosts considered in UHECR astrophysics, as well as the angle averaging, reduce the importance of such deviations. The recoil kinetic energy of the nucleus can also be ignored and the decay can be considered isotropic in the center-of-mass rest frame.

$$ \frac{dN}{dE_e} \propto p_e E_e (Q_\beta - E_e - m_e c^2)^2 \tag{3.3} $$
$$ \frac{dN}{dE_{\bar{\nu}_e}}(E_{\bar{\nu}_e}) = \frac{dN}{dE_e}(Q_\beta - E_e) \tag{3.4} $$

Particle decay (p, n, α-decay) This is the emission of an alpha particle (nucleus of helium-4), a proton or a neutron, which may be accompanied by photon emission (Eq. 3.5). There is a loss of mass corresponding to the number of nucleons in the particle emitted (1 for p and n, 4 for α). Unlike the beta decay, it is a two-body process where the products have similar mass, and the kinetic energy released is much lower ($Q \lesssim 30$ MeV, or less than 1% of the total mass). Therefore the energy distribution can be described as a delta function, the kinetic energy released can be neglected in the decay of UHECRs, and the assumption of boost conservation applies.

$$ {}^{A}_{N}Z \rightarrow {}^{A-1}_{N}(Z-1) + \mathrm{p} \quad (\mathrm{p}\text{- decay}) \tag{3.5} $$
$$ {}^{A}_{N}Z \rightarrow {}^{A-1}_{N-1}Z + \mathrm{n} \quad (\mathrm{n}\text{- decay}) \tag{3.6} $$
$$ {}^{A}_{N}Z \rightarrow {}^{A-4}_{N-2}(Z-2) + \alpha \quad (\alpha\text{- decay}) \tag{3.7} $$

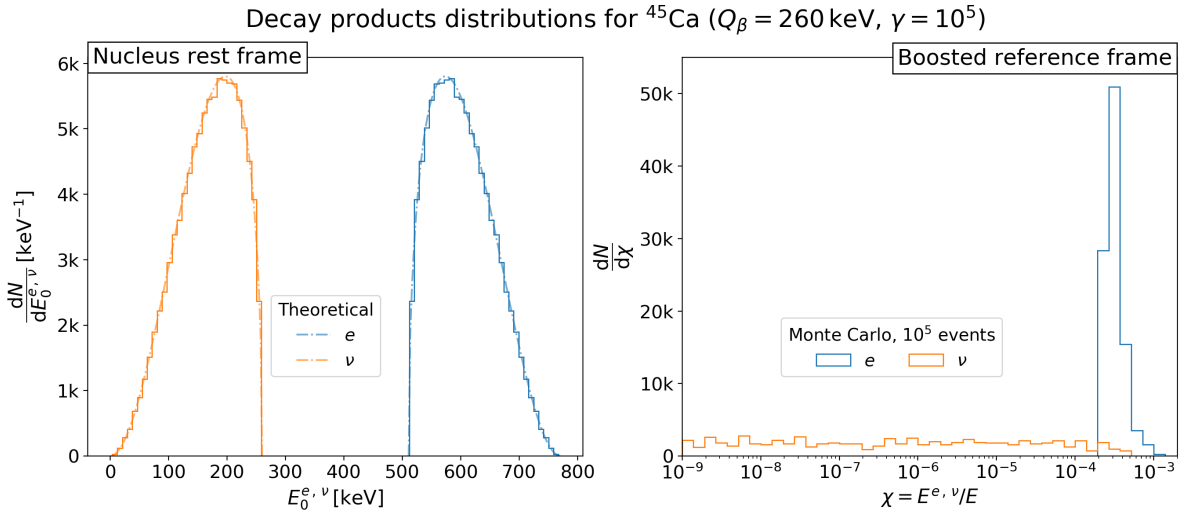

Figure 3.4: Left: spectral energy distributions in the nucleus rest frame of an electron and an antineutrino emitted from a relativistic nucleus with $A = 40$: Monte Carlo result (solid) and theoretical (dashed). Right: same simulation result boosted into the lab frame.

Internal transition or photon emission All the above decays may produce nuclei in excited states. The subsequent decay of such states occurs with the emission of photons with energies between hundreds of keV and a few MeV (Eq. 3.8) with a defined energy and a narrow energy spread. The emission may have anisotropies due to the parity and momentum differences between the initial and final nuclear states; nevertheless, they can be considered isotropic for the purpose of cosmic-ray astrophysics where the production is angle-averaged and the spectrum is dominated by relativistic boost effects from the ultra-relativistic speeds of the emitting nuclei. The photon energy in the nucleus rest frame typically does not exceed a few MeV; however, due to the ultrarelativistic speeds of cosmic ray nuclei, these photons will emerge as X-rays or gamma rays in the rest frame of the astrophysical medium. For instance, an MeV photon emitted in the decay of an UHECR nucleus with $\gamma = 10^9$ is seen as a PeV gamma ray in the SRF. In theory, these gamma rays could potentially provide observational evidence of cosmic ray interactions in the source, which is the topic investigated in Chapter 5.

$$ {}^{A}_{N}Z^{*} \rightarrow {}^{A}_{N}Z + \gamma \tag{3.8} $$

Photodisintegration and photomeson production

The interactions of photons with nuclei can conduce to multiple phenomena depending on the center-of-mass energy, the relative angular momentum and the internal energy levels of the

nucleus involved. The astrophysics scenarios considered here involve nuclei interacting with photons of a broad energy spectrum. The kinematics is not simulated in detail, instead, only a few parameters are included like the center-of-mass energy, the multiplicity of the products and their energy distribution. In the case where either the cosmic rays or the photons are distributed anisotropically, additional information is necessary regarding the angular distribution of the interacting particles. However, this thesis will focus specifically on cases where both cosmic rays and photons can be described as isotropic and homogeneous distributions.

The description of photonuclear interactions that follows is based on the general assumption that the processes can be described through the dependence of the cross section on the energy of the incoming photon in the nucleus rest frame, ϵ_r. The intermediate states undergone by the nucleus are not modeled in detail, and we assume it is sufficient to know the average number of products and their energy distributions. The energy ϵ_r is obtained through the following transformation from the SRF into the rest frame of the cosmic ray:

$$\epsilon_r = \gamma\varepsilon'(1 - \cos\theta), \tag{3.9}$$

where γ is the Lorentz factor of the cosmic-ray nucleus, and ε' is the photon energy in the SRF, and θ is the pitch angle, defined as the angle between the momenta of the photon and the cosmic ray. This transformation is represented in Figure 3.5. The left panel shows the example of a thermal field in the SRF, with the color representing the frequency of the photons, assumed to be isotropic in the SRF (as shown in the middle panel). The photons that have a trajectory close to head-on relative to the the cosmic ray, will appear boosted in the cosmic-ray rest frame, due to Eq. 3.9; while the photons that deviate more from a head-on trajectory will appear with their frequency more and more de-boosted in the cosmic ray rest frame (right-hand-side panel).

Photons excite internal nuclear levels below the average energy per nucleon (8 MeV) corresponding to individual excitation of nucleons analogous to how individual electrons account for excitations in an atom (Greiner and Maruhn, 1996). These levels range in energy from a few keV to a few tens of MeV. However, as the photon energies approach the mean energy per nucleon, collective excitations of the nucleus take place predominantly. The most prominent of these is known as the Giant Dipole Resonance (GDR) and it manifests as a notable increase of the cross section with a wide energy range of excitation. The total photo-nuclear cross section for different nuclei is shown in Figure 3.6, where the GDR appears in the energy range of $\epsilon_r = 8 - 40$ MeV. It is shaped usually as one broad peak but in many cases it can exhibit two peaks caused by the radial asymmetries found in some nuclei.

Given the sufficiently high photon energies ϵ_r, the emission of particles is energetically possible and the nucleus will disintegrate. The most common products are neutrons, but protons and

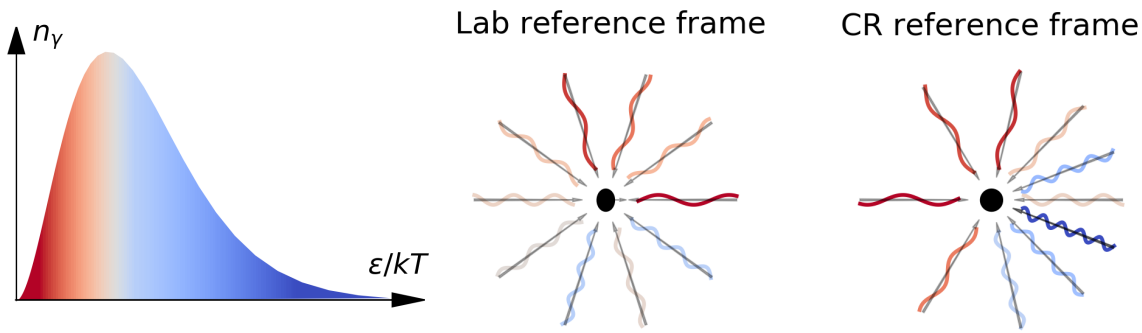

Figure 3.5: Schematic representation of the relativistic boost of photons into the rest frame of a cosmic ray. A thermal spectrum of photons (left) is color-coded with a red-to-blue scale corresponding to low-to-high energy centered in the mean value. In the laboratory frame, or more precisely the rest frame of the astrophysical source (middle) a cosmic-ray particle (black) is moving through an isotropic field of photons (curved lines, wavelengths inversely proportional to their energies). In the rest frame of the cosmic ray (right), both the angular and the energy distributions are affected by the special-relativistic effects. The transformation of the photon energy is given by Eq. 3.9.

alpha particles can also be emitted. General trends have been found, such as the decrease of the peak energy and the broadening of the GDR with the mass number. These trends can be used to model the cross section analytically. For example, an Atlas of GDR parameters has been published (Plujko et al., 2011) where the values were obtained by fitting a large number of experimental cross sections for many nuclei to a unique analytical function. The compilation by Otuka et al. (2014) of several cross section measurements for photodisintegration is currently one of the most complete databases. However, as noted by (Boncioli et al., 2017) the data is still sparse and mainly available for stable nuclei. Additionally, there are very few measurements for isobars (nuclei with the same nuclear mass) where variance is expected, since their mass and nuclear levels are known to differ. This is an important uncertainty that may affect modeling in astroparticle physics. Hence, parametrizations and codes based on the limited data may be biased by incorrectly extrapolating based on stable nuclei phenomenology.

The cross section decreases considerably beyond the GDR and is almost constant in the range $\epsilon_r = 50 - 140$ MeV, where quasi-deuteron scattering is the dominant process (Odian et al., 1956, Fuji, 1962)). The interacting photon is predominantly absorbed by a pair of nucleons which escape absorbing most of the energy, the rest remaining in the nucleus. The production cross sections cannot be calculated analytically so it needs to be measured when possible. There are codes that use nuclear models and other experimental data to estimate these production rates

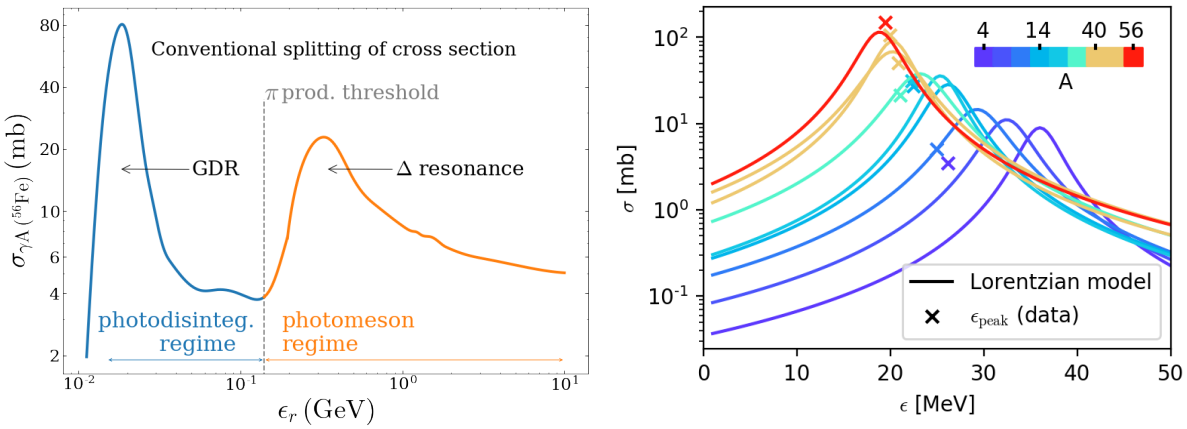

Figure 3.6: Left: Photonuclear inelastic cross section for ^{56}Fe showing the main features common to all nuclei. In the disintegration regime at lower energies the interaction is dominated by the Giant Dipole Resonance (GDR). In the photomeson regime, at higher energies, the Delta Resonance (DR) dominates the interaction cross section (see Section 3.1.1 for further discussion). Right: The lorentzian model for the GDR (curves) compared to experimentally determined peaks (see Section 5.2.

for nuclei where experimental data is unavailable, such as FLUKA (Ferrari et al., 2005) and Talys (Koning et al., 2007, 2005).

The photodisintegration process can be simulated using empirical models, like the Puget-Stecker-Bredekamp (PSB) model (Puget et al., 1976), or tabulated data based on dedicated codes that simulated these interactions in detail, such as Talys (Koning et al., 2007) and Peanut (Fassò et al., 1997, 2005), which is part of Fluka . Talys can only be applied to nuclei with mass number $A \geq 12$, so complete tables tables must additionally include a compilation of cross sections for lighter elements, as can be found in Kampert et al. (2013).

Boncioli et al. (2017) detailed a comparison of these models to data, as well as their impact on specific astrophysical source simulations. The different models exhibit qualitative and quantitative differences in the disintegration chain. In the PSB model only one stable nucleus is considered per mass, and therefore a unique disintegration possibility is available per interaction, namely the emission of one nucleon. Talys and Peanut, which simulate the dynamics of the interactions, show helium emission in addition to nucleons. These two models are qualitatively similar but in most cases exhibit differences on the cross sections and the rates of products. Boncioli et al. (2017) have argued for the need for systematic measurements of the production and total cross sections for many nuclei due to the disagreements between codes. It was also found that in general Peanut is better tuned to experimental data, which may be because Talys assumes a unique total absorption cross section for different nuclei in a given isobar. For some

nuclides where Talys shows significant deviation from data, corrections have been introduced for applications to astroparticle physics (Alves Batista et al., 2015). The photodisintegration model used in this thesis is Talys , except when a different one is explicitly specified.

While the regime below 140 MeV is known is astroparticle physics as the *photodisintegration regime*, above these energies we enter the *photomeson regime*. Here, the photon energy ϵ_r exceeds the pion production threshold, and the photon interacts with individual nucleons, as evidenced by the appearance of nucleon resonances in the cross section. The peak known as the Δ resonance appears at the same energy of the first nucleon excited state $\Delta(1232)$, in the energy range $140 - 350$ MeV in Figure 3.6. As with photon interactions with free nucleons at these energies, pions are produced, leading to subsequent neutrino and photon emission from pion decays (Eq. 3.10).

$$
\begin{aligned}
p + \gamma \;\rightarrow\; & \begin{cases} \Delta \rightarrow p\,\pi^0 \;/\; n\,\pi^+ & (\Delta \text{ resonance}) \\ \sum \pi^{\pm,0} & (\text{Multi-pion production}) \end{cases} \\
\pi^+ \;\rightarrow\; & \mu^+ + \nu_\mu \rightarrow (e^+ \nu_e \bar{\nu}_\mu) + \nu_\mu \,, \\
\pi^- \;\rightarrow\; & \mu^- + \bar{\nu}_\mu \rightarrow (e^- \bar{\nu}_e \nu_\mu) + \bar{\nu}_\mu \,, \\
\pi^0 \;\rightarrow\; & \gamma\gamma
\end{aligned}
\tag{3.10}
$$

For nucleons, pion production at threshold leads to an energy distribution between the proton and the pion that follows the mass ratio, which means the pion takes $\sim 20\%$ of the nucleon energy. At higher energies, multi-pion production dominates the total cross section.

The pions are unstable and decay predominantly as $\pi^+ \rightarrow \mu^+\nu_\mu \rightarrow e^+ + \nu_e + \nu_\mu$ (weak interaction) and $\pi^0 \rightarrow \gamma\gamma$ (electromagnetic interaction). The neutron produced in the charged pion channel will decay weakly into a proton, $n \rightarrow p + e^- + \bar{\nu}_e$.

The charged pion channel is widely expected to be the main source of high-energy astrophysical neutrinos. Since this channel has a branching ratio of 2/3 compared to 1/3 for the neutral pion channel, the average number of positive, neutral and negative pions emitted is equal. Given the decay reactions shown above, the expected flavor ratio of neutrinos from photo-pion production is therefore $\nu_e : \nu_\mu = 1 : 2$, while tau neutrinos are not produced directly from this process (although this flavor can be created through neutrino oscillations in the course of the propagation of the neutrinos over cosmological distances). This scenario can change, however, if the secondary muons lose sufficient energy before decaying (through synchrotron radiation in sources with high enough magnetic fields); in the most extreme case where muons are not allowed to decay at all, only muon neutrinos (from the direct pion decay) would be emitted by

the source.

The photomeson regime is widely modeled in the astroparticle physics community using the code Sophia (Mucke et al., 2000), which is a Monte Carlo event generator developed for interactions of free protons and neutrons with photons. This code is an implementation of earlier work by Rachen (1996), who compiled the experimental data.

For nuclei, a superposition model is typically assumed (Hummer et al., 2010, Aloisio et al., 2017, Alves Batista et al., 2016), motivated by the similarity between the cross section for free nucleons and those inside a nucleus. In these superposition models the interacting nucleon is then ejected, while the remaining nucleus is kept intact. The discussion of the limitations of this model and its improvement has been published recently (Morejon et al., 2019a) and is one of the results of this thesis (see Chapter 4).

Shortly after the detection of the Cosmic Microwave Background (CMB), interactions between CR protons with the CMB were studied. Greisen (1966) and Zatsepin and Kuzmin (1966) proposed that photo-pion production of cosmic-ray protons propagating in the intergalactic space would cause a suppression in the CR spectrum at 10^{20} eV, a phenomenon that became known as the *GZK effect*. The neutrinos produced by these interactions are referred to as GZK neutrinos, or more generally *cosmogenic neutrinos*. Additionally to the CMB, the extragalactic background light (EBL) can also serve as a target photon field for photohadronic interactions of propagating UHECRs. This background radiation originates in non-thermal emission from AGNs, as well as in star-forming activity. Subsequently to the work by Greisen, Zatsepin and Kuzmin, Stecker (1969) addressed the photodisintegration of relativistic nuclei heavier than protons through interactions with the CMB and the EBL, and found that extensive air showers could not be interpreted as purely protons.

As can be seen in Figure 3.6, the Δ resonance can be excited by a photon with approximately 300 MeV in the proton rest frame. This means that a CMB photon will interact through the Δ resonance with a cosmic-ray proton with energy $\gamma \approx 10^{11}(\epsilon_{\rm CMB}/2\ {\rm meV})^{-1}$, emitting four neutrinos (in the case of charged pion production, Eq. 3.10) each with an energy of around 5×10^9 GeV, or 5% of the proton energy, or two gamma rays, each with 10% of the proton energy (in the case of neutral pion production). The photons will eventually cascade down to lower energies through successive pair production interactions with the photon backgrounds (*cf.* next section), while the neutrinos will travel in a straight trajectory, losing energy only through the cosmological expansion.

On the other hand, for a nucleus to photodisintegrate through the GDR, the photon must have an energy of only around 20 MeV in the nucleus rest frame, an order of magnitude lower than the Δ resonance. Therefore a nucleus with Lorentz factor $\gamma \approx 10^{10}$ will photodisintegrate with the CMB through the GDR, producing lighter isotopes that will have the same Lorentz factor. For

a mass number of the order of $A \sim 10$, this corresponds to the same kinetic energy $E \approx \gamma A m_p$ as a proton that interacts through the Δ resonance. More generally, given a nucleus with a certain kinetic energy E, the higher its mass number A, the lower its Lorentz factor and therefore the higher the energy of the target photon that is necessary to meet the photodisintegration threshold.

An aspect that is not considered in the literature is the propagation of UHECR nuclei heavier than iron ($A > 56$), although it is known that such elements are present in astrophysical sources (such as r-process-driven kilonovae, Tanvir et al., 2013, Cowperthwaite et al., 2017) which can potentially be accelerated to ultra-high energies. A framework for treating interactions of these super-heavy UHECR nuclei is presented in Chapter 6.

3.1.2 Electromagnetic interactions

Synchrotron radiation

The emission of photons by a charged particle due to scattering off a magnetic field. For a nucleus with Lorentz factor $\gamma = E/(Am_p)$ interacting with a magnetic field of strength B, the (angle-averaged) energy loss rate is given by

$$\left|\frac{dE}{dt}\right|_{\text{synch}} = \frac{c\,\sigma_T}{6\pi m_e\, c^2}\, Z^4 \left(\frac{m_e}{A\, m_p}\right)^3 B^2\, \gamma^2 \tag{3.11}$$

where σ_{T} is the Thomson cross section. For the purposes of this work, we will be interested in the case of highly relativistic particles interacting with a homogeneous and isotropic magnetic field, which justifies the averaging of the pitch angle dependence that is implicit in this formula (*cf.* Blumenthal, 1970). The power loss given by Eq. 3.11 corresponds to the luminosity of the emitted synchrotron radiation.

The equivalent expression can be obtained for electrons by making $Z = 1$ and replacing $Am_p \to m_e$. Synchrotron radiation from a spectrum of accelerated electrons is a common mechanism behind the emission from non-thermal sources, such as GRBs and their afterglows (*e.g.* Wijers and Galama, 1999) and AGNs (see *e.g.* Section 5.4), as well as from Galactic sources, in some cases with observed frequencies reaching the X-ray range (*e.g.* Aharonian et al., 2005). In AGNs, electron synchrotron emission is typically responsible for the broadband emission ranging from radio up to infrared/optical/UV, or even up to X-rays in the case of so-called 'extreme blazars' like Markarian 501 (Kataoka et al., 1999). Therefore, these photons are often the main target for photonuclear interactions of cosmic-ray proton and nuclei co-accelerated in the source, although in some models that role can also be played by thermal

photons originating outside the AGN jet (*e.g.* Murase et al., 2014, Rodrigues et al., 2018).

In proton synchrotron models of AGNs (Mucke and Protheroe, 2001), the high-energy broadband emission (X-rays to gamma rays) is explained by synchrotron radiation from accelerated protons. However, because of the scaling of Eq. 3.11 with the nucleus mass, synchrotron emission is highly suppressed for cosmic rays compared to electrons, by a factor $Z^4(\frac{m_e}{A\,m_p})^3$, which is around 10^{-10} for protons. Furthermore, for a given value of γ, the frequency of the emitted photons follows a distribution dominated by a 'characteristic' photon frequency that scales inversely with the mass of the particle. These two factors imply that proton synchrotron models usually require either very high deposited power in non-thermal protons and high maximum proton energies, and/or a very high magnetic field strength in the source.

Inverse Compton scattering

The inelastic scattering of photons by a highly relativistic charged particle through the electromagnetic interaction. In the so-called Thomson regime (when the energy of the photon in the particle rest frame is small compared to the particle's rest mass), the energy loss is given by (Blumenthal, 1970)

$$\left|\frac{\mathrm{d}E}{\mathrm{d}t}\right|_{\mathrm{IC}} = \frac{4}{3} n_\gamma \sigma_{\mathrm{T}} c\, Z^4 \left(\frac{m_e}{A m_p}\right)^2 \gamma^2, \tag{3.12}$$

where like in Eq. 3.11, the equivalent expression for electrons is obtained by replacing $Am_p \to m_e$, $Z = 1$. This energy is transferred to the photon, which receives a frequency boost as a result of the interaction. As we can see from the expression, this frequency boost is proportional to γ^2.[2]

In leptonic phenomenological models of astrophysical sources, gamma-ray emission is often explained through inverse Compton scattering of photons by accelerated electrons. An example of such model will be discussed in Chapter 5 with the example of the AGN jet of the galaxy Centaurus A. In that system, the target photons for the scattering are synchrotron photons emitted by the same electron population, in which case we talk about a synchrotron self-Compton (SSC) scenario.

Finally, note that like in the case of synchrotron emission, this process is highly suppressed for nuclei compared to electrons due to the mass dependence of the rate.

[2] For electrons, it is often the case that the energy of the photon in the electron rest frame is comparable to the $\varepsilon_r \gtrsim m_e$, (Klein-Nishina regime), in which case the recoil energy of the electron becomes important kinematically, and the frequency boost given to the photon becomes less efficient, scaling with γ instead of γ^2. In the case of a nucleus, this regime is is rarely relevant astrophysical scenarios, since the photon energy in the rest frame of the nucleus would have to surpass the GeV scale.

Photo-pair production

This corresponds to the creation of an electron-positron pair by the interaction of a cosmic ray with low-energy photons, and is also known as Bethe-Heitler pair production (Bethe and Heitler, 1934):

$$N + \gamma \rightarrow N + e^+ + e^-. \tag{3.13}$$

This process has a threshold of $\varepsilon_r = 2m_e c^2 \approx 1$ MeV, which for CMB photons corresponds to an UHECR nucleus with Lorentz factor $\gamma \sim 10^9$. This can in principle cause the ankle in the observed UHECR spectrum, assuming the flux is dominated by protons (Berezinsky and Grigor'eva, 1988, Berezinsky et al., 2006b, Aloisio et al., 2007). However, several arguments have since disfavored this so called *dip model* such as the heavier composition observed by Auger (Bellido, 2017a) and the very high cosmogenic neutrino and gamma ray fluxes expected in this case (Heinze et al., 2016, Supanitsky, 2016).

Although pair production has a higher cross section compared to other cosmic ray photo-interactions. However, the energy loss per interaction is low (around 1% per interaction), making the energy loss rate comparatively small to other processes. This is also the reason why pair production losses are typically treated assuming a continuous energy loss approximation. This loss term was derived analytically by Blumenthal (1970) in terms of an integral involving the target photon density spectrum $n_\gamma(\varepsilon_r)$:

$$\left|\frac{dE}{dt}\right|_{e^+e^-} = \alpha_0 r_0^2 Z^2 m_e^2 \int_2^\infty d\varepsilon_r \, n_\gamma(\varepsilon_r) \left(\frac{\varepsilon_r m_e}{2\gamma}\right) \frac{\Phi(\varepsilon_r)}{\varepsilon_r^2}, \tag{3.14}$$

where α_0 is the fine-structure constant and r_0 is the classical electron radius. The dimensionless function $\Phi(\varepsilon_r)$ contains the angle-averaged cross section and inelasticity. For nuclei this scales as $Z^2 A^{-1}$, since the cross section increases with Z^2 while the inelasticity scales as A^-1. However, the threshold also increases proportionally to A (appearing in the above formula implicitly in the Lorentz factor Γ). Effectively this threshold scaling makes pair production off nuclei subdominant compared to photodisintegration (see *e.g.* Biehl et al., 2018b, Rodrigues et al., 2018, where this is shown for GRBs and AGNs, respectively). However, as we will show in Chapter 5 in the case of the Centaurus A AGN, this process can still be relevant in astrophysical contexts.

Photon-photon annihilation

To conclude this section, it is worth mentioning that in the presence of magnetic fields, two photons can interact to produce an electron-positron pair. This process has the same threshold energy as Bethe-Heitler pair production ($\sqrt{E_{\gamma 1} E_{\gamma 2}} = 2m_e \approx 1$ MeV), and it can lead to the attenuation of astrophysical high-energy gamma rays through interactions with softer target photons. Although this process does not directly involve cosmic rays, it plays an important role both in high-energy astrophysical sources as well as during the propagation of extragalactic gamma rays, through interactions with the radiation backgrounds. At threshold, an infrared EBL photon will annihilate and pair-produce with a gamma ray of energy $\varepsilon = 10$ TeV$(\varepsilon_{\rm EBL}/0.1$ eV$)^{-1}$, leading to the attenuation of the gamma-ray spectrum and the creation of an electromagnetic cascade, redistributing the energy to lower frequencies.

3.2 Numerical implementation

This section starts by introducing some of the fundamental equations used in describing the interactions and propagation of UHECR spectra. Following, an overview of some numerical codes for simulating these interactions in astrophysics is presented, which are the codes used later in this thesis to test the new nuclear models.

3.2.1 Basic mathematical description of radiative processes in astrophysics

Establishing the connections between all messengers in multimessenger astrophysics requires in general integrating a system of first-order partial differential equations (PDEs). Each equation in the system corresponds to a particle species and relates the energy distribution of the particle density to the interaction terms which cause it to change in time. This includes terms for the *cooling* (*i.e.* energy losses) suffered through interactions (see previous section) as well as other processes that can *remove* particles from the system, such as decays and the physical escape from a source, *add* new particles into the system, such as the injection of freshly accelerated particles from an adjacent acceleration region, and *transform* particles into other particles of different species, such as through photodisintegration, which effectively removes a nucleus from the system and replaces it with a set of lighter isotopes and nucleons. A general form of these equations is:

$$\frac{\partial}{\partial t} N_i(E,t) = \frac{\partial}{\partial E}\left(b(E) N_i(E,t)\right) + Q_i^{\rm ext}(E,t) - \Gamma_i N_i(E) + \sum_j Q_{j\to i}(N_j(E,t)), \tag{3.15}$$

where N_i is the number density of particle species i per unit of energy and volume.

The term $\frac{\partial}{\partial E}\left(b(E)N_i(E,t)\right)$ describes the processes that lead to the energy redistribution of the spectrum $N_i(E,t)$ and can in the most general case contain acceleration (energy gain) and cooling (energy loss) terms. In the numerical frameworks that will be used in this work, the acceleration process will not be simulated explicitly, and thus only loss terms are included in $b(E)$. The cooling terms account for energy losses such as synchrotron, pair production, *etc.* , which were introduced in the previous section. Assuming the the magnetic field and the target photon field n_γ are stationary, this loss term is constant in time. The second term, $Q_i^{\rm ext}(E,t)$, represents the injection rate of particles of species i from external sources, for example an acceleration region. The remaining two terms are concerned with the removal and re-injection of particles due to interactions with target photons. The improvements proposed in this thesis will affect the latter terms and in the following the expression to compute them from the cross sections are discussed.

The term $\Gamma_i N_i(E)$ denotes the reduction of particles from the system due to inelastic interactions. Γ_i is the total inelastic interaction rate of particle i and it is related to the total inelastic cross section $\sigma_i(\varepsilon_r)$ by

$$\Gamma_i(E_i) = \int \mathrm{d}\varepsilon' \int_{-1}^{+1} \mathrm{d}(\cos\theta)\frac{1-\cos\theta}{2} n_\gamma(\varepsilon', \cos\theta)\,\sigma_i(\epsilon_r), \tag{3.16}$$

where ϵ_r is given by Eq. 3.9 and $n_\gamma(\varepsilon', \cos\theta)$ gives the target photon density spectrum as a function of the photon energy ε' and the pitch angle θ. These quantities refer to the source rest frame (SRF), where the cosmic ray has been accelerated to a relativistic energy. The cross section is a function of the photon energy in the cosmic ray's rest frame ϵ_r.

In the case where unstable nuclides are explicitly included in the simulation (see discussion on nuclear decays in Section 3.1.1), an additional sink term needs to be included to account for this process. The corresponding rate for $\Gamma_i^{\rm decay} = m_i/(E_i\tau_0^i)$ where the proper mean lifetime τ_0^i refers to the nucleus rest frame and the boost into the SRF is accounted for by the Lorentz factor $\gamma_i = E_i/m_i$. Another process that can contribute to this type of term is the escape of the particles from the source, corresponding to to an additional sink term with rate $\Gamma^{\rm esc}$. The form of $\Gamma^{\rm esc}$ depends on the mechanism by which particles are assumed to escape the source (*cf. e.g.* Rodrigues et al., 2018, who discuss the effect of different escape assumptions on the cosmic ray and neutrino emission from AGN jets using the NeuCosmA code, see Section 4.1).

The lat term in Eq. 3.15, $Q_{j\to i}(N_j(E,t))$, reflects the injection of particles that are produced in certain interaction processes, where the index j indicates the particle species that participated in the interaction. This includes for example the injection of neutrons and pions from π^+

photoproduction off protons, or the injection of secondary nuclei after photodisintegration of the mother nucleus. This term depends on the production rate of the given interaction:

$$Q_{j\to i}(N_j(E_i)) = \int_{E_i}^{\infty} dE_j \frac{d\Gamma_{j\to i}}{dE_i}(E_j, E_i)\,, \tag{3.17}$$

where the production interaction rate $d\Gamma_{j\to i}/dE_i(E_j, E_i)$ is differentiated over the energy of the produced particle. This differentiation is necessary especially where the production of particles has a broad spectrum in energy or when the production cross section has a broad dependence on the emission angle. Expressing the production cross section as a differential function of the outgoing particle $d\sigma_{i\to j}/dE_i(E_i, E_j)$ the production interaction is (similar to Eq. 3.16):

$$\frac{d\Gamma_{j\to i}}{dE_i}(E_j, E_i) = \int \mathrm{d}\varepsilon \int_{-1}^{+1} \mathrm{d}(\cos\theta) \frac{1-\cos\theta}{2} n_\gamma(\varepsilon, \cos\theta)\, \frac{\mathrm{d}\sigma_{j\to i}}{\mathrm{d}E_i}(E_j, E_i, \varepsilon_r)\,. \tag{3.18}$$

There are two distinct cases for the energy distribution of outgoing particles in this framework. The **boost conservation** case applies to products whose energy distribution in the SRF is narrow and can be described by a delta function. This is the case when the energy involved in the interaction is small compared to the mass of the products in the cosmic ray rest frame. Namely, the mass of nuclear fragments emitted through photodisintegration, $\sim A$ GeV, is large compared to the photon energy in the nucleus rest frame, which reaches at most a few GeV. In such case the energy fraction taken by the products approximates the ratio of their masses, and the distribution can be described by a delta function:

$$d\sigma^{\mathrm{bc}}_{j\to i}/dE_i(E_i, E_j, \varepsilon_r) = \sigma_{j\to i}(\varepsilon_r)\delta\left(E_i - \frac{m_i}{m_j}E_j\right). \tag{3.19}$$

The **broad distribution** case applies to products whose distribution in energy cannot be reduced to a narrow function. This is the case for particles whose mass is much lower or comparable to the energy involved (photons, neutrinos, electrons, pions, etc. and also protons). For these particles the energy boost is strongly affected by the emission angle, resulting in a broad distribution in the SRF.

$$d\sigma^{\mathrm{bd}}_{j\to i}/dE_i(E_i, E_j, \varepsilon_r) = \sigma_{j\to i}(\varepsilon_r)\chi(E_i/E_j), \tag{3.20}$$

where χ is the energy distribution function of the products in the SRF. For Lorentz factors sufficiently high (UHECR energy $E_i > 10^6$ GeV), this distribution only depends on the energy ratio between the original cosmic ray i and the product j.

Codes and implementation of photonuclear interactions

The equations and relations presented in the previous section represent the most general form. Different numerical codes exist that solve these equations employing different implementations in congruence with the physical scenario studied. The numerical codes employed in this work are introduced in the respective chapters discussing their use and results. The implementations in general involve producing interaction tables, which are often precomputed to speed up the computations. The precomputed quantities involve the angle averaged cross sections, which can be used to compute the interaction rates once the target photon spectrum is known (given the astrophysical scenario). In the case of extragalactic UHECR propagation, the target photons are the cosmological radiation backgrounds which depend on the redshift only in the norm of the spectrum (in the case of the EBL, a model must be assumed, *e.g.* Dominguez et al., 2011, Gilmore et al., 2012). Hence the precomputed interaction tables can include the photon spectra and the scaling with redshift may be applied during simulation time. The interaction models developed in this thesis have been made available to these codes, including software tools that allow future implementations additional codes and related numerical computations.

Chapter 4

A new improved model of nuclear photomeson interactions

The detection astrophysical neutrinos at very high energies indicates that photomeson interactions occur in the sources of UHECRs. These neutrinos result in decays of mesons which are produced by UHECRs interactions with surrounding photon fields. While this process is well understood for UHECR protons, this is not the case for nuclei.

This chapter introduces an improved model for the photomeson production off nuclei and compares it to the widespread "Single Particle Model". The improvements involve modifications relevant for the astrophysical processes: improved cross section descriptions driven by data, and empirical approaches to describe the fragmentation of the nucleus. The impact of these modifications is illustrated in astrophysical simulations of Gamma-Ray Bursts (GRBs) and Tidal Disruption Events (TDEs). The paper is organized as follows: Section 4.1 discusses the physical differences between photon interactions with nucleons and with nuclei, and the quantities and nomenclature related to multimessenger astroparticle physics. Section 4.2 presents the ingredients of the new photomeson model,referred to by Empirical Model (EM). The EM is contrasted with a different alternative previously proposed, and not implemented before in the literature, referred to as Residual Decay Model (RDM). The EM is found in better agreement with the experimental data available. Section 4.3 illustrates the impact of the model in astrophysical source simulations in which the photomeson model is relevant.

The content of this chapter has been published by Morejon et al. (2019a). The models and the tools to reproduce the results have been made available to the community by Morejon (2019b).

4.1 Astrophysical photohadronic interactions: $p\gamma$ vs $A\gamma$

The photomeson interactions of nuclei resemble at first glance interactions of individual nucleons non-interacting nucleons. Therefore it is instructive to first discuss the photomeson production in the absence of collective effects, *i.e.* in interactions of photons with free nucleons, which have been extensively studied experimentally and theoretically (Ho ohler et al., 1965, Feynman,

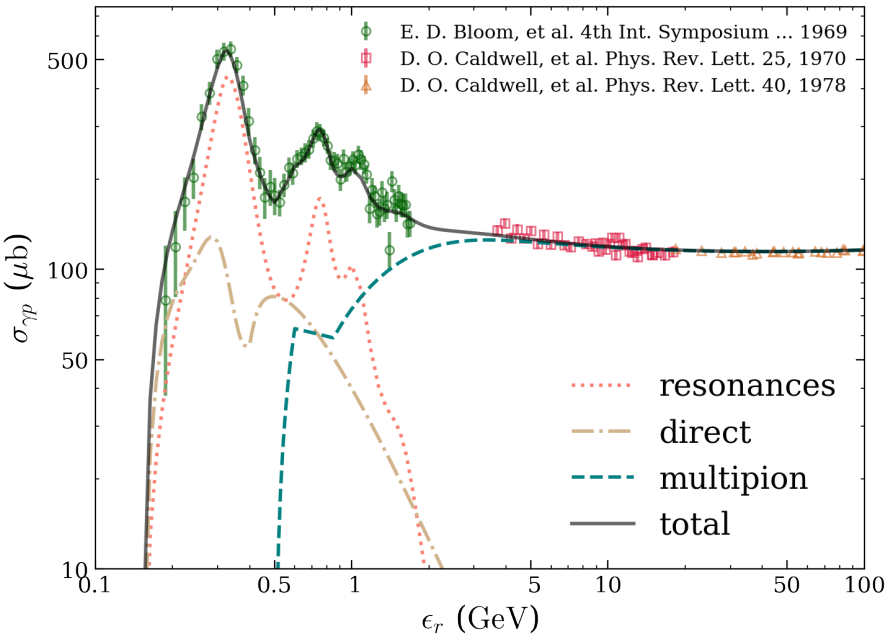

Figure 4.1: The cross section for inelastic scattering of photons by protons as a function of photon energy in the proton rest frame ϵ_r. The curves correspond to the theoretical estimates of different processes. The measurements of the total cross section are by Bloom (1969), Caldwell et al. (1970, 1979). Figure taken from Morejon et al. (2019a).

1972). The proton and neutron cross sections are different below $\sim 140\,\mathrm{MeV}$, since for protons Thomson scattering and pair-production are possible, whereas only the much weaker magnetic moment scattering occurs for the neutron (Gould, 1993). However they are very similar above the photopion production threshold energy 140 MeV. The production of pions at threshold occurs through the excitation of the lightest baryonic resonance (Δ) in resonant (s-channel) scattering. This process has no counterpart in pp scattering since there are no known di-baryon resonant states, and hence no s-channel equivalent. Instead, mesons are produced through t-channel processes at sufficiently large momentum transfer. Above the pion threshold more channels are available for the production of higher mass resonances and there are small differences between proton and neutron cross sections (see Figure 4.1). At high energies above a few GeV, the photon interacts mostly as a virtual vector meson (see for instance (Engel, 1995)) and all phenomena of hadronic interactions can occur.

In the nuclear rest frame the photon energy ϵ_r and the cross section are similar to the case of a nucleon with the same Lorentz boost. Given the energy of the relativistic nucleus E and the photon energy ε in the observer's or (cosmological) comoving frame, $\epsilon_r = E\,\varepsilon\,(1-\cos\theta)/m_j$,

where the pitch angle θ is the angle between incident photon and nucleus such that $\cos\theta = -1$ represents head-on collisions. ϵ_r is related to the center-of-mass energy by $s = m_j^2 + 2m_j\epsilon_r$ where m_j is the mass of the nucleus. The photonuclear interaction rate and the interaction cross section σ are related as Eq. 3.16 and is expressed in units of inverse length. Depending on the type of source or environment, the photon spectrum can extend from sub-eV up to TeV energies, and its shape can contain peaked (thermal) or power-law (non-thermal) components.

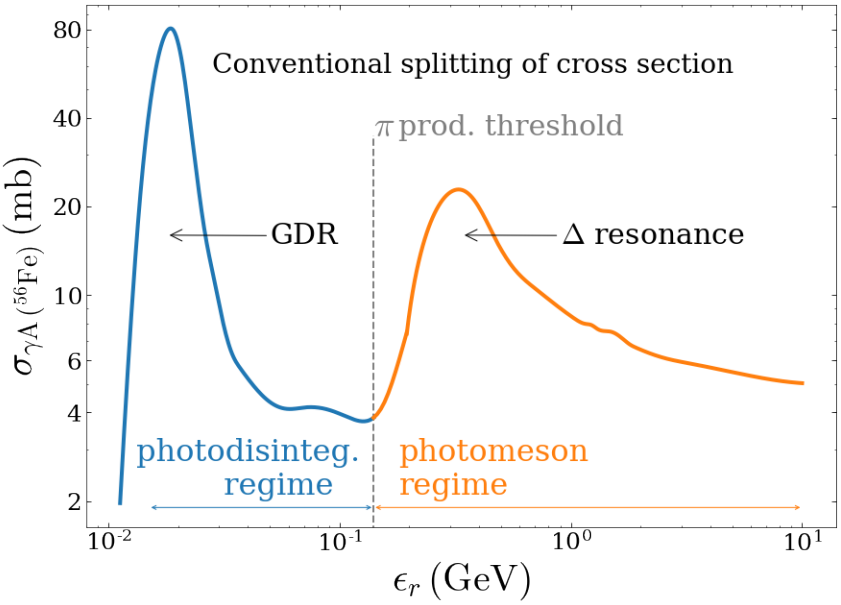

Figure 4.2: The total inelastic photonuclear cross section for ^{56}Fe as a function of photon energy in the nucleus' rest frame illustrates the general shape for nuclei. The convention of distinguishing two regions based on the photon energy is represented with a change of the color. The photodisintegration portion (in blue) refers to photon energies ϵ_r below the photopion production threshold ($\sim 14\,\mathrm{MeV}$), and the photomeson portion (in orange) refers to photon energies above the photopion production threshold. Figure taken from Morejon et al. (2019a).

The shape of a typical photonuclear cross section is illustrated in Figure 4.2 for ^{56}Fe. The energy range is split in two energy regimes. The photodisintegration regime is characterized by the absence of hadron production and negligible momentum transfer to recoils compared to typical cosmic ray energies (boost conservation). A more detailed discussion about the role of photodisintegration for cosmic ray astrophysics is contained in *e.g.* (Boncioli et al., 2017, Alves Batista et al., 2015, 2019b). The photomeson regime leads to the production of predominantly pions, but also other mesons are possible given the photon energy exceeds the production threshold. Here, the momentum transfer can be significant compared to the mass of the mesons.

The energy behavior of the cross section is similar, for example the resonance has the same position, however, the nucleon resonance are in general broader and less resolved in nuclei.

Based on these similarities, the simplest form of photomeson description for nuclei assumes the individual nucleon interactions with the photon disregarding the remainder of the nucleus. The final state particles are the products of the γN interaction and one remnant nucleus with $A-1$ nucleons. The inelastic cross section is thus computed scaling with the nuclear mass A, *i.e.* $\sigma_{A\gamma} = A\sigma_{p\gamma}$, implying that $\mathrm{d}\sigma^{\mathrm{incl}}_{j\to i}/\mathrm{d}E_i = A_j\,\mathrm{d}\sigma^{\mathrm{incl}}_{N\to i}/\mathrm{d}E_i$. This model has been used commonly in the cosmic ray astrophysics literature (Kampert et al., 2013, Hummer et al., 2010) and it will be referred here as *Single Particle Model* (SPM). Section 4.2 discusses the limitations of the SPM an the context of experimental observations.

Implementation of photomeson interactions in NeuCosmA

The photomeson interactions are included astrophysical simulations by means of cross sections for the interaction and production of pions. The transport equations Eq. 3.15 contain the re-injection terms that describe the production rate of secondaries of type i by species j at energies $E_i < E_j$. These processes remove density from species j corresponding to interactions and/or decay processes. The re-injection rate (Eq. 3.17) is the product of the parent particle density N_j and the interaction rate for producing species i. The interaction rate Eq. 3.18 contains the dependency on the inclusive cross section (production cross section labeled here $\sigma^{\mathrm{incl}}_{j\to i}$ for clarity). By integrating the inclusive differential cross section $d\sigma^{\mathrm{incl}}_{j\to i}/\mathrm{d}E_i\,(E_j, E_i)$ we define the multiplicity as

$$M_{j\to i}(E_j) = \frac{1}{\sigma_j(E_j)} \int \mathrm{d}E_i \frac{d\sigma^{\mathrm{incl}}_{j\to i}}{\mathrm{d}E_i}(E_j, E_i)\,, \tag{4.1}$$

which has the meaning of the average number of particles of species i produced per interaction. In the boost conservation scenario, the inclusive cross section takes the simple form

$$\frac{\mathrm{d}\sigma^{\mathrm{incl}}_{j\to i}}{\mathrm{d}E_i}(E_j, E_i) \approx \sigma_j(E_j) M_{j\to i}(E_j)\,\delta\left(E_i - \frac{A_i}{A_j}E_j\right). \tag{4.2}$$

For species i other than the remnant nucleus (such as $\pi^{\pm}$, π^0, secondary p, n and higher mass hadrons), the redistribution function does not have a simple parametrization and needs to be obtained from simulations with Monte Carlo codes like Sophia .

The code employed here is NeuCosmA (Hummer et al., 2010, Baerwald et al., 2013) which is a software to calculate the photohadronic interactions of cosmic rays with photon fields in astrophysical sources. It has been successfully used previously to study different source classes expected to accelerate UHECRs, such as GRBs (Biehl et al., 2018b) and AGN jets (Rodrigues

et al., 2018). It solves the system of equations Eq. 3.15 using the time-dependent Crank-Nicolson solver (Crank and Nicolson, 1996), which calculates the particle density spectra iteratively, which means that at a given time step t_n the calculated densities depend on the state of the system in the previous time step t_{n-1}, *i.e.* $N_i^n = N_i^n(n_\gamma, N_i^{t=n-1}, N_j^{t=n-1})$, where j represents the indices of all the species that are coupled to species i through a term like that shown in Eq. 3.17.

In NeuCosmA , the photon density spectrum n_γ is not self-consistently generated by the interactions, but is instead input by the user. For instance, a density spectrum in the source can be estimated based on multi-wavelength observations of that source.

Nuclear interactions are implemented by providing tabulated response functions which are read by NeuCosmA during runtime. These response functions encode the cross sections for the interactions and include the pitch-angle averaging under the assumption of an isotropic target photon field.

The response function $f(y)$ describes the total inelastic interactions as a function of angle-averaged photon energy $y \equiv E_i\varepsilon/m_i$. It results from the angle integration in Eq. 3.16 excluding the photon density (assuming the photon field has no dependence on the pitch angle):

$$f_i(y) = \frac{1}{2y}\int_0^{2y} \mathrm{d}\varepsilon_r\, \varepsilon_r\, \sigma_i(\varepsilon_r). \tag{4.3}$$

The response functions for particle production are computed for the case with **boost conservation** and for the case of **broad distribution** differently since the cross sections will be different. In the first case it is completely analogous to Eq. 4.3 but using the production cross section in Eq. 3.20:

$$g_{j\to i}(y) = \frac{1}{2y}\int_0^{2y} \mathrm{d}\varepsilon_r\, \varepsilon_r\, \sigma_{j\to i}(\varepsilon_r). \tag{4.4}$$

In the second case, the production cross section has a differential form and so does the response function:

$$h_{j\to i}(E_i, E_j, y) = \frac{1}{2y}\int_0^{2y} \mathrm{d}\varepsilon_r\ \varepsilon_r \frac{\mathrm{d}\sigma_{j\to i}}{\mathrm{d}E_i}(E_i, E_j, \varepsilon_r). \tag{4.5}$$

With these response functions the form of the rates in Eqs. 3.16-3.18 is reduced to

$$\Gamma_i(E_i) = \int \mathrm{d}\varepsilon\, n_\gamma(\varepsilon)\, f_i(y), \tag{4.6}$$

$$\Gamma_{j\to i}(E_i) = \int \mathrm{d}\varepsilon\, n_\gamma(\varepsilon)\, g_{j\to i}(y), \tag{4.7}$$

$$\frac{d\Gamma_{j\to i}}{dE_i}(E_j, E_i) = \int \mathrm{d}\varepsilon\, n_\gamma(\varepsilon)\, h_{j\to i}(E_j, E_i, y). \tag{4.8}$$

For the extreme relativistic energies of UHECRs, distribution of products only depend on the ratio of energies $x = E_i/E_j$ (Feynman approximation). For the implementation it is therefore practical to tabulate the inclusive cross section $d\sigma_{i\to j}/dx(x, \varepsilon_r)$ as a function of x. We omit this substitution here for clarity.

Finally, given the density spectra of hadronic species at a given time step, NeuCosmA can compute the spectrum of secondaries emitted by that distribution through photo-meson production. This includes pions and kaons, the muons that are produced from their decay, and finally the spectra of muon- and electron neutrinos emitted through the decay of all these secondaries (Eq. 3.10). Electron (anti)neutrinos from $\beta^\pm$ decays are also taken into account, thus providing an estimate of the total neutrino flux emitted by the source as a consequence of all the photo-interactions.

4.2 A new model: Empirical photomeson Model (EM)

Extract parameters of the spline interpolations and report them here. We improve the SPM in three main aspects:

1. **The absorption cross section**: A "universal function" better describes the shape of the cross section per nucleon the near the Δ resonance energy. At higher energies an energy dependent mass scaling exponent is introduced to account for nuclear shadowing effects. Both modifications are motivated and derived from data.

2. **The pion production cross section**: Pion production is known to be strongly influenced by nuclear medium effects (Nagl et al., 1991, Bloch et al., 2007). The inclusive pion production cross section is derived from data (Krusche et al., 2004a) for different nuclei and parameterized with an additional curve and a mass scaling exponent that differs the absorption cross section.

3. **Nuclear fragmentation**: The photonuclear interactions can result in nuclear breakup through different mechanisms not included in the SPM. We implement two alternatives:

an Ablation-Abrasion inspired model and an empirical data-driven parametrization. The latter is found in better agreement with detailed simulations and is chosen as our baseline model.

In the following sub-sections, each of the aspects is addressed. The implementation of the model is available to the community (Morejon, 2019b) for reproduction of the following figures and implementation in other works.

Features \ Models		Single Particle Model (SPM)	Residual Decay Model (RDM)	Empirical Model (EM)
Schematics of physical process		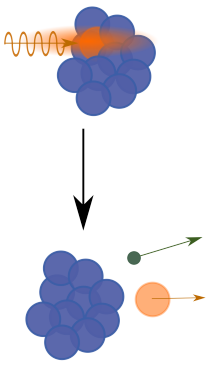	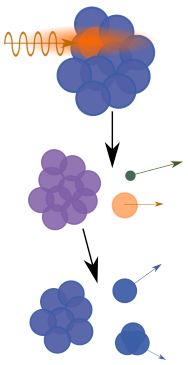	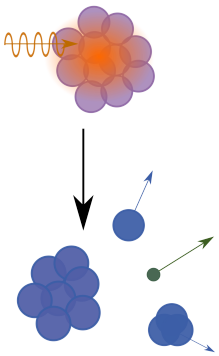
$\sigma_{A\gamma}$	$\epsilon_r < 1\,GeV$	$A\,\sigma_{p\gamma}^{\text{Sophia}}$	$A^{\alpha}\,\sigma_{\text{univ}}$, $\alpha = 1$	
	$\epsilon_r > 1\,GeV$		$A^{\alpha}\,\sigma_{\text{univ}}$, $\alpha = \alpha(\epsilon_r)$	
$\sigma^{\text{incl}}_{A\gamma\to X}$	Fragments produced	n/p and $A-1$	n/p and disintegration products at E^*	$A_{\text{fr}} \in [1-4, A/2...A-1]$ (see Appendix 4.2.3)
	Fragment's multiplicity	Always 1 (for any fragment produced)	Combination of disintegration model and Sophia	Empirical formulas and nuclear thermostatistics (see Appendix 4.2.3)
	$\sigma^{\text{incl}}_{A\gamma\to\pi}$	$A\,\sigma^{\text{incl, Sophia}}_{p\gamma\to\pi}$		$A^{\alpha_\pi}\,\sigma^{\text{incl}}_{\pi}$ (see Appendix 4.2.2)

Table 4.1: Comparison of photomeson models and schematics of the related physical picture. The nuclei and nuclear fragments are represented as collections of circles (nucleons) with color related their role in the interaction (and fraction of the photon energy they receive): blue, spectator nucleons (no extra energy received, boost conservation); purple, non-active participants (some extra energy received); and orange, active participants (receive most of the energy, direct interaction). Green smaller circles represent pions. Table and diagrams taken from Morejon et al. (2019a).

4.2.1 Total photonuclear cross section

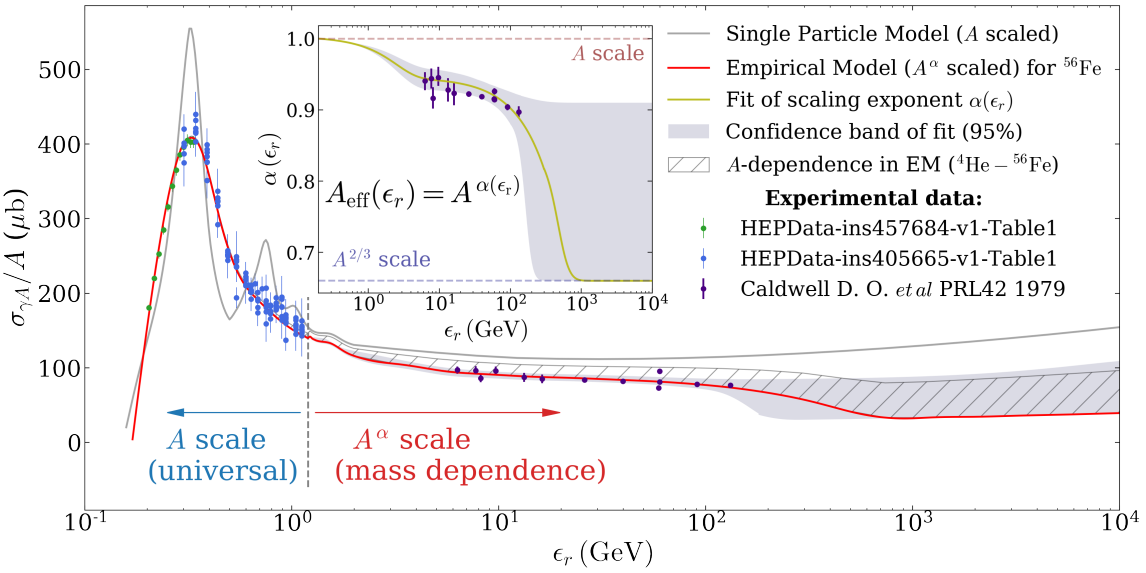

Figure 4.3: The inelastic photonuclear cross section divided by A as a function of photon energy in the nucleus' rest frame. Data points from a broad range of nuclei with masses $A = 7 - 208$ show a universal behavior at low energies and a mass dependence at higher energies. The red curve is the ^{56}Fe cross section as implemented in the EM, and illustrates the typical shape in the model. The gray curve correspond to the SPM, common to all nuclei and identical to the photo-nucleon cross section $\sigma^{\rm SPM}_{A\gamma}/A = \sigma_{N\gamma}$. The EM cross section has a mass scaling with A^α energy for $\epsilon_r > 1\,$GeV (see Eq. 4.9). The dependence $\alpha(\epsilon_r)$ (yellow curve in the insert plot) is a linear function fitted to data (confidence band shown as gray area). The extrapolation to lower energies is a sigmoid which takes the low energy value $\alpha_{\rm low} = 1$. The extrapolation to higher energies is a sigmoid which tends to the theoretical limit $\alpha_{\rm lim} = 2/3$). The hashed region represents the variation of the cross section per nucleon in EM ($\sigma^{\rm EM}_{A\gamma}/A = A^{\alpha-1}\sigma_{N\gamma}$) for the mass for the mass range $A = 4 - 56$. Figure taken from Morejon et al. (2019a).

As discussed in Section 4.1, the nuclear environment (also referred to as "medium effects") changes the physics above the pion threshold energies compared to the free nucleon case. Figure 4.3 shows the inelastic cross section divided by A as a function of energy. The curves corresponding to protons (SPM curve) and to ^{56}Fe (EM curve) are compared to photonuclear data compiled from experiments with various target nuclei (Bianchi et al., 1996, MacCormick et al., 1997, Caldwell et al., 1979). At $\epsilon_r \lesssim 1\,$GeV, the green circles correspond to light nuclei ($A = 2 - 4$) and the blue circles to $A = 7 - 208$. Within the errors of the data, a scaling with A appears justified. However, the shape of the curve is different compared to $\sigma_{p\gamma}$, with only one

pronounced resonance peak in place of the $P_{33}(1232)$ resonance (Δ-resonance), being 20% wider at half height and 30% lower at the peak. The widening has been explained with the D*elta*-hole model (Koch et al., 1984), where medium effects are taken into account by including the Fermi motion of nucleons, the Pauli blocking restricting decay channels and the Δ-N interactions. The nucleon resonances at energies beyond 500 MeV are not visible even for small masses such as Be and C (Bianchi et al., 1993, Anghinolfi et al., 1993).

For $\epsilon_r \gtrsim 1\,\mathrm{GeV}$ the photonuclear cross section per nucleon is reduced due to the shadowing effect. This reduction is dependent on the nuclear mass, and has been successfully understood within the Vector Meson Dominance model (VMD), which describes the photon's wave function as a superposition of mesonic states (ρ, ω, φ) (Weise, 1974, Bianchi et al., 1999, Schildknecht, 2006) that interact hadronically with the nucleus. At higher energies, where the photon can resolve the partons in the nucleus, the parton distribution function is predicted to be high enough that the nucleus becomes opaque to photons, leading to a theoretical limit similar to that of hadron-nucleus interactions $\alpha_{\mathrm{lim}} = 2/3$ (Kaidalov, 2002). The mass scaling is typically parametrized in the literature as a power of the nuclear mass:

$$\sigma_{A\gamma}(\epsilon_r) = A_{\mathrm{eff}}(\epsilon_r)\,\sigma_{p\gamma}(\epsilon_r) = A^{\alpha(\epsilon_r)}\,\sigma_{p\gamma}(\epsilon_r). \tag{4.9}$$

In the EM the cross section is parametrized parametrization with the following additional elements:

- For $\epsilon_r < 1$ GeV a "universal curve" (spline fit of data points in Figure 4.2) scaled by A ($\alpha = 1$) is used. This reflects the universal shape of the cross section per nucleon exhibited by nuclei of a wide range of masses.

- For $\epsilon_r \geq 1$ GeV the photo-nucleon cross section is calculated with Sophia , scaled by an energy dependent exponent $A_{\mathrm{eff}} = A^{\alpha(\epsilon_r)}$. The energy dependence of the exponent is shown in the insert of Figure 4.2.

The data provided by Caldwell et al. (1979) are provided as $f_A(\epsilon_r) = A_{\mathrm{eff}}(\epsilon_r)/A$ for different nuclei (C, Cu, and Pb). Considering the parametrization with mass in Eq. 4.9, the exponent values α are calculated from the data using $\alpha(\epsilon_r) = 1 + \ln f_A(\epsilon_r)/\ln A$ (purple points in the insert of Figure 4.3). A linear fit was performed to find the energy dependence, and extrapolated towards the shadowing limit $\alpha_{\mathrm{lim}} = 2/3$ for high energies (yellow curve in insert). The shaded area contains the 95% confidence interval of the fit in the region where data are available, and has also been extrapolated to higher energies: the upper band with a constant value, the lower band with a transition towards $\alpha_{\mathrm{lim}} = 2/3$ (Figure 4.3).

The mass scaling dependence with energy introduced in th EM at higher energies results in an

A-dependence of the cross section per nucleon $\sigma_{A\gamma}/A$. The hashed region in Figure 4.3 represents this mass dependence for the range of masses $A = 4 - 56$, where the upper line corresponds to the smaller mass and the lower to the larger mass.

4.2.2 Photoproduction of pions off nuclei

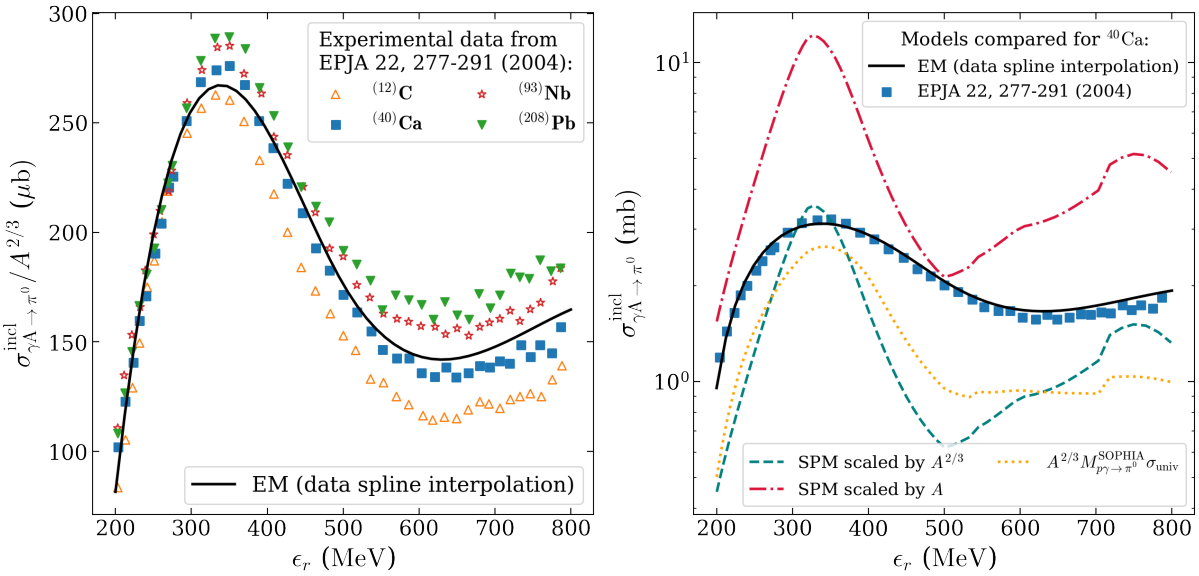

Figure 4.4: The figure shows the inclusive π^0 photoproduction cross section data compared to different parametrizations. On the left, the cross sections are divided by $A^{2/3}$ as a function of the photon energy, and the data points are taken from Fig. 9 by Krusche et al. (2004a). The overall shape is similar for nuclei with different masses, and it is represented with a unique curve (solid black, spline interpolation of the data) which is implemented in the EM. On the right, the data and EM inclusive pion photoproduction off ^{40}Ca are shown with other parametrizations. The SPM curve with $A^{2/3}$ scaling (dashed blue) is too low, and with A scaling (dot-dashed red) leads to overproduction. The total cross section per nucleon (universal curve $\sigma_{\rm univ}$) scaled by the pion multiplicity (dotted orange) $M^{\rm SOPHIA}_{p\gamma\to\pi^0}$ is also not suitable to describe the data. Figure taken from Morejon et al. (2019a).

The photoproduction of pions off nuclei is very sensitive to nuclear medium effects near threshold energies (Nagl et al., 1991). The interaction of the photon can occur via a "quasi-free" process, where one nucleon and the pions produced are ejected while the rest of the nucleus is unaffected. However, the pion(s) produced inside the nucleus interact with the surrounding nucleons with a strong dependence on their kinetic energy. Pions interact weakly with nucleons inside the nucleus for kinetic energies below ~ 40 MeV, and exhibit a resonance around kinetic

energies $50 - 100$ MeV which depends on the nuclear mass (Lee and Redwine, 2002). This effect is also evidenced in the photoproduction of pion pairs (Krusche, 2011), where the mass scaling of the cross section decreases from A to $A^{2/3}$ as the photon energy becomes large enough to produce pions with kinetic energies above ~ 40 MeV. An effective description for the mass scaling (Krusche et al., 2004b) can be achieved by separating "surface" and "volume" contributions, but such a description is hard to generalize for a broad range of nuclear masses.

Pion photoproduction off nuclei can be calculated with existing codes using Monte Carlo techniques in a cascade scenario (CRISP (Deppman et al., 2004)), or in terms of transport equations (GiBUU (Buss et al., 2012)). These simulations can be set up to have a good overall agreement with data. However, a general table for a wide range of nuclear species is computationally expensive and at the same time, the details of pion emission from each species are usually less important in astrophysical simulations compared to the uncertainties of nuclear composition. To keep the EM description of the pion photoproduction off nuclei as simple as in the SPM, the same shape for the inclusive cross section is used for all nuclei with a mass dependence and scaling coefficient $\alpha_\pi(\epsilon_r)$.

Figure 4.4 (left) shows the inclusive π^0 photoproduction as a function of incident photon energy ϵ_r for energies below ~ 1 GeV. The data were measured for different nuclei and normalized to $A^{2/3}$ (values reproduced from Fig. 9 by Krusche et al. (2004a)). The similarities in the curves point to a dominating "surface"-like mass scaling ($A^{2/3}$) rather than a 'volume"-like mass scaling (A). The systematic differences between the different curves are due to second order processes which scale with volume like multi-pions produced at low kinetic energies (Krusche et al., 2004b). The data have been fit with a spline (black solid curve), which represents the inclusive pion production cross section fit to all nuclear masses assuming a scaling with $A^{2/3}$. Figure 4.4 (right) compares the ^{40}Ca pion production cross section with different parametrizations. The SPM curve with A scaling (dot-dashed red line) predicts on average more than twice the number of pions compared to data (blue squares), whereas when using $A^{2/3}$ scaling (dashed blue) it leads to less than half. The total cross section per nucleon (universal curve σ_{univ}) scaled by the pion multiplicity per nucleon $M^{\text{Sophia}}_{p\gamma\to\pi^0}$ and a $A^{2/3}$ mass scaling (dotted orange) underestimates data, as well. The spline fit to all available data in Figure 4.4 (left) scaled by $A^{2/3}$ describes the pion production sufficiently well.

At higher energies heavier mesons start playing a role in the final states, affecting the simplified scaling assumption. For example, studies of photoproduction of η mesons up to 2 GeV (Mertens et al., 2008) find consistency with a $A^{2/3}$ scaling when the η is produced with kinetic energies sufficiently above threshold, demonstrating strong absorption through FSI. These type of effects are currently studied but the theoretical description is not yet complete (Dieterle et al., 2015, The A2 Collaboration, 2016). However, as the photon energy increases such effects are less important,

and have been shown to become irrelevant for photon energies beyond 50 GeV (Bianchi et al., 1999) where the production of pions is consistent with A scaling.

Our inclusive description with a mass scaling coefficient does not capture the complexity of the exclusive final states. Hence, our model follows the available data that suggests a $A^{2/3}$ scaling near threshold with a common curve for all species of nuclei, and is extended to higher energies by allowing the exponent to increase towards the limit value 1.

The pion photoproduction off nuclei in the EM is, therefore, parametrized as $A^{\alpha_\pi(\epsilon_r)}\sigma_\pi^{\text{incl}}$ where $\sigma_\pi^{\text{incl}}(\epsilon_r)$ is an inclusive cross section for π^+, π^- and π^0 production, as described below. Below 1 GeV $\sigma_\pi^{\text{incl}}(\epsilon_r)$ is derived from data: the form of $\sigma_{\pi^0}^{\text{incl}}$ is obtained by fitting a spline to the experimental values (black curve in Figure 4.4). For charged pions, their multiplicities are adjusted proportional to the production ratio off nucleons as taken from Sophia :

$$\sigma_{\pi^\pm}^{\text{incl}}(\epsilon_r) = \frac{M^{\text{Sophia}}_{N\gamma\to\pi^\pm(\epsilon_r)}}{M^{\text{Sophia}}_{N\gamma\to\pi^0}(\epsilon_r)}\sigma_{\pi^0}^{\text{incl}}(\epsilon_r)\,. \tag{4.10}$$

Above 1 GeV the EM curve is extended as in the SPM but with a smooth transition from $A^{2/3}$ scaling to A scaling with photon energy (see Figure 4.5) at around 50 GeV:

$$\sigma_{A\gamma\to\pi}^{\text{incl}} = A^{\alpha_\pi(\epsilon_r)}\sigma_\pi^{\text{incl}} = \begin{cases} A^{\alpha_\pi(\epsilon_r)}\sigma^{\text{Sophia}}_{N\gamma\to\pi} & \text{for } 1\,\text{GeV} < \epsilon_r < 50\,\text{GeV} \\ A\sigma^{\text{Sophia}}_{N\gamma\to\pi} & \text{for } \epsilon_r > 50\,\text{GeV} \end{cases}, \tag{4.11}$$

satisfying also the relations in Eq. 4.10.

As demonstrated in Figure 4.5 the energy dependence of the pion scaling exponent $\alpha_\pi(\epsilon_r)$ is derived from experimental data (Airapetian et al. and The HERMES Collaboration, 2001, Airapetian et al., 2003, 2007). The data has been obtained in deep inelastic scattering experiments measuring the semi-inclusive hadron production from the interaction of virtual photons with nuclei. The reported magnitude is the multiplicity ratio, which describes ratio of pion production per nucleon in a nucleus X to that in Deuterium D (see Eq. 4.12).

$$R_M^\pi(\epsilon_r) = \left(\frac{\sigma_{A_X\to\pi}^{\text{incl}}}{A_X}\right) / \left(\frac{\sigma_{A_D\to\pi}^{\text{incl}}}{A_D}\right). \tag{4.12}$$

It follows from Eq. 4.11 that the EM the multiplicity ratio is related to the photon energy nucleus mass and the scaling exponent as:

$$R_M^\pi(\epsilon_r) = \left(\frac{A_X}{A_D}\right)^{\alpha_\pi(\epsilon_r)-1}. \tag{4.13}$$

Below 1 GeV, the scaling exponent is fixed to 2/3 as suggested by data in Figure 4.4. The multiplicity ratio data, from different nuclear species, show a sharp increase of the scaling exponent in the interval from $1-3\,\mathrm{GeV}$. A spline fit to the entire energy range (dash-dotted gray curve in Figure 4.5) underestimates data from $4-10\,\mathrm{GeV}$. For this reason the model joins the the two energy ranges below 3 and $4-22\,\mathrm{GeV}$ using a sigmoid function (dashed black line). This curve applies to all pion species, since they are produced in equal amounts (Airapetian et al., 2003).

The energy redistribution of pions (differential cross sections, see Eq. 3.20) used are those sampled from Sophia for free nucleons, which means that any modification to the angular distributions resulting from the nuclear medium is neglected.

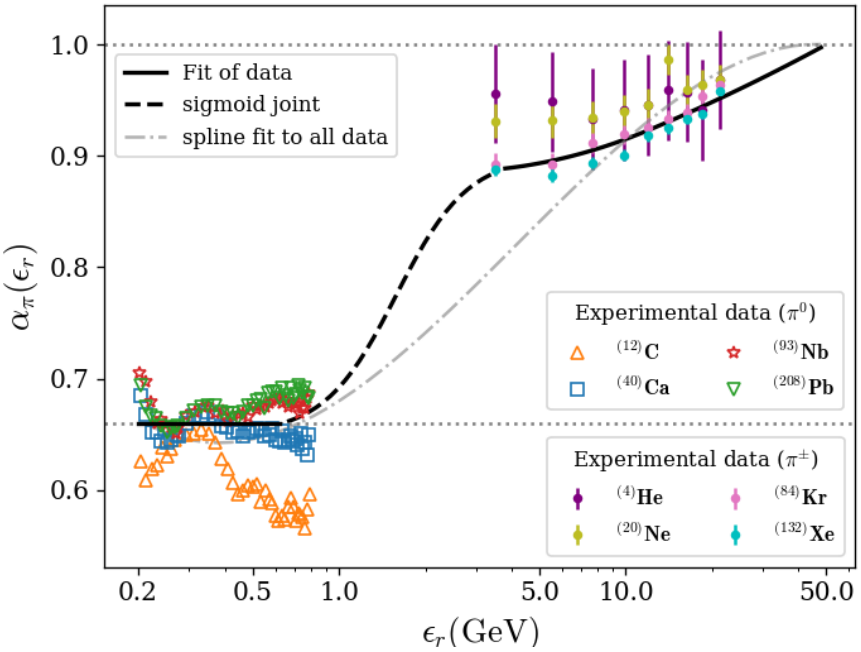

Figure 4.5: Energy dependence of the scaling exponent in the EM parametrization of the pion production inclusive cross section. The data values have been calculated from hadron multiplicity ratios reported by Airapetian et al. and The HERMES Collaboration (2001), Airapetian et al. (2003, 2007). The production of different pion species is even (Airapetian et al. and The HERMES Collaboration, 2001, Airapetian et al., 2003), therefore we use data from all of them to derive a unique $\alpha_\pi(\epsilon_r)$. Figure taken from Morejon et al. (2019a).

4.2.3 Nuclear fragmentation

In the SPM a photonuclear interaction of a nucleus with mass A always results in the loss of one nucleon per interaction. Hence, the final state always includes a remnant nucleus of mass $A-1$ that does not further disintegrate. In the photomeson regime nuclear breakup is governed by several mechanisms that lead to a more complex final state, including the emission of multiple nucleons, light fragments and a distribution of remnant nucleus masses. We consider two physical approaches to model this effect:

Residual Decay Model (RDM): The initial photon-nucleon interaction is modeled in the same way as in the SPM, assuming a quasi-free target nucleon. The motion of the nucleon through the nuclear medium results in an average energy loss, proportional to the nuclear radius (Abrasion-Ablation hypothesis). This energy left in the residual nucleus with mass $A-1$ is an excitation energy which can been estimated as $\epsilon^* = 17\,\mathrm{MeV}(A-1)^{1/3}$ (Rachen, 1996). The subsequent de-excitation proceeds through a re-scattering, or an equivalent interaction a photon with the energy $\epsilon_r = \epsilon^*$ with the remnant nucleus $(A-1)$. The typical energies for the range of masses are close to the GDR regime, for which the multiplicity distributions for final state particles have been obtained from a statistical, Hauser-Feshbach based model Talys (Koning et al., 2005) that uses combinations different nuclear models to describe the disintegration. These tabulated cross sections have been previously discussed by Boncioli et al. (2017). The inclusive cross section in the RDM for producing the fragment k from the interacting species j is calculated by normalizing the multiplicity of the fragments produced in the disintegration model at ϵ^* to the total cross section of the interacting species σ_j where δ_{kN} (1 if k is proton or neutron and zero otherwise) accounts for the additional nucleon emitted in the first photon interaction.

Empirical Model (EM): The photonuclear interaction is more complex, and often involves multiple nucleons and intermediate fragments. The production of nuclear fragments is very dependent on the absorption mechanism and the consequent energy transfer to the rest of the nucleus (intra-nuclear cascade). The average production of masses can be modeled using empirical formulas previously obtained by Terranova and Tavares (1994) and reproduced in Appendix A.1.1. The formulas estimate the average cross sections for producing certain fragments in the energy range $0.2 \lesssim \epsilon_r \lesssim 1\,\mathrm{GeV}$. Employing those relations and additional considerations from thermostatistics, the inclusive cross sections for a broad range of nuclear fragments have been produced (see Appendix A.1.1). Schemes of the physical scenarios and a summary of the components of these models are shown in the Tab. 4.2 in comparison with the SPM.

In Figure 4.6 a comparison between of the mass distribution of fragments is shown for two interacting nuclei: ^{14}N (left) and ^{56}Fe (right). The multiplicities are calculated from the total

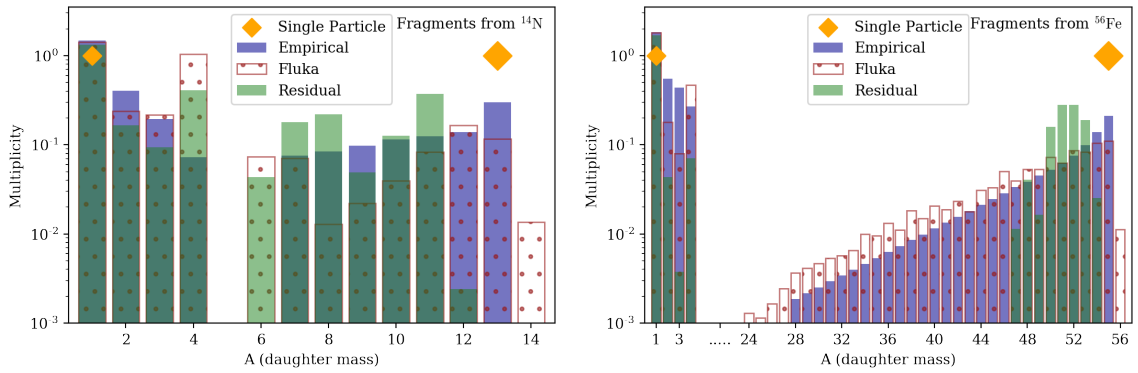

Figure 4.6: The mass distribution of the daughter fragments for different interacting nuclei ^{14}N (left) and ^{56}Fe (right). The multiplicity is the average number of particles produced of certain species (see Eq. 4.1). The distribution corresponding to the Residual Decay Model (green) is peaked as is characteristic of evaporation-dominated disintegration. The distribution corresponding to the Empirical Model (blue) is more spread its shape is in better agreement with that obtained in Fluka (Ferrari et al., 2005) which is a detailed a Monte Carlo code based on data and theory (red outline). In the SPM masses 1 and $A-1$ (orange diamonds) are always produced from species with mass A. Figure taken from Morejon et al. (2019a).

cross section of the interacting species j and the inclusive cross section for production of species k:

$$M_{j\to k} = \frac{\sigma^{\text{incl}}_{j\to k}}{\sigma_j} \tag{4.14}$$

which is equivalent to Eq. 4.1 and represents the mean number of particles of a certain species produced per interaction. The species are grouped by mass and the multiplicity of the mass group is the sum of the multiplicities of all species with the same mass. The EM values are shown in solid blue, and the RDM in solid green. Additionally, the values obtained with Fluka (Ferrari et al., 2005) are shown as reference. In Fluka , detailed Monte Carlo simulations are combined with state of the art theory and nuclear data to obtain the photonuclear interaction and the subsequent production of secondaries. The shape of the EM is in better overall agreement with Fluka than the RDM. The implicit assumptions in the RDM are reflected in the narrower mass distribution which is a typical shape produced in the disintegration at lower energies around the GDR, where the disintegration model for the residual nucleus is sampled. Experimental results for the disintegration at energies corresponding to the photomeson regime point to processes like spallation and fission (di Napoli et al., 1976, 1978) (see Figure A.1) which are explicitly simulated in Fluka whereas in EM the mass distribution is fixed for all species of the same mass. Figure 4.7 shows a comparison of EM and Fluka to data by di Napoli and Terranova

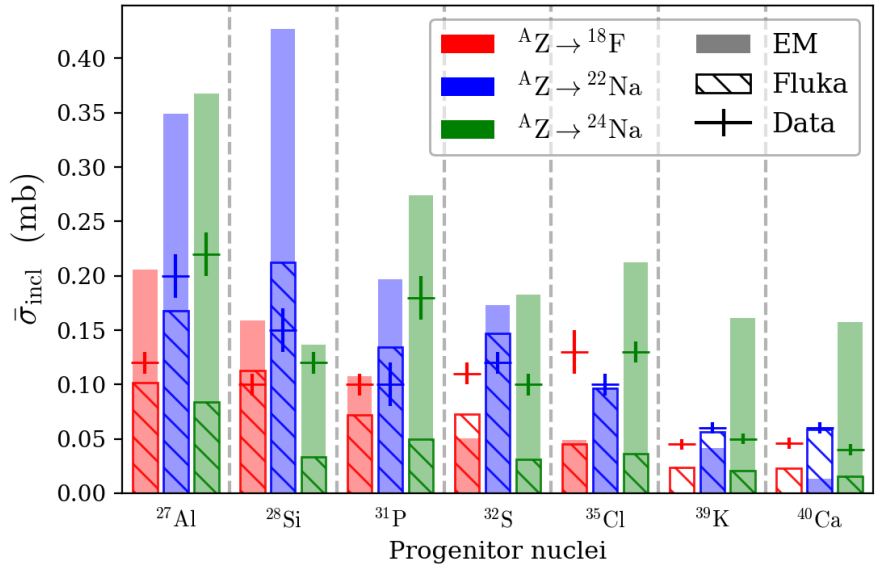

Figure 4.7: Comparison of the cross sections averaged over the range $0.3 - 1$ obtained from Fluka , the EM, and experimental data by di Napoli and Terranova (1974). EM performs similar to Fluka . Note that both models are have not been specifically optimized for these particular isotopes. Figure taken from Morejon et al. (2019a).

(1974) where the average production over photon energies $0.3 - 1$ GeV is measured for multiple nuclei. The corresponding values from the EM and Fluka are within a factor 1-3 of the experimental values. For this case, the EM performs similarly to a more elaborate nuclear code. The SPM can not be even compared in the same way, since it produces only one $A-1$ fragment.

The differential cross sections (energy redistributions) of the fragments from the statistical fragmentation in the RDM and EM follow the relation in Eq. 4.2 (boost conservation). The redistribution for secondaries produced directly in the photon-nucleon interaction are sampled from Sophia (see Eq. 3.20). A fully detailed description of the model's implementation is located in Appendix A.1.

4.3 Impact in astrophysical scenarios

The characteristics of our new model impacts the production of UHECRs and neutrinos, depending on the parameters of the sources. We show in the following two representative example sources where the importance of the photomeson production have been already highlighted: GRBs (Biehl et al., 2018a) and TDEs (Biehl et al., 2018c). The examples have been chosen such

that photomeson processes dominate the disintegration at the highest energies.

GRBs are the most energetic electromagnetic outburst class. Shells of plasma emitted by the central engine can create internal shocks that become acceleration sites for charged particles. The interactions of those particles with the target photons in the so-called prompt phase can result in the production of a significant number of neutrinos. As a consequence, GRBs are candidate sources for UHECRs and neutrinos, although existing analyses already constrain some regions of the parameter space for GRBs (Aartsen et al., 2017c) multimessenger models.

In this work we use an example by Biehl et al. (2018a), where the interactions in the source are simulated with NeuCosmA in the context of a one-zone model, meaning that the collisions of plasma shells cluster at the same collision radius R. Provided that baryons are present in the source, the density of the radiation triggers a nuclear cascade in which nuclei lighter than the primary are produced due to photodisintegration and photomeson production, impacting the mass composition of in-source and ejected cosmic rays. In Biehl et al. (2018a), several qualitative cases have been distinguished: for a high radiation density in the source, the nuclear cascade strongly develops ("optically thick case") and produces a high flux of nucleons, which dominate the neutrino production. If the radiation density is low ("empty cascade"), the nuclear cascade does not develop and the neutrino flux is dominated by photomeson production of the primary nuclei. In the intermediate case ("populated cascade"), the nuclear cascade develops and neutrinos are efficiently produced off primary and secondary nuclei. The different cases can be quantitatively distinguished by the optical thickness to photohadronic interactions at the highest energies.

These different cases relating the degree of disintegration to the multimessenger production as introduced by Biehl et al. (2018a) for GRBs, can be applied to other source classes (Biehl et al., 2018c). A special case are jetted Tidal Disruption Events (TDEs), which have been proposed as possible UHECR sources (Farrar and Piran, 2014). In this scenario, a star is gravitationally disrupted in the vicinity of a black hole by tidal forces, generating a jet in which a nuclear cascade similar the GRB can develop.

Tab. 4.2 presents the source parameters for the models considered here. The luminosity L and collision radius R define the photon energy density in the source, together with the Lorentz factor of the shells G. The duration T can vary greatly among source classes, with consequences for the detection capability of different experiments. The baryonic loading ξ is defined as the energy injected as baryons over the energy injected in photons, and it is fixed to a reference value here. The efficiency of the acceleration controls the maximum energy of acceleration. The spectrum of the GRB is typically described by a broken power law with a spectral break at 1 keV in the observer's frame and spectral indices $\alpha = -2/3$ (-1) and $\beta = -2$ below and above the break energy for TDEs (GRBs), respectively. Although the photodisintegration through excitation

Source	TDE (Biehl et al., 2018c)	GRB (Biehl et al., 2018a)
Gamma factor	$G = 10$	$G = 300$
Redshift	$z = 0.001$	$z = 2$
Duration	$T = 10^6$ s	$T = 10$ s
Luminosity	$L_X = 10^{47}$ erg/s	$L_\gamma = 10^{53}$ erg/s
Collision Radius	$R = 10^{9.6}$ km	$R = 10^{8.3}$ km
Injected isotope	^{14}N	^{56}Fe
Acceleration efficiency	$\eta = 1$	$\eta = 1$
Baryonic loading	$\xi = 10$	$\xi = 10$
Target photon spectrum parameters in the shock rest frame	$\varepsilon'_{X,\mathrm{br}} = 1\,\mathrm{keV}$ $\varepsilon'_{X,\mathrm{min}} = 10^{-6}\,\mathrm{eV}$ $\varepsilon'_{X,\mathrm{max}} = 300\,\mathrm{keV}$ $\boldsymbol{a = -2/3}$, $b = -2$	$\varepsilon'_{\gamma,\mathrm{br}} = 1\,\mathrm{keV}$ $\boldsymbol{\varepsilon'_{\gamma,\mathrm{min}} = 100\,\mathrm{eV}}$ $\varepsilon'_{\gamma,\mathrm{max}} = 300\,\mathrm{keV}$ $a = -1$, $b = -2$

Table 4.2: The source parameters shown were taken from the references (Biehl et al., 2018a,c). In the case of the GRB, the parameters for the Optically Thick scenario are shown; the ones for the other scenarios (Empty Cascade and Populated Cascade) are identical except for their luminosities $L_\gamma = 10^{49} erg/s$ and $L_\gamma = 10^{51} erg/s$, respectively. Parameters critical for the photomeson processes dominating at the highest energies are highlighted in boldface. Table taken from Morejon et al. (2019a).

of the GDR is the dominant process for UHECRs with respect to photomeson processes, the interplay of the spectral index of the photons with the GDR and photomeson regimes may favor the photomeson production at the highest energies, as for example in TDEs. The minimal cutoff of the photon spectrum in the source can also drastically reduce the GDR interaction length, as demonstrated already by Biehl et al. (2018a). The critical parameters influencing photomeson production at the highest energies are marked in boldface in the table. These parameters are especially important for the predictions of neutrino production.

4.3.1 TDE scenario

Let us focus on the TDE scenario first, see Figure 4.8. The slope of the photon spectrum at low energies reduces the photodisintegration rate at high energies (high energy protons interact with low energy photons), which means that the photomeson regime dominates the photohadronic interactions at the highest energies – as it is shown in the upper left panel of Figure 4.8. Here the impact of the cross section systematics is only significant beyond the maximal energy of the cosmic rays, which can be estimated by balancing the acceleration rate with the sum of the

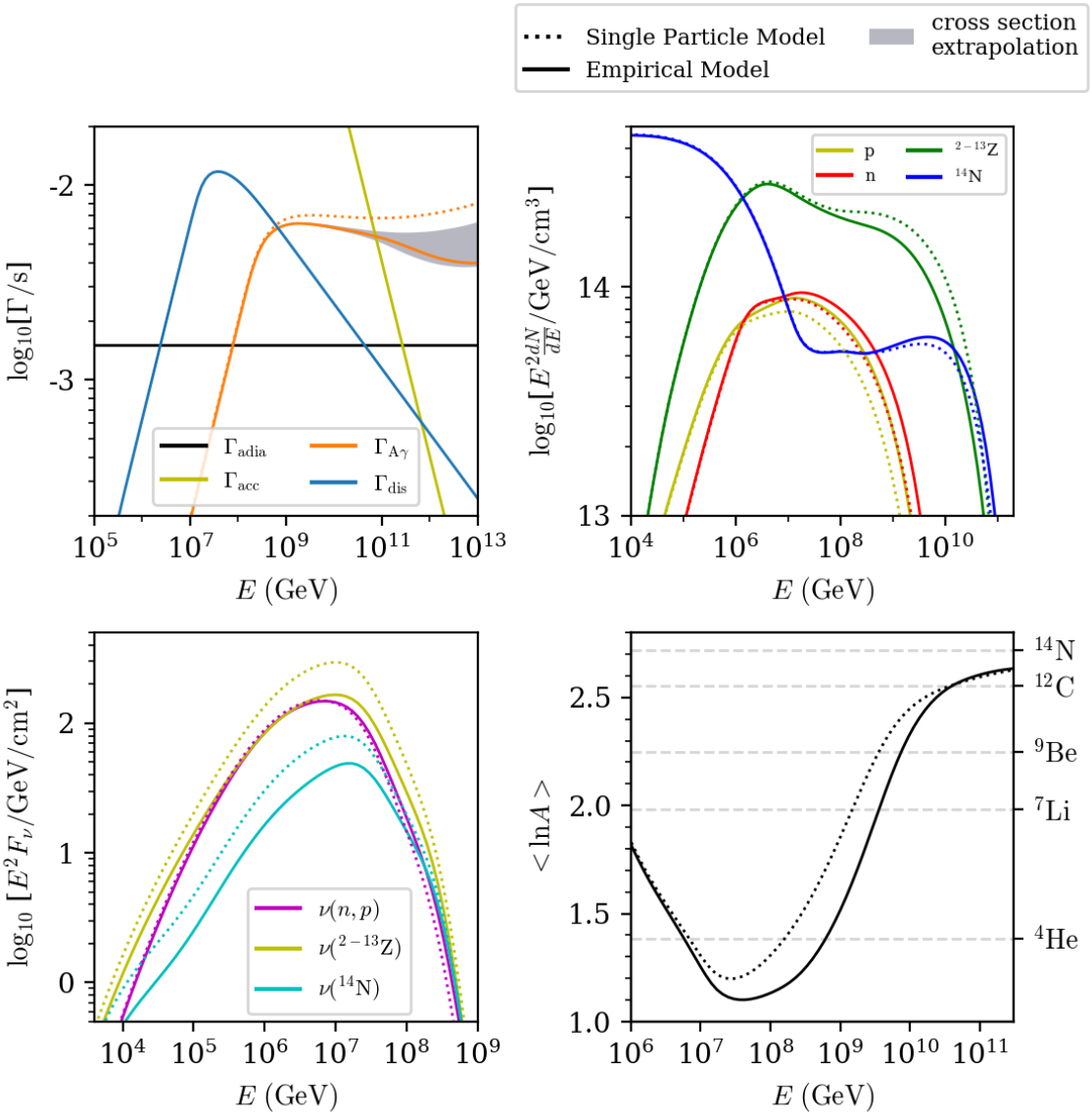

Figure 4.8: Comparison of the results using the new Empirical Model (EM) (solid curves) with the reference Single Particle Model (SPM) (dotted curves) in the TDE scenario from Biehl et al. (2018c); shaded areas refer to uncertainty in the cross section extrapolation. The different panels show: the leading process rates for the injected ^{14}N (upper left panel), the in source densities (upper right panel), the flux of neutrinos grouped by origin (lower left panel), and the averaged $\ln A$ of the in-source spectra, all as a function of the energy E in the observer's frame. Figure taken from Morejon et al. (2019a).

energy losses (acceleration is possible only when losses are subdominant). In the upper right panel, the effect of the lower cross section adopted in the EM with respect to the SPM is visible: the injected primary nuclei (blue) is less depleted in the EM, therefore less energy is injected in secondaries. On the other hand the the production of secondaries is distributed over a larger range of masses (see Figure 4.6) and the average mass of the secondaries is smaller than in the SPM, which implies a more efficient disintegration. The increase in the nucleons densities is the result of this more efficient disintegration of all the secondaries produced.

The neutrino production (see lower left panel) is mostly affected by the cross section scaling of the pion production; the heavier the primary, the larger the difference between the models. It is noteworthy that the SPM changes the qualitative observation that the neutrino production would be dominated by interactions of nuclei: In the EM, both contributions are similar in magnitude but nuclei dominate slightly at the highest energies. Overall the neutrino flux is depleted by a factor of 1.5 if the EM is used with respect to the SPM. The effect of the disintegration channels is appreciable in the $< \ln A >$ where the EM leads to a smaller cascade mass (lower right panel). This happens mainly at the intermediate energies range because of the conservation of the Lorentz factor of the nuclei in the photodisintegration process, and because the secondaries are produced at lower energies in proportion to their mass ratio to progenitor species (due to boost conservation). At the highest energies, where the primary nuclei density dominates, the composition is slightly heavier than in SPM due to the reduced interaction.

4.3.2 GRB scenario

For the GRB example, we follow (Biehl et al., 2018a). The luminosity and the collision radius reported in Tab. 4.2 correspond to a high radiation density, and the neutrinos are mainly given by the secondary nucleons produced in the nuclear cascade. In particular, we use the assumptions of Appendix B by Biehl et al. (2018a) for the photon spectrum of the source, in which a higher low-energy cutoff of the photon spectrum is investigated resulting in an suppression of photodisintegration rate with respect to the photomeson rate. The upper left panel of Figure 4.9 demonstrates how the changes in the cross section affect the interaction rates at energies above the maximum energy of acceleration, which means that the effects on the energy densities (upper right panel) are dominated by the redistribution channels of the secondaries. The impact on the more efficient nuclear disintegration (through a larger number of open channels) is also visible in the $\langle \ln A \rangle$ behavior (bottom right) which overall exhibits a lighter composition, reaching up to three times lower value compared to the SPM. The neutrino production (bottom left) is again dominated by the pion production scaling used in EM ($A^{2/3}$) in contrast with SPM scaling (A), and the effect is large because of the heavier primary mass compared to the TDE example.

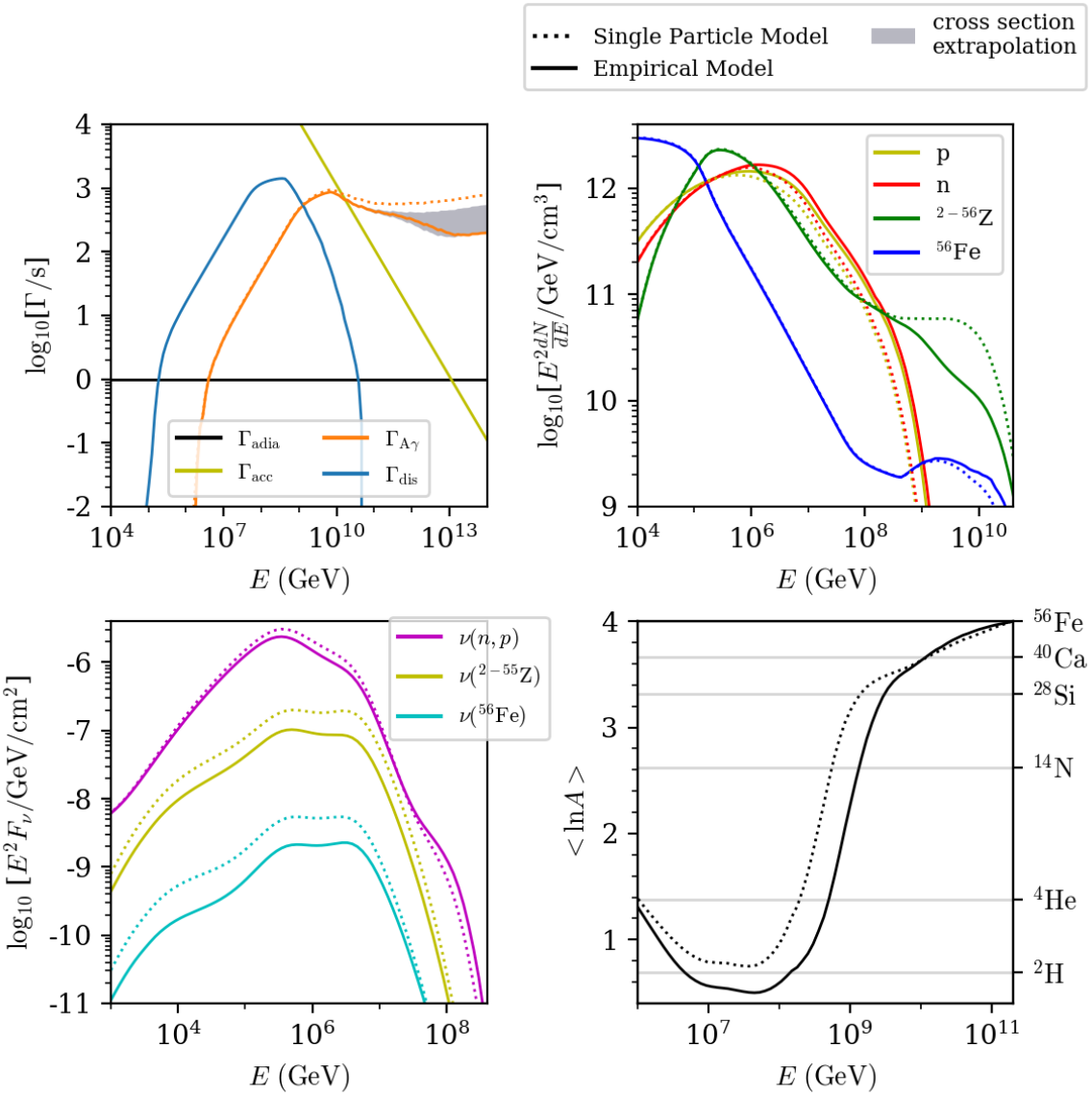

Figure 4.9: Similar to Figure 4.8, but for the GRB scenario with parameters shown in Tab. 4.2 by Biehl et al. (2018a), for the injected ^{56}Fe. Figure taken from Morejon et al. (2019a).

Figure 4.10 shows the impact of the change of the photomeson model in the neutrino fluxes, corresponding to different GRB luminosities identified with different nuclear cascade regimes. Note that, compared to the main text of (Biehl et al., 2018a), here the low energy photon cutoff has been applied to all examples. The largest differences are visible in the low and intermediate

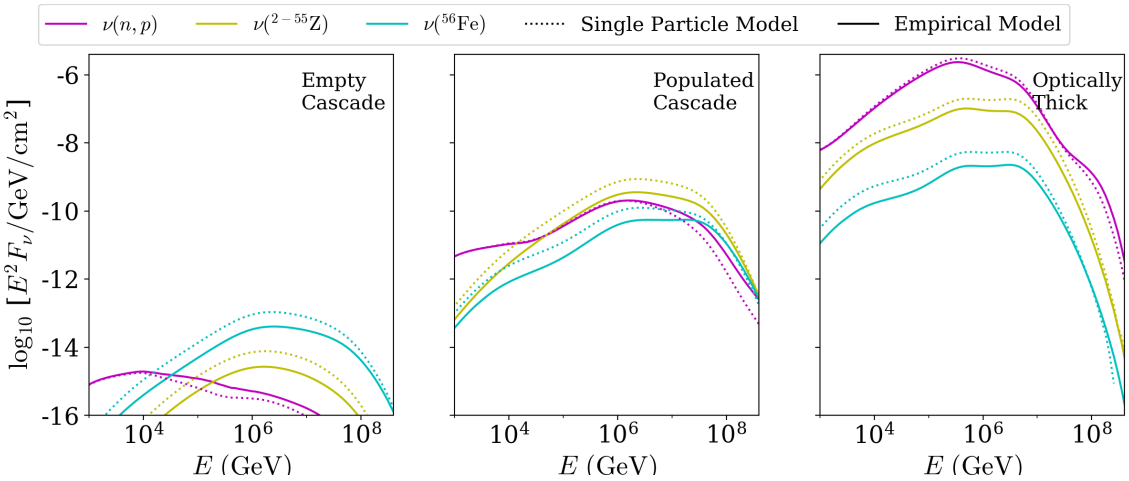

Figure 4.10: Neutrino production corresponding to different GRB luminosities and to SPM (dotted curves) and EM models (solid curves) for photomeson process. Figure taken from Morejon et al. (2019a).

luminosities, for which the neutrinos are mainly produced off (primary and secondary) nuclei. In the populated-cascade scenario (center), the smaller neutrino yields from the intermediate nuclei in the EM, change the leading production channel of the neutrinos. When using SPM in this intermediate case, the neutrino emission from secondary nuclei dominates the flux, whereas for the EM the contribution from nucleons is comparable to that from secondary nuclei.

4.4 Conclusions

A commonly adopted approach in the literature regarding photomeson interactions of UHECR nuclei (Single Particle Model, SPM) has been revised. Disagreements were found between the model results and experimentally obtained data. An improved photomeson model was introduced (dubbed Empirical Model, EM) that better models the interactions and has similar ease of use as the SPM. The impact of the EM was studied in astrophysical scenarios in which the photomeson processes are known to dominate at the highest energies (certain classes of GRBs and TDEs).

The SPM treatment views the nucleus as superposition of nucleons. The total inelastic cross section is assumed to scale with A or $A^{2/3}$. The disagreements of this model with available data have been presented. The EM improves on the SPM by using: a data-driven parametrization for the total inelastic cross section at low energies and a mass number scaling consistent with data and theory for high energies; a data-driven parametrization of the pion photoproduction cross section resulting in a $A^{2/3}$ scaling at the lower energies that accounts for nuclear medium effects

and final state interactions; a nuclear breakup model for the remnant nucleus based on existing empirical formulae for partial photo-emission mechanisms, resulting in a better agreement with distributions obtained from Monte-Carlo simulations, such as Fluka .

These modifications affect the photomeson interactions off nuclei in astrophysical environments, and we used two examples from the literature in which the photomeson regime is known to dominate the nuclear interactions at the highest energies. The GRB example resembles an effect from synchrotron self-absorption in which low energy target photons are suppressed that would otherwise disintegrate the UHECRs via Giant Dipole Resonance excitation. The TDE example has a broken power law target photon spectrum with a hard enough (low) power law index such that the photomeson production dominates at the highest energies. The EM affects the nuclear cascade in the source resulting in an ejected UHECR composition that is up to three times lighter, and a reduction of the neutrino flux by up to 50%. This is a result of the additional production channels included which disintegrate nuclei faster per interaction compared to the SPM. The EM impact on the neutrino flux stronger (in contrast to SPM) because it depends on the mass of the isotope(s) due to the different scaling. This implies that neutrino emission becomes more sensitive to the choice of the injection composition into an internal-shock GRB model and the degree of the nuclear cascade. For high radiation densities in the optically thick case, neutrino production is dominated by nucleon interactions, and hence the impact from the new model is low. Consequently, the strongest effects will occur for the populated and empty nuclear cascade cases with heavy injection isotopes, which, however, have a smaller neutrino production efficiency compared to cases in which the cascade develops fully. The impact on the UHECRs is smaller and only expected in environments where the photomeson regime dominates the nuclear disintegration. A prominent counter-example is, for instance, cosmic ray transport in the extragalactic space. In such scenario the main interaction process is the photodisintegration via interactions with the CMB and the photomeson interactions are much reduced. The corresponding cosmogenic neutrino flux contributions of nucleon and nuclei interactions at the peak is about the same (Heinze et al., 2019). This means that the neutrino flux may be even lower (by up to about 25%) in the present photomeson model.

Finally, note that the EM is based on a very small number of parameters and can be easily implemented for cross comparisons in any of the existing codes and calculation frameworks for radiation modeling of High Energy Particle Astrophysics. The tools for reproducing the model are available (Morejon, 2019b) and can be used for implementation in any framework simulating the interaction of UHECRs.

Chapter 5

Secondary photon emission from nuclear photointeractions

The interactions of UHECR nuclei with photons can lead to the production of isotopes in excited states. This can happen in to ways: when the photon energies exceed several keV in the nucleus rest frame, they can directly excite the nucleus to a higher nuclear energy level; or the photodisintegration process, discussed in previous chapters, can lead to the production of lighter secondary nuclei that are in unstable excited states. In either case, the subsequent decay of the excited nuclear levels produces photons with keV-MeV energies in the nucleus rest frame. As a result of the ultra-relativistic velocities of the UHECRs, the energy of these photons is highly boosted in the observer's rest frame, where it can reach TeV-PeV energies.

In this chapter, I present a framework for treating these secondary photons in UHECR interaction models. I first discuss the available experimental data, and then my implementation of these processes in existing astrophysical models. Finally, I discuss an astrophysical application of this model, namely the very-high-energy gamma-ray emission from the galaxy Centaurus A. While previous studies have claimed that these photons originate in photointeractions of ^{56}Fe accelerated in the source (Joshi and Gupta, 2013, Kundu and Gupta, 2014), with this more realistic model it can be shown that the processes at play are in fact more complex and must be modeled with a fully numerical approach. The model for photon emission from nuclear decays is my contribution to a project currently in preparation (Rodrigues et al., in development).

5.1 Photon emission from nuclear de-excitation

The nucleus, as a composite system of strongly interacting fermions, has a complex energy level structure. At excitation energies much lower than the average energy per nucleon of 8 MeV, the internal levels are distinctly separated and have a very narrow width. In the shell model of nuclei (Greiner and Maruhn, 1996) these levels correspond to individual excitations of nucleons analogous to individual electrons jumping to higher energy levels in the atomic model. De-excitation from these levels is only possible through the emission of a number of photons

carrying away a portion or all the excitation energy, which is in the order of hundreds of keV to a few MeV.

As the excitation energies approach the nucleon binding energy, the separation between nuclear excitation levels reduces and their widths increase. Eventually the nuclear energy states can be described by a continuous distribution rather than quantized levels, and the shell model is no longer applicable. De-excitation from these levels is possible through the emission of one or more photons, as in the case of lower energy levels, and additionally by the emission of a nucleon, usually a neutron. This is energetically possible due to the differences in binding energies between nuclides, which makes the transition between their ground states possible. Nevertheless, photon emission is the most likely de-excitation process below the binding energy of nucleons.

For excitation energies between 10-30 MeV collective modes like the giant dipole resonance (GDR) are the dominant excitation feature of the nuclear system. These resonances are broad features in the photoabsorption cross section described by isoscalar oscillations of the nuclear system. De-excitation of this state occurs mostly with the emission of nucleons because they can take away a larger fraction of the excitation energy, but also light fragments such as deuterium, tritium and helium nuclides. The emission of photons also occurs in this regime, albeit with lower probability because particle emissions are more effective in removing energy from the nucleus.

At excitation energies above 50 MeV, the spectrum of photons emitted depends on the process that populates the excited levels:

- When the excited state is populated through a collision between nuclei, the system thermalizes quickly and high-energy (10-20 MeV) photons are emitted. Immediately after thermalization, evaporated nucleons and lower-energy photons are also emitted with a characteristic spectrum (Van Der Woude, 1987). When the incoming projectile is a much smaller nucleus or a nucleon, the particle's momentum is absorbed by only a fraction of the system which is stripped off the remaining nucleus, leaving it with a rather small fraction of the incoming energy.

- If the excitation is due to the interaction with a photon of energy between 40-100 MeV, it can be successfully explained by assuming the photon interacts predominantly with a pair of coupled nucleons Odian et al. (***quasi-deuteron model***, 1956), Fuji (***quasi-deuteron model***, 1962).

- For photons above 140 MeV, the dominant process is that of ***meson photoproduction*** off single nucleons. This is an even more localized interaction, but can lead to nuclear break up if the photon energy is sufficiently above the pion production threshold. The fragments

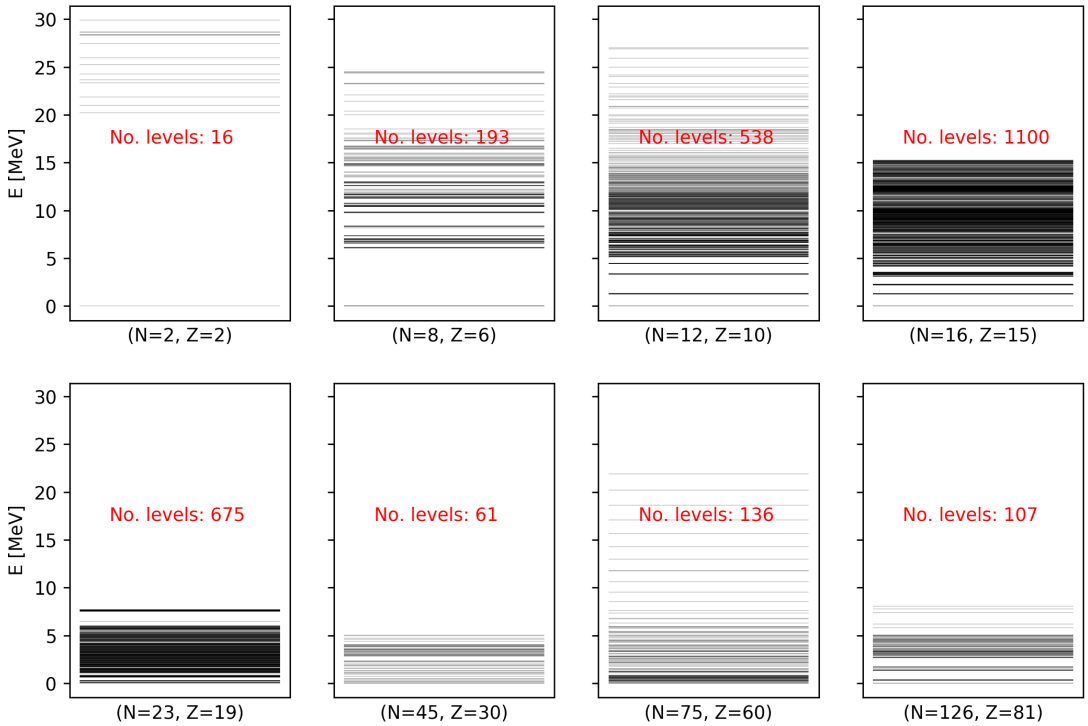

Figure 5.1: Nuclear energy levels (horizontal lines) of eight different isotopes chosen arbitrarily and given by the proton Z and neutron N numbers. Each level may have a small energy spread. Isotopes of lower mass (A) have less energy levels, with wider gaps and concentrated at higher energies, as opposed to lower mass nuclei, *i.e.* the excitation threshold of low mass nuclei is higher. Data taken from (Huang et al., 2017, Wang et al., 2017).

produced could also exhibit low excitation energies leading to de-excitation photons (see Chapter 4 and Appendix A).

In spite of these general guidelines, nuclear levels are in fact highly dependent on the particular nuclear species and on the properties of the initial and final quantum states involved in the interactions, such as angular momentum and parity. However, the energy and angular averaging employed in simulating UHECR interactions allows an effective description such as that presented above. Additionally, the intermediate nuclear states are usually short lived compared to most UHECR interactions' timescales, thus it is justified to consider the photons as immediate secondary products of the photonuclear interaction.

An illustration of the diversity of nuclear energy levels can be seen in Figure 5.1, where these levels are plotted for eight different nuclides representative of distinct nuclear mass ranges. One

general trend that can be seen is that for nuclei with lower masses the available excitation levels tend to be less densely populated, and the first excited level is generally higher compared to more massive nuclei. This is because as the larger the nucleon number, the larger the number of degrees of freedom in the nucleus with more available resonant modes in the system.

Nuclear interaction codes like Talys and Fluka combine tables of experimentally determined nuclear levels and nuclear theory to calculate the probability of de-excitation by photon emission. However, as discussed in Chapter 3, these codes are based on models and can differ from experimental data on a case-by-case basis.

Previous works in particle astrophysics that have taken into account photons from nuclear decays (Anchordoqui et al., 2007, Murase and Beacom, 2010, Aharonian and Taylor, 2010, Kundu and Gupta, 2014) make the following assumptions:

- the emitted photons have a unique energy in the range 1-3 MeV (independently of nuclear species)
- the photon multiplicity is 1-3 photons (also independently of nuclear species)
- the production cross section follows the same shape as the photonuclear cross section, and usually only photoabsorption at the GDR is considered
- photons are emitted with a unique boost (no redistribution in energy)

In reality, when a nucleus emits one or several photons through de-excitation, the probability distribution of the energy of these photons is given by the gamma strength function. Estimates of the gamma strength functions are tabulated, and can be found for example in the RIPL-2 (2006) handbook, which combines experimental data and nuclear models.

In Section 5.4 the overly simplified approach currently used in the literature will be compared directly to the one presented here, making the argument for the need of a more realistic photon emission model in astrophysical simulations.

5.2 A novel model for photon emission from nuclear decays

For the astrophysical treatment of secondary photons the dynamics of the photonuclear interaction can be reduced to averaged quantities, as discussed in Chapter 3. The models used in other works can be improved in several ways:

1. Improving the total cross sections
2. Including the photon energy distribution

3. Introducing an energy-dependent photon multiplicity

The first aspect affects the rate of production of photons and therefore the spectrum of photons produced. The second aspect affects directly the shape of the photon spectrum produced in the interactions and the range of energies, typically extending it to lower energies. The third aspect affects the yield at different photon energies in the nucleus rest frame. Therefore it is difficult to point to a unique aspect as the cause of an effect observed in simulations in the astrophysical context. However, this is an advantage because the model can make simple assumptions and still be consistent with a more detailed model. So, although the use of detailed codes like TALYS and FLUKA may be more accurate, a parametrized model may produce similar results of the effective photon production.

The disintegration photoproduction model (DisPhot) presented here will be parametrized in simple terms, and has the following characteristics:

Lorentzian model for the total cross section Based on the parameters published by Santonocito and Blumenfeld (2006) the cross section is simulated using a Lorentzian shape for the GDR

$$\sigma(\epsilon) = \sigma_0 \frac{\Delta_{GDR}/2}{(\epsilon - \epsilon_0)^2 + \Delta_{GDR}^2/4} \tag{5.1}$$

$$\epsilon_0 = 31.2A^{-\frac{1}{3}} + 20.6A^{-\frac{1}{6}} \text{ MeV} \tag{5.2}$$

$$\Delta_{GDR} = 4.5 + 3\left(\frac{N - M_{\text{low}}}{M_{\text{top}} - M_{\text{low}}} + \frac{Z - M_{\text{low}}}{M_{\text{top}} - M_{\text{low}}}\right) \text{ MeV} \tag{5.3}$$

with parameters formulas taken from Santonocito and Blumenfeld (2006). M_{top} and M_{low} are respectively the lower and higher nuclear magic numbers in relation to Z or N. The nuclear magic numbers are {2, 8, 20, 28, 50, 82}. From 50 MeV the quasi-deuteron contribution was included as in Terranova et al. (1989):

$$\sigma(\epsilon) = 6.1\frac{ZN}{A}\sigma_d(\epsilon)\exp\left(-\frac{D}{\epsilon}\right) \text{ mb} \tag{5.4}$$

$$D = 0.72A^{0.81} \text{ MeV} \tag{5.5}$$

$$\sigma_d(\epsilon) = 36\epsilon^{-1.37} \text{ mb} \tag{5.6}$$

where σ_d is the cross section for deuterons which was obtained by fitting the model to experimental data (Bernabei et al., 1986).

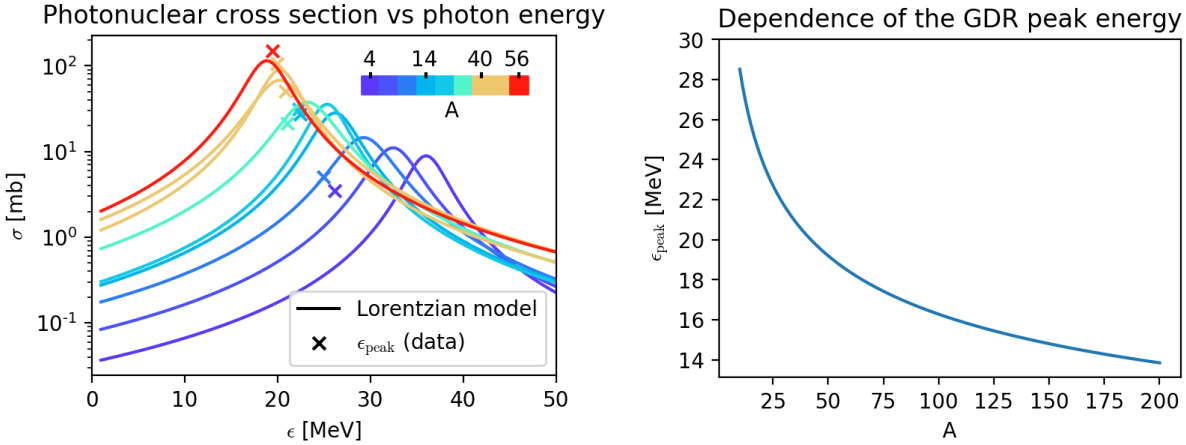

Figure 5.2: The Lorentzian model for the GDR region of the cross section. Left: cross section as a function of the photon energy. The colors of the curves indicate nuclei of different masses according to the color scale. The experimentally determined GDR peaks, shown as crosses, were taken from an Atlas of GDR parameters (Plujko et al., 2011). Right: evolution of the GDR peak of the distributions shown in the left plot with cosmic-ray mass number A.

The value of σ_0 is obtained normalizing to comply with the Thomas-Reiche-Kuhn sum rule,

$$\int_0^{140\,\mathrm{MeV}} \sigma(\epsilon) d\epsilon = 60 \frac{ZN}{A}\ (\mathrm{MeV}\cdot\mathrm{mb}). \tag{5.7}$$

The cross sections and peak energies are shown in Figure 5.2 where comparison with data is shown. The positions of the peaks are not so different from experimental values for masses $\gtrsim 20$ but differ importantly for lower masses. The cross sections in the photomeson regime are implemented as discussed in Chapter 4.

Photon multiplicity and energy distribution The photon energy in the nucleus rest frame and the multiplicities may depend on energy of the incoming photon and the nuclear species, nevertheless in this model average values are used for all energies. However, the photon energy is no larger than a few MeV and the number of photons no larger than 3. The reason is that the total energy emitted in photons should not be higher than the nucleon binding energy of about ≤ 8 MeV, since in that case nucleon emission channels are preferred. Furthermore, although individual values for each species could be chosen, the distribution function is insensitive to differences in those parameter within the same order of magnitude. Therefore, the average energy of the produced photon and multiplicity can be fixed at the same value for all nuclei.

The values chosen here are $\epsilon_m = 2$ MeV for the mean energy, and $M_\gamma = 3$ for the mean multiplicity. The photon energy distribution in the SRF is obtained by boosting the photons with sufficiently large Lorentz factor γ, where it is only a function of the relative energy in the nucleus rest frame. The photons of unique energy ϵ_m and isotropic emission in the nucleus rest frame, are distributed in the boosted frame over energies in the range $\epsilon \in (0, 2\gamma\epsilon_m]$ with a flat distribution. This distribution is important in logarithmic scale given the multi-scale nature of the resulting photon emissions detected in the astrophysical sources. Because of this, the small variations in ϵ_m within one order of magnitude, have negligible effect on the distribution, justifying the choice of a fixed value for ϵ_m in this model.

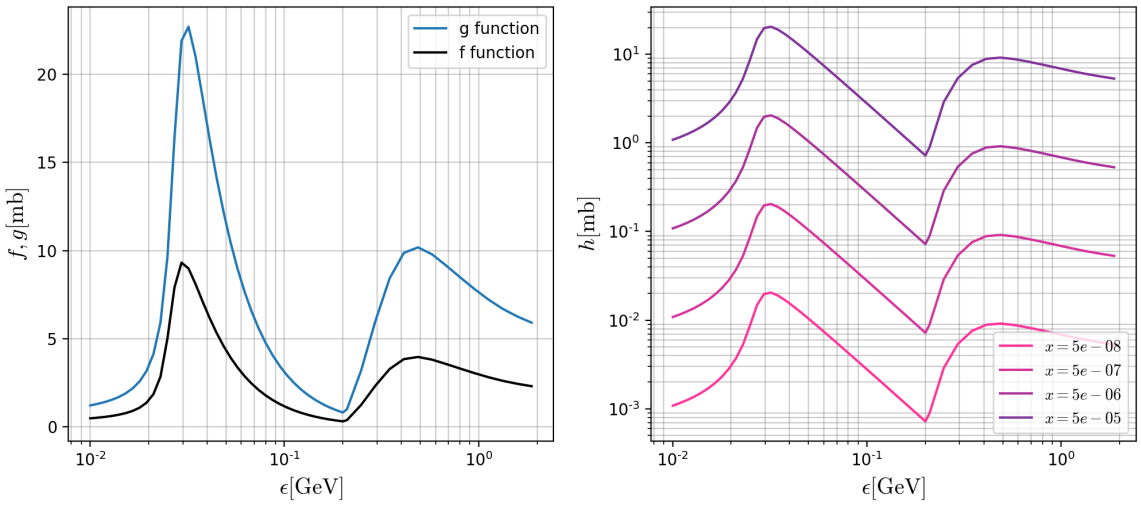

Figure 5.3: The computed response functions f, g and h (see Section 4.1). The values shown refer to a nucleus of ^{12}C. The photon production includes both photodisintegration and the photomeson regime.

Implementation of the model The DisPhot was implemented in NeuCosmA by computing the response functions f, g, h as described in Section 4.1. The functions are presented in Figure 5.3 for the species ^{12}C. The values of $f(y)$ are calculated with the total cross section using Eq. 4.3, and the multiplicity is used to compute $g(y) = M_\gamma f*(y)$. The response function $h(x, y)$ is a differential form of g in the photon to nucleus energy $x = \epsilon/E$, *i.e.* $g = \int h(x, y)dx$. In practice $h(x, y)$ is discretized in values x and the range needs to be limited. The implementation here uses four discrete values of x equally spaced in logarithmic scale from $x_{\max} = \epsilon_m/(Am_p) \approx 10^{-3}/A$ down to $10^{-4}x_{\max} \approx 10^{-7}/A$. The nuclear species modeled include all nuclides represented in Figure 3.3.

Nuclear photons models with other methods

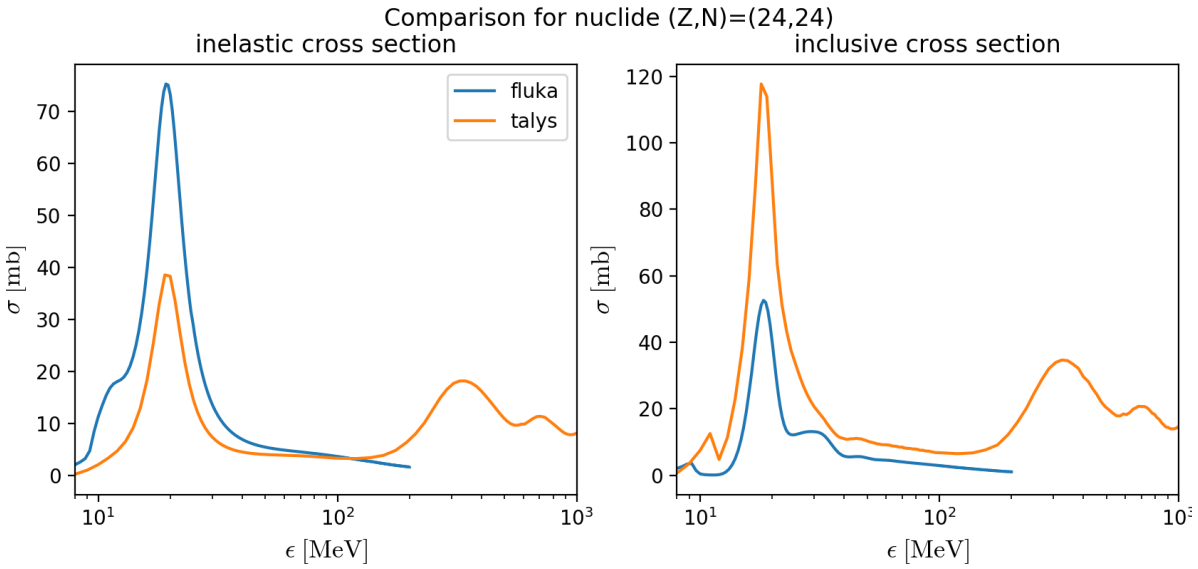

Figure 5.4: Comparison of photon models created using Talys and Fluka . The multiplicity is given by the ratio of the inclusive to inelastic cross section. The models codes differ considerably in the production rates and multiplicities. Comparisons for other species are included in Appendix B.

The detailed products of photonuclear interactions can be obtained by running dedicated codes such as Talys and Fluka . These codes take kinematic variables as input (product type, energy, spin, etc.) and model the reaction based on nuclear models, taking into account interaction probability, compound system formation, and the time evolution of the system. Therefore, the codes should provide a more accurate description. However, the codes do not agree in several cases as can be seen in Figure 5.4 (see Appendix B). Talys has some limitations: nuclei with $A < 7$ are not available and it does not cover energies in the photomeson regime. Fluka also covers a wider range of masses and energies in the photomeson regime, but only provides averages of the number and energy of produced photons while Talys returns a distribution. A systematic study quantifying these differences for all energies and nuclear species is necessary to estimate the impact in astrophysics, and will be part of future work. Tables for disintegration photons extracted from Fluka and Talys were created here for NeuCosmA , and implementation in PriNCe and CRPropa 3 is possible. In CRPropa 3 , the nuclear photons have been implemented (Heiter et al., 2018) extracting values from Talys , however it includes only photons produced from disintegrations in the photomeson regime, while the model presented in the previous section includes photons from disintegration in the photomeson regime (see Chapter 4).

It should be noted that the models discussed here exclude photons from isomeric states which may be of importance. An isomeric state is an excited state of a nuclear species which has a relatively long lifetime before it decays into the ground state with the emission of photons. The assumption that disintegration photons (from excited products) are emitted immediately after

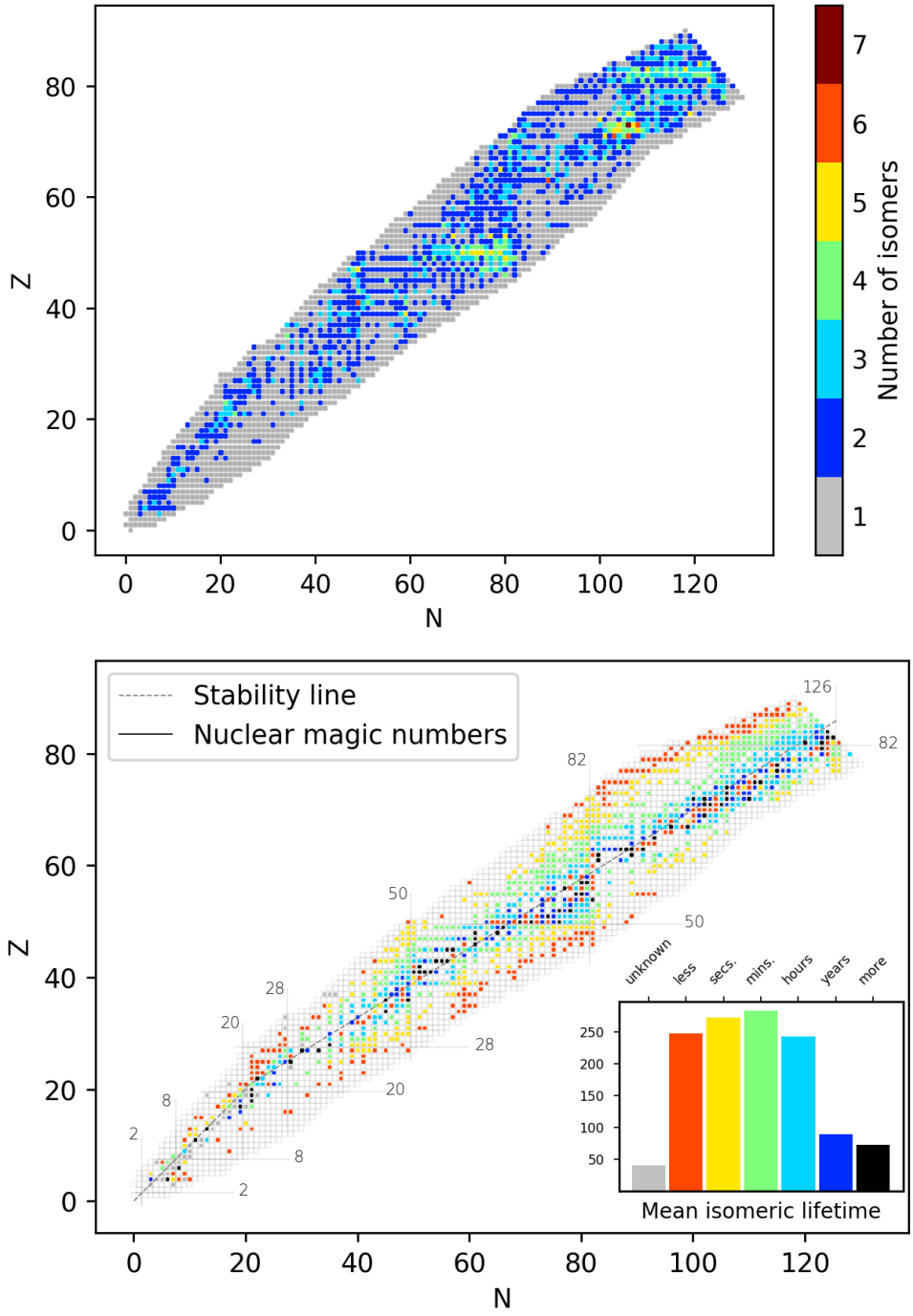

Figure 5.5: Data related to the isomeric states compiled in this work. Above, the number of isomeric states per nuclear species. Nuclei with one isomeric state do not have isomers with excitation energy, only ground states. On the bottom, the mean lifetime of the isomeric states. A considerable number of isomers have lifetimes comparable to the dynamic timescales of certain UHECR sources. Source of the data, (ENSDF, 2019).

interactions does not hold for isomeric states, which can have lifetimes in the SRF comparable to the dynamic timescales of some sources. Figure 3.3 illustrates the data from the ENSDF files (ENSDF, 2019) where the number of isomers and their distribution over all nuclear species are represented. Most nuclei with more than one isomeric state are located above iron masses, but there is a large amount also at lower masses. More importantly, the average lifetimes shown in the bottom figure illustrate there are plenty of nuclides with lifetimes above of seconds and above. This is relevant for UHECR sources such as GRBs, where such nuclei could be accelerated before decaying and even escaping the source, emitting the photons during propagation. If we consider nuclides with a lifetime of seconds in their own rest frame, for Lorentz boosts in the range of UHECRs $10^9 - 10^{11}$ their propagation before decay could range from 10 pc to 1 Mpc. This data is available for studies in-source and propagation, but the implementation is deferred to future works because the structure of the codes is not compatible currently with these species (*e.g.* the particle identification number format limits the maximum nuclear mass of nuclear species).

5.3 Implementation of the nuclear model to astrophysical simulations

Coupled AM^3 /NeuCosmA code

AM^3 (*Astrophysical Multi-Messenger Modeling* Gao et al., 2017) is a dedicated radiation modeling code that has been applied to blazar AGNs (Gao et al., 2017, 2019, Rodrigues et al., 2019), which models the non-linear couplings between different particle species self-consistently.

Like NeuCosmA (*cf.* Section 4.1), AM^3 can simulate the photointeractions undergone by electrons, protons and neutrons in an astrophysical source. The main differences are that *(a)* the code solves a version of Eq. 3.15 where photons are represented as an additional species in the coupled system of partial (integro-)differential equations, *(b)* electrons and positrons are also included in the system, and the photons emitted from their electromagnetic interactions feed self-consistently into the PDE system; and *(c)* AM^3 cannot treat photonuclear interactions of isotopes heavier than protons.

In an on-going project (Rodrigues et al., in development), the AM^3 and NeuCosmA codes have been coupled into a new simulation tool. With this new software, written in Python, it is possible to model self-consistently the photon production from photo-hadronic and electromagnetic emission from electrons, nuclei and nucleons co-accelerated in a blazar AGN (applications to other sources are work in progress).

A simulation with this new code is performed by iteratively running NeuCosmA and AM^3 , assuming that in each iteration the PDE system converges to a steady state, *i.e.* the stage

when the densities N_i become constant due to the balance between the sink and source terms contributing to the density evolution. To potentially achieve this state, the simulation must typically be run up to a few times the dynamical time scale of the system, when the effects of all the leading terms have been fully captured.

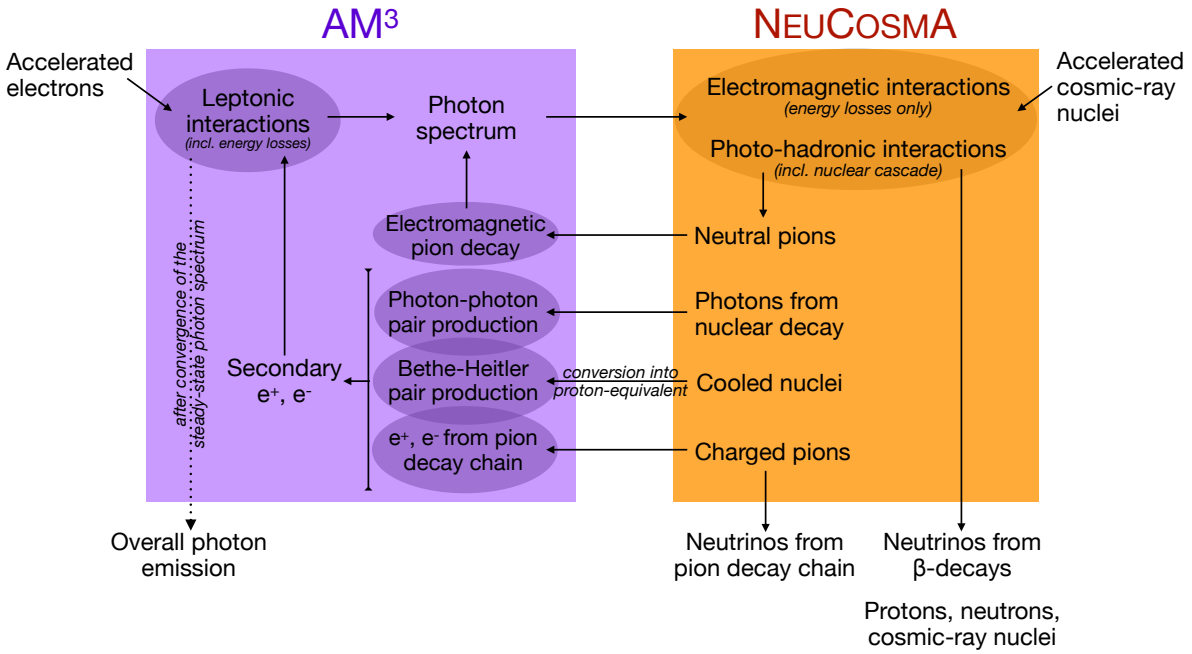

Figure 5.6: Schematic diagram representing an approximated flow of a new multimessenger simulation code (Rodrigues et al., in development), based on the coupling of the softwares AM^3 (Gao et al., 2017) and NeuCosmA (Baerwald et al., 2013), see also Section 4.1. In this iterative setup, AM^3 is responsible for calculating the radiation from electromagnetic processes, including electron cooling, while NeuCosmA calculates the photo-pion production and photodisintegration processes undergone by cosmic rays. This includes the development of nuclear cascades, as well as neutrino production. Cosmic-ray energy losses from electromagnetic cooling processes like Bethe-Heitler pair production and synchrotron cooling are also considered in NeuCosmA . The overall emission from the source is assumed to be dominated by accelerated electrons, with hadronic processes contributing as a perturbation to the purely leptonic model.

The flow of the software is represented in Figure 5.6. A first run is performed with AM^3 by injecting only electrons in the system (simulating their acceleration to a non-thermal spectrum), leading to a purely leptonic model. The photons produced by this leptonic simulation are then used as a static target photon field in NeuCosmA , assuming the same source parameters, such as the volume of the interacting region and the magnetic field strength (the reader is referred

to Section 5.4 where the example of a simulation of an AGN jet is discussed). In this second run, nuclei are included in the simulation, assumed to be co-accelerated with the electrons, and an estimate is made on the pions emitted through photomeson production, and the photons emitted by unstable isotopes from photodisintegration. In the second AM^3 run, the same accelerated electron spectrum is considered, and additionally the nuclei obtained from NeuCosmA are also injected in order to calculate the spectrum of electron/positron pairs emitted by the nuclei through Bethe-Heitler production. Note that although AM^3 cannot simulate nuclei, Bethe-Heitler pair production is a purely electromagnetic interaction, and can be treated by converting the nuclei into their proton-equivalent. This implies a re-scaling in energy of the spectrum of each isotope to account for the scaling of the pair-production rate with Z^2 (Eq. 3.14). Additionally, the photons emitted by unstable isotopes are also injected as an additional photon field contribution, as well as the pions resulting from photomeson production of nuclei. AM^3 then calculates the effects of these contributions: the Bethe-Heitler interaction will produce electron/positron pairs; the photons from nuclear decay can produce electron-positron pairs through photon-photon annihilation, and the pions will emit electrons or positrons from their decay chain. These electrons and positrons will radiate and create an additional contribution to the overall emission, thus changing the purely leptonic model.

Note that in order for this iterative method to converge, the contributions from nuclei described above must be a small perturbation to the overall emission, which is assumed to be largely dominated by electrons, namely electron synchrotron and inverse Compton (see Section 3.1.2).

My contribution to this new code was the inclusion of photon production from de-excitation and decay of photodisintegration products in the NeuCosmA software, as detailed in Section 5.2.

5.4 Application to the high-energy emission from Cen A

5.4.1 Multi-wavelength emission from Cen A

Centaurus A (abbreviated as Cen A), also known as NGC 5128, is an elliptical galaxy in the Centaurus constellation, located in the southern sky (for a review see *e.g.* Israel, 1998). At a distance of 3.4 Mpc, it is the nearest active galaxy. From its active galactic nucleus (AGN, see Section 2.2.2), a radio and X-ray di-jet extends up to 5 kpc, where it broadens into radio lobes that extend up to 250 kpc. In this section, I will focus on the multi-wavelength emission from the core of the Cen A jet, which is the more central region extending up to ~ 1 pc from the central black hole.

Like the radio lobes of Cen A (Abdo et al., 2010b), the core region has been detected in gamma rays above 100 MeV by the *Fermi*-LAT satellite (Abdo et al., 2010a). More recently,

the H. E. S. S. ground-based gamma-ray telescope system detected gamma-ray emission from the core with energies above 100 GeV (Aharonian et al., 2009).

The core emission from Cen A has been successfully explained in the range from radio up to GeV gamma rays as a product of synchrotron self-Compton scattering by an electron population (*e.g.* Chiaberge et al., 2001, Abdo et al., 2010a, Kundu and Gupta, 2014). As explained briefly in Section 3.1.2, this is the emission of synchrotron radiation by electrons in a magnetic field, and the simultaneous up-scattering of that synchrotron radiation by the same electron population.

In Figure 5.7 we can see the multi-wavelength data from the core of Cen A, from radio to the recent observation in very-high-energy (VHE) gamma rays. As is the case with AGNs in general, the emission is primarily characterized by two broad band features. The low-frequency broad band can be explained by synchrotron emission from a population of accelerated electrons. The broad band peaking at hundreds of MeV is explained in the literature as the result of the Compton scattering of the low-frequency synchrotron photons by the same electron population (*e.g.* Chiaberge et al., 2001, Abdo et al., 2010a, Kundu and Gupta, 2014). As explained briefly in Section 3.1.2, this is known as a synchrotron self-Compton (SSC) model.

In a typical one-zone model, the region where the non-thermal interactions take place is considered spherical, with a radius R' which in this case is constrained to 1 pc, because we are modeling localized emission from the core. We will follow the usual astrophysical convention to denote quantities in the rest frame of the source with primed variables, whereas unprimed variables refer to quantities in the observer‘s frame at Earth. As discussed in Section 2.2.2, the Lorentz factor of an AGN jet is usually of the order of $G = 10$. However, in the case of Cen A, the jet is seen at a wide angle, leading to a Doppler factor $\delta_D \sim 1$ [1]. This implies that relativistic effects, such as Lorentz contraction ($R = R'/\delta_D = R'$), photon blueshift or luminosity boost are not relevant here.

In an SSC scenario, the same electron population is responsible for the synchrotron photons and for the inverse Compton scattering of those photons, which means that equations Eq. 3.11 and Eq. 3.12 are coupled. By Eq. 3.12, the energy of the synchrotron emission depends on the energy of the emitting electrons, E_e, and on the strength of the magnetic field, B. At the same time, the photon density n_γ in Eq. 3.12 depends on the luminosity of the accelerated electrons, L_e, their characteristic energy E_e, and on the volume of the region where the interactions take place, $V \sim R'^3$ (assuming a spherical zone with radius R). Thus, in an SSC model, the peak frequencies of the two broad bands and their relative heights can help constrain relationships between the basic parameters that influence the emission. Additionally, the slopes of the broad bands can give further information about the detailed shape of the accelerated electron spectrum.

[1] The actual value varies slightly among the different SSC models in the literature, but in the one presented here $\delta_D = 1$ is assumed.

The two solid curves in Figure 5.7 represent the results of two SSC models (Abdo et al., 2010a, Kundu and Gupta, 2014). In both cases the emission region has a radius of $R \sim 1$ Mpc. Other parameters of these two models can be found in the respective references. As we can see, SSC interactions can only account for the emission up to ~ 1 GeV, while the fluxes observed at higher frequencies require other explanations.

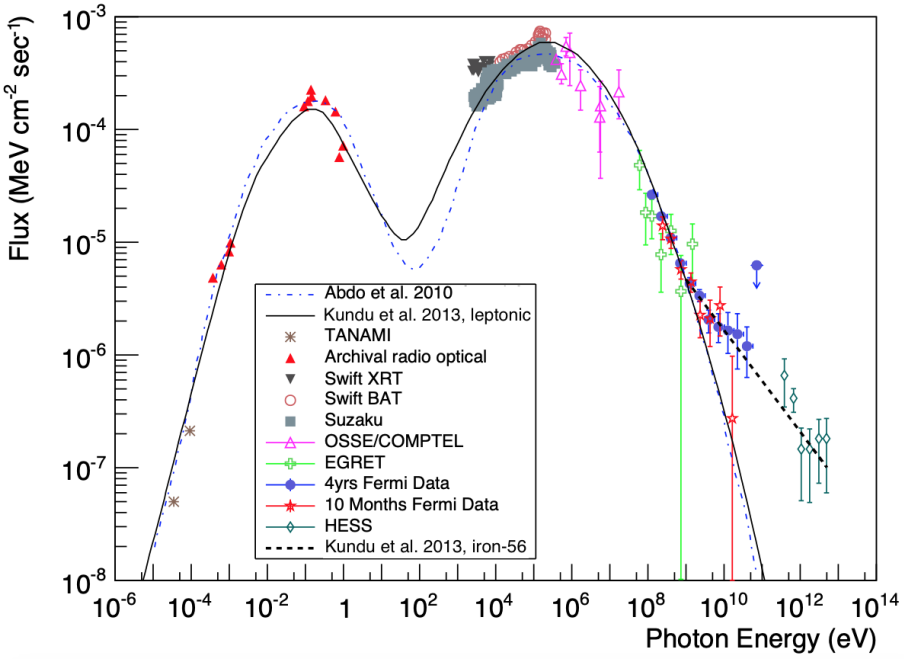

Figure 5.7: Multi-wavelength observations of the core of Cen A, with several model predictions shown as overlayed curves. The sets of multi-wavelength data points, from radio up to VHE gamma rays, are identified in the caption by the name of the respective experiment. Figure taken from Kundu and Gupta (2014).

Abdo et al. (2010a) have shown that SSC scattering from an independent population of electrons interacting in a second independent blob with three times larger radius can explain the emission up to very high energies. Brown et al. (2017), on the other hand, hypothesize that the emission can originate in a localized distribution of dark matter particles surrounding the galaxy core, or in a population of millisecond pulsars. Using a more conventional one-zone lepto-hadronic model, Petropoulou et al. (2014) have demonstrated that ultra-high-energy protons co-accelerated with the electrons can also explain the H.E.S.S. fluxes. In that scenario, the dominating emission process is synchrotron radiation from electron-position pairs created through Bethe-Heitler interactions of the ultra-high-energy protons.

In order to apply the nuclear model presented in this chapter, we will focus on the hypothesis

that ^{56}Fe nuclei are accelerated to ultra-high energies in the core of the Cen A jet. These iron nuclei then interact with the photons emitted by the electrons, undergoing photodisintegration. This can lead to the emission of secondary photons through the decay of unstable products. Kundu and Gupta (2014) claim that this process leads to a power-law flux of gamma-rays up to VHEs, represented in Figure 5.7 as a dashed line, and can therefore explain both *Fermi* and H.E.S.S. observations. In the remainder of this chapter, this hypothesis will be tested by means of numerical modeling, challenging the conclusion previously drawn by Kundu and Gupta (2014).

5.4.2 Comparison of the method to the state-of-the-art literature

Kundu and Gupta (2014) have modeled the emission from cosmic-ray iron nuclei accelerated in Cen A. The target photon spectrum in the source is obtained from converting the flux shown as a solid line in Figure 5.7 to an energy density in the source rest frame:

$$\frac{dN_\gamma(\epsilon'_\gamma)}{d\epsilon'_\gamma} \approx 4\pi D^2 \frac{\delta_D^{-4}}{c\,R'^2} \frac{dF_\gamma(\epsilon_\gamma)}{d\epsilon_\gamma dt dA}, \tag{5.8}$$

where D is the distance to the source (3.4 Mpc), $\delta_D = 0.25$ is the assumed Doppler factor of the jet, R' is the size of the emission region, and $dF_\gamma(\epsilon_\gamma)/d\epsilon_\gamma dt dA$ is the observed flux spectrum shown in Figure 5.7. This observed photon spectrum is obtained as the result of an SSC model, as discussed previously.

Once the target photon spectrum is calculated, the photodisintegration rate is obtained by Kundu and Gupta (2014) through a series of steps, which can be summarized as follows:

(a) The photodisintegration cross section has been approximated by a delta function, given by

$$\sigma(\epsilon'_\gamma) = \pi\sigma_0 \frac{\Delta}{2} \delta(\epsilon'_\gamma - \epsilon_0), \tag{5.9}$$

where $\sigma_0 = 1.45A$ mb, $\epsilon_0 = 42.65A^{-0.21}$ MeV is the assumed central value of the GDR, $\Delta = 8$ MeV is the assumed width of the GDR, and $A = 56$ for the isotope considered which is ^{56}Fe.

This approximation is represented by the dashed line in Figure 5.8, compared to the Lorentzian form used in this work (orange curve).

(b) The photodisintegration rate obtained from that cross section has been used to obtain an average value, given by $\Gamma^{\rm disinteg} = 2 \times 10^{-8}$ s^{-1}.

(c) The photons emitted by secondaries of photodisintegration have a fixed energy in the cosmic-ray frame.

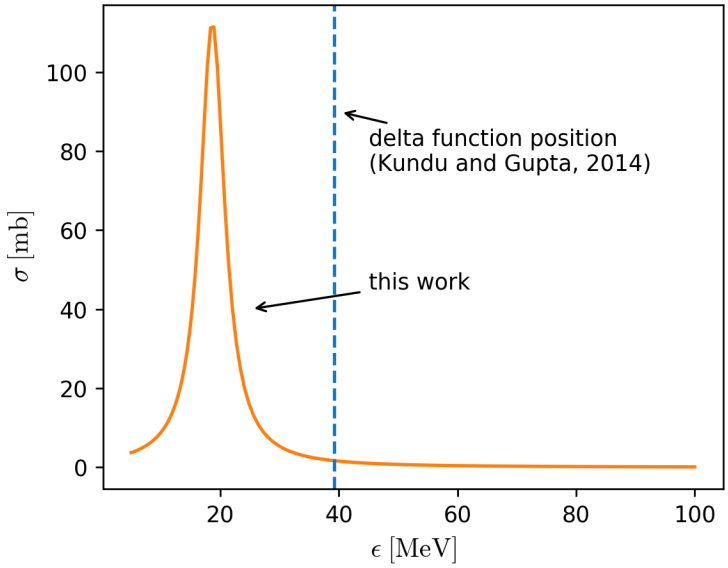

Figure 5.8: Comparison between cross sections in the model presented in this chapter (solid curve) and the approximation used by Kundu and Gupta (2014), who consider a Delta distribution.

(d) Photons from the photodisintegration of lighter secondary nuclei (which are created from successive disintegrations) are neglected compared to those from iron photodisintegration.

(e) All photons emitted through nuclear processes are allowed to escape the source.

(f) Iron nuclei do not interact through other processes.

These steps lead to the result that photons from photodisintegration of iron are emitted with power-law spectrum that can explain the H.E.S.S. fluxes, as shown in Figure 5.7 as a dashed line. This power-law follows directly the assumed acceleration spectrum of $^{56}\mathrm{Fe}$, which has a spectral index of approximately 3.

As detailed previously in this chapter, in the new model the assumptions used are more realistic at several levels, namely *(a)* the cross section is approximated with a Lorentzian curve as a function of energy; *(b)* the photodisintegration rate is computed as a function of the cosmic-ray energy, which means that nuclei with different energies will give different relative contributions to the overall photon spectrum; *(c)* the photons emitted by nuclei are redistributed in x (as explained previously); *(d)* all the secondary isotopes created in the nuclear cascade are considered *(e)* and the photons produced can re-interact in the source, namely by producing pairs through annihilation with softer photons (see Figure 5.6); and *(f)* iron nuclei, as well as the secondary hadrons, are self-consistently cooled through photo-hadronic and electromagnetic processes, and can emit electron/positron pairs through Bethe-Heitler interactions. These pairs will create an

additional contribution to the photon flux emitted by the source, mainly through synchrotron emission.

5.4.3 Results

In Figure 5.9 we can see the result of a numerical simulation using the AM^3 /NeuCosmA code described above, where the new nuclear photon model was included. The main result is shown as a solid magenta curve, representing the full multi-wavelength emission from the Cen A core. The assumption of the model is that electrons and ^{56}Fe are co-accelerated in a single spherical zone. As described in Section 3.2, this numerical treatment accounts for all relevant electromagnetic and hadronic processes undergone by these accelerated particles.

The dashed magenta curve shows the photon fluxes emitted by the accelerated electrons alone. Like the solid curves shown in Figure 5.7, this corresponds to a purely leptonic SSC model. Besides the low-energy synchrotron bump and the SSC bump in the keV-MeV range, there is also a third bump at 100 MeV, which originates in the Compton scattering of the SSC peak. This second-order feature is not present in the results by (Abdo et al., 2010a, Kundu and Gupta, 2014), but it has been captured by Petropoulou et al. (2014).

As explained previously, by fitting the result of the SSC model to the observed fluxes below GeV, the main source properties were constrained, namely the size of the region R [2], the magnetic field strength B, and the Doppler factor of the jet δ_D as well as the shape and normalization of the electron spectrum produced by the acceleration process. This allows fixing the leptonic contributions to the SED in a first stage before finding the parameters of the hadronic injection that produce the VHE photons. For simplicity, the spectrum of accelerated electrons is assumed to be a simple power law with an exponential cutoff (*cf.* Section 2.2.2):

$$\frac{dN_e^{\rm inj}}{d\gamma_e} \sim \gamma_e^{-\alpha} \exp\left(\frac{\gamma_e}{\gamma_e^{\rm max}}\right), \text{ for } \gamma_e > \gamma_e^{\rm min}, \tag{5.10}$$

where $\gamma_{\rm e}^{\rm min}$ and $\gamma_{\rm e}^{\rm max}$ are the minimum and maximum Lorentz factors of the non-thermal electrons, and α is their spectral index. The normalization of the spectrum is given by the total

[2] Besides being used to calculate the volume of the interaction region, and therefore the particle energy densities (see Eq. 5.10), the parameter R plays a role in the escape of photons and particles from the source. The differential equations that describe the evolution of the density spectra have an 'escape' term that subtracts the amount of particles present in the system at every step of the integration, and the escape rate is inversely proportional to the light-crossing time of the region: $t_{\rm esc}^{-1} \sim c/R$. This assumption corresponds to an 'advective' escape scenario, also used as an assumption in previous studies of cosmic-ray interactions in AGNs and other sources (see *e.g.* Lacki and Thompson, 2010, Senno et al., 2015, Rodrigues et al., 2018). In this thesis, the focus is placed on aspects of the modeling more directly related to nuclear interactions, rather than the technical details of the astrophysical simulations.

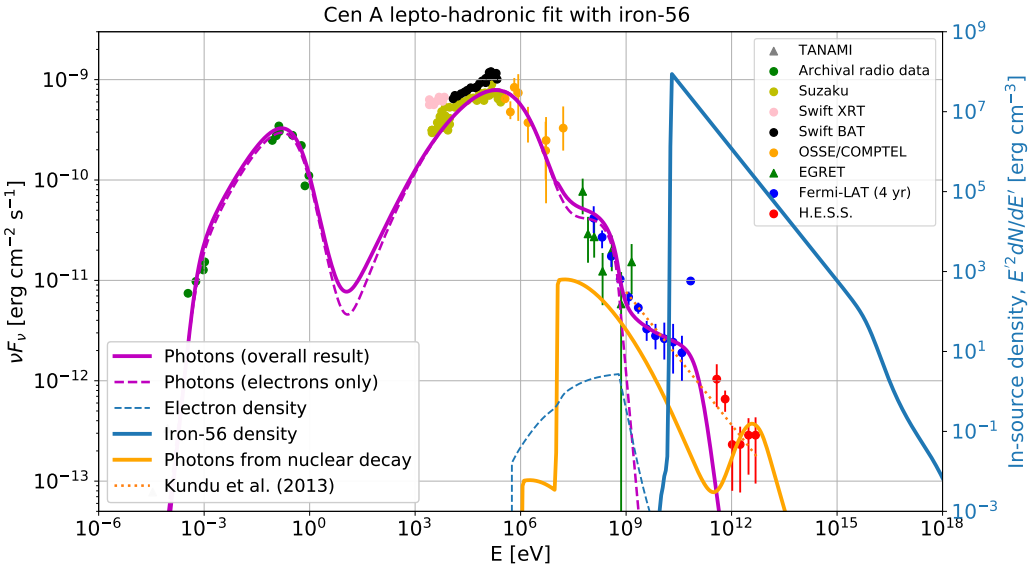

Figure 5.9: Main result of the lepto-hadronic simulation of the Cen A core emission, obtained with the novel AM^3 /NeuCosmA code (see Section 3.2.1). This code includes the treatment of photon emission from nuclear de-excitation and decay presented in this chapter, which leads to the fluxes shown as an orange curve. The final result (solid magenta curve) also takes into account other electromagnetic processes, such as photon-photon annihilation, which leads to the re-distribution of these photons to lower energies. Figure to be included in Rodrigues et al. (in development).

power deposited in non-thermal electrons, $L_e^{\rm inj}$:

$$m_e \int \frac{dN_e^{\rm inj}}{d\gamma_e} \sim \gamma_e d\gamma_e \; = \; \frac{L_e^{\rm inj}}{4\pi\, R^2\, c}. \tag{5.11}$$

The values of the parameters in the final result are listed in Tab. 5.1. The fact that these values differ from other SSC models in the literature is a consequence of the different characteristics of the models. For example, the AM^3 /NeuCosmA code performs a time-dependent calculation of the energy losses suffered by the electrons, which leads to a gradual change in the electron spectrum, usually with a softening at high energies. The system is assumed to eventually converge to a steady state between the acceleration and cooling processes, after which point the electron and radiation density spectra become constant. On the contrary, works like Kundu and Gupta (2014) do not explicitly consider the cooling effects on the electron spectrum, which is the main reason for the differences between the parameter values obtained in both works.

The electron density spectrum in the source at the end of the simulation (after having suffered

Parameter	Value	
Source Doppler factor, δ_D	1.0	
Emission zone radius, R / cm	9.5×10^{14}	
Magnetic field strength, B / G	10.0 G	
	Electrons	^{56}Fe
Minimum Lorentz factor, $\gamma^{\rm min}$	1.3×10^3	1.8×10^1
Maximum Lorentz factor, $\gamma^{\rm max}$	7.0×10^5	3.6×10^{11}
Spectral index, α	3.3	3.1
Injection luminosity, $L^{\rm inj}$ / erg s^{-1}	1.0×10^{43}	1.3×10^{48}

Table 5.1: Parameters of the lepto-hadronic model of Cen A using the nuclear interaction model presented in this chapter (Rodrigues et al., in development). The resulting multi-wavelength emission is shown as a magenta curve in Figure 5.9. Table to be included in Rodrigues et al. (in development).

energy losses from the radiative processes) is shown in Figure 5.9 as a dashed blue curve. Note that the energy density scale is given in the right hand side axis and is different from the scale of the observed flux at Earth, given in the left hand side axis. The transformation between the two is given by Eq. 5.8.

Additionally to the electrons, we assume that nuclei of ^{56}Fe are also accelerated in the source. The shape of the accelerated iron spectrum was obtained by scanning the parameter space with the model, searching for the best fit to the high and very-high-energy data. Like the electrons, the iron nuclei are assumed to be accelerated to a simple power-law spectrum, described by a minimum and maximum Lorentz factors, total luminosity (which determines the normalization of the spectrum) and a spectral index. With the remaining source parameters already constrained by the leptonic model, only these four parameters were left to vary in order to best explain the emission above GeV energies. The best values are shown in Tab. 5.1. The iron density spectrum in the source in the final steady state (after undergoing energy losses as discussed in detail below) is shown as a solid blue curve.

The leptonic and hadronic luminosities are in a ratio of 10^5 which is possibly very high. However, the luminosities of iron are dominated by the minimal injection energy, which was chosen particularly low here to explore their contributions via Bethe-Heitler processes. However we have found these contributions to be negligible, and thus there are no indications that the injection of lower energy nuclei is as large as assumed. Furthermore, the minimal injection energy can be increased (thus reducing the total luminosity) with no effect on the photoproduction results. This is because the photoproduction threshold is much higher, at around PeV energies (see Figure 5.10). Hence, choosing a higher value of the minimal injection energy, *e.g.* 1000 times

larger, would still be below the photoproduction threshold while reducing the iron luminosity to ten times lower than that of electrons. Therefore the needed iron luminosity can be reduced considerably without changing the photoproduction results discussed here.

The acceleration of iron nuclei up to ultra-high energies leads to a series of processes that change the multi-wavelength emission obtained with the leptonic SSC model:

- Iron nuclei are assumed to be co-accelerated with electrons, and are therefore injected in the system with a power-law spectrum like in Eq. 5.10, but with parameter values independent from the electrons;
- The high-energy iron nuclei encounter the leptonic radiation and photodisintegrate, leading to the production of a cascade of lighter secondary isotopes;
- Besides interacting with the leptonic radiation through photodisintegration, these isotopes also undergo Bethe-Heitler pair production, which leads to energy losses of the nuclei and to the emission of high-energy electron-position pairs;
- The electrons and positrons created through Bethe-Heitler pair production interact with the magnetic field and emit additional high-energy synchrotron radiation;
- The creation of excited or unstable secondary isotopes leads to gamma-ray emission from their decay (which was also considered by Kundu and Gupta (2014) with different assumptions);
- High-energy photons produced by Bethe-Heitler pairs and by unstable/excited isotopes interact with softer photons of leptonic origin and annihilate, producing further electron-positron pairs, creating a synchrotron-supported electromagnetic cascade.

In principle, the additional process of photomeson production can be experienced by the accelerated nuclei. As discussed earlier in this thesis, this can lead to the additional radiation emission through the production of *(a)* neutral pions that decay into photon pairs, and *(b)* charged pions, which decay into muons and then electrons, which then feed into the cascade. However, in this source photomeson production of nuclei is sub-dominant compared to photodisintegration and therefore it will not be included in this discussion.

The photons emitted by unstable and excited secondary nuclei are represented in Figure 5.9 as a solid orange curve. As we can see, the shape of this spectrum is different from the power law estimated by Kundu and Gupta (2014), represented as a dotted orange line. To understand this difference, we start by analyzing Figure 5.10. The dotted blue curve shows the photodisintegration rate of ^{56}Fe as a function of the energy of the nucleus, as calculated in NeuCosmA (a part

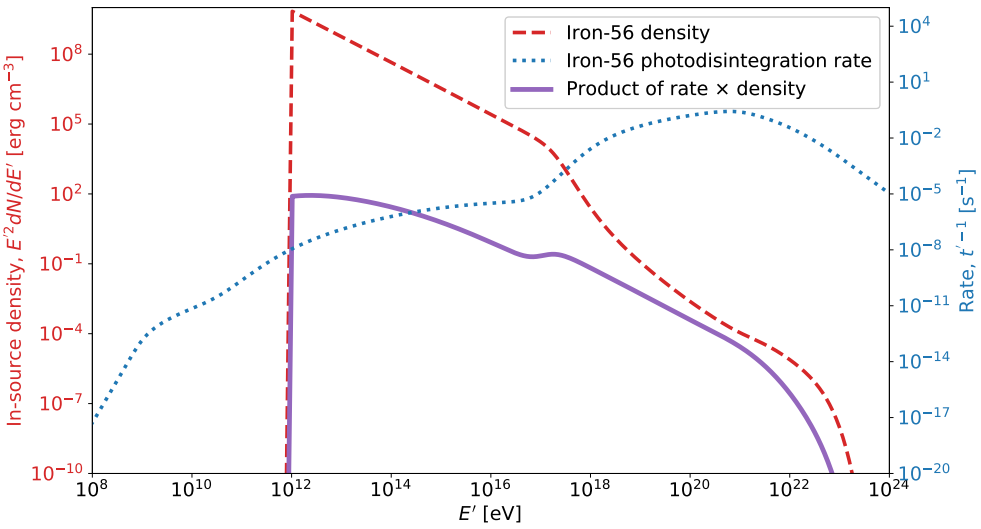

Figure 5.10: Rate of photodisintegration of ^{56}Fe (blue dotted), spectral density of ^{56}Fe in the final stage of the simulation (red dashed) and product of the two quantities (purple). The feature in the purple curve at 10^{17} eV is responsible for the peak in the orange curve in Figure 5.9, which is shifted to lower frequency due to the energy redistribution of the emitted photons. Figure to be included in Rodrigues et al. (in development).

of the AM^3 /NeuCosmA software). The red dashed curve shows the energy density spectrum of ^{56}Fe, the same as in Figure 5.9. Finally, the product of the two is shown as a solid purple curve, which exhibits a bump at around 300 PeV, due to the increase in the photodisintegration rate. In the nuclear model proposed in this chapter, this convolution of rate and spectrum is taken into account, leading to the feature that can be observed at 10 TeV in the orange curve in Figure 5.9 (the energy shift of this feature in the photons spectrum comes from the energy distribution of the photons in the nucleus rest frame, as will become apparent in the discussion below). In comparison, as detailed in Section 5.4.2, the model by Kundu and Gupta (2014) considers only an average, energy-independent photodisintegration rate, which cannot capture these details in the spectral shape of the emitted photons (dotted orange curve).

Another two aspects that are captured by this new model are the re-distribution in energy of the emitted photons, and the individual contributions from all the secondary nuclei, and not only from ^{56}Fe. These two features can be explained by analyzing Figure 5.11, which shows the density spectra of four selected isotopes (dashed curves) and the photons (solid curves) resulting from photodisintegration of each individual species. For reference, the red dashed curve corresponds to the blue curve in Figure 5.9, and the thin black curve corresponds to the

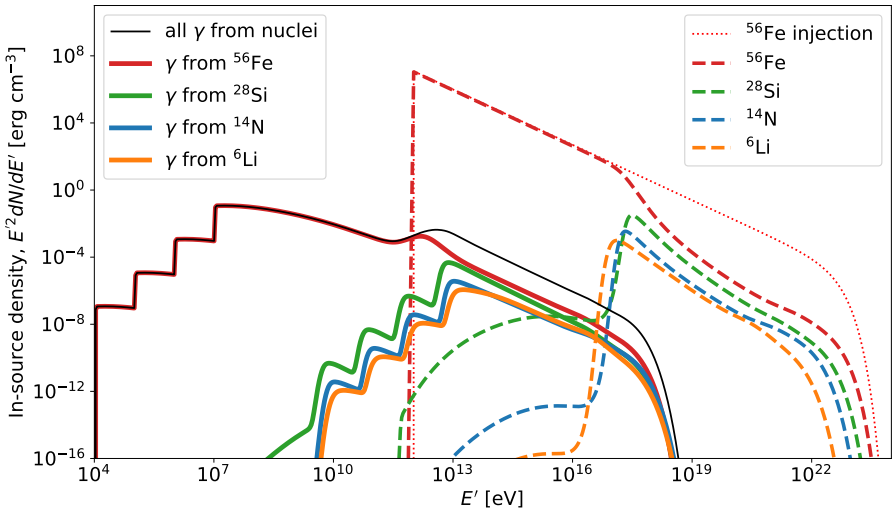

Figure 5.11: Energy density spectra in the source of nuclei (dashed curves) and the respective emitted photons (solid curves) from unstable secondaries created by photodisintegration in the source. Below 1 TeV, the total photon flux (black curve) is dominated by ^{56}Fe photodisintegration, while above 1 TeV other lighter secondary isotopes also contribute, a feature that is not included in the current literature. Figure to be included in Rodrigues et al. (in development).

total photon spectrum from nuclei, which is the orange curve in Figure 5.9. Additionally, we can see the injection spectrum of ^{56}Fe as a dotted red curve, representing the accelerated iron spectrum before energy losses.

The injection and final spectrum of ^{56}Fe are the same below 10^{17} eV, or 100 PeV, while above this energy ^{56}Fe suffers efficient energy losses from photodisintegration, and the final iron spectrum becomes lower and softer than the injected one. Above this energy, the production of secondary isotopes becomes efficient and their densities spike (see dashed curves of silicon-28, nitrogen-14 and lithium-6). This impacts the emission of photons from nuclear decay. We can see that at energies below ~ 1 TeV, these photons are dominated by ^{56}Fe, while at higher energies other lighter isotopes also contribute significantly.

The four spikes that can be seen in the low-energy part of the photon spectra are due to the discretization of the x values of the photons, discussed in Section 5.2. In the current version of the model, these distributions are centered around four characteristic values for each isotope. So for ^{56}Fe, for example, the spikes in the photon density are produced by interactions of nuclei with the minimum energy (1 TeV), below which there is a sudden drop in density. Each of

the four spikes corresponds to photons produced with one of the four quantized characteristic x values. The same happens to the secondary nuclei in the figure, which all have a 'peaky' density spectrum: for each isotope, the spikes in the photon spectrum are produced by nuclei sitting at the maximum of the spectrum.

In order to refine this distribution, the number of discretized x-values can be increased by adding more data to the photon production tables. This aspect will be addressed in future installments of the model. However, in the case of Cen A it is clear that this discretization does not affect the result, since below $\sim$ 1 TeV, where the spectrum from secondary nuclei shows these artifact peaks, ^{56}Fe dominates the emission, and below $\sim$ 10 MeV, where the spectrum from ^{56}Fe also shows these artifacts, the emission is dominated by electron SSC (*cf.* Figure 5.9). Finally, note that as shown previously in Figure 5.10, the bump observed in the final overall spectrum is a physical result from considering energy-dependent interaction rates, and not a consequence of these numerical artifacts.

Note that while these four isotopes are used as illustrative examples, in reality the code explicitly accounts for all the isotopes produced in the interactions whose lifetime in the source rest frame exceeds a certain threshold (for a more complete discussion, see Section 3.1.1). In the case of this system, a total of 232 isotopes are explicitly accounted for in the simulation.

The final aspect of this study that is also not addressed in other literature about ^{56}Fe emission from Cen A, is the creation of electromagnetic cascades from pair production, both by nuclei and by high-energy photons. As we can see in Figure 5.9, the photons emitted through nuclear decay (orange curve) are strongly attenuated at the highest energies in the final result. This is due to photon annihilation with softer photons in the source. At threshold, a 10 TeV photon from nuclear interactions will efficiently pair-annihilate with a 0.1 eV infrared photon (*cf.* Section 2.2.2), which in this source is available from synchrotron emission of accelerated electrons. These interactions lead to the softening of the spectrum at VHEs, and create electron-positron pairs that radiate at lower frequencies through synchrotron emission. This is responsible for the disappearance of the peak above TeV.

Although the TeV emission from nuclei is re-processed in the source, and therefore cannot explain H.E.S.S. observations, it plays nonetheless a crucial role in explaining *Fermi* data in this model. In Figure 5.12, we can see a close-up of the result at high energies. Overlayed as a dashed curve is the result of a similar simulation where photons from nuclear decays were excluded. Without this process, the model would be unable to explain *Fermi* data between 1 and 30 GeV. A crucial aspect to this fit is the soft acceleration spectrum of iron-56 ($\alpha = 3.1$).

Finally, the dashed curve in Figure 5.12 shows the result without accounting for Bethe-Heitler pair production by nuclei. We see that the synchrotron emission from these pairs provides the dominant contribution to the flux above $\sim$ 30 GeV, and is responsible for a significant hardening

of the spectrum above GeV. Bethe-Heitler pairs are also responsible for the factor-two increase in flux at 100 MeV compared to the purely leptonic model (Figure 5.9).

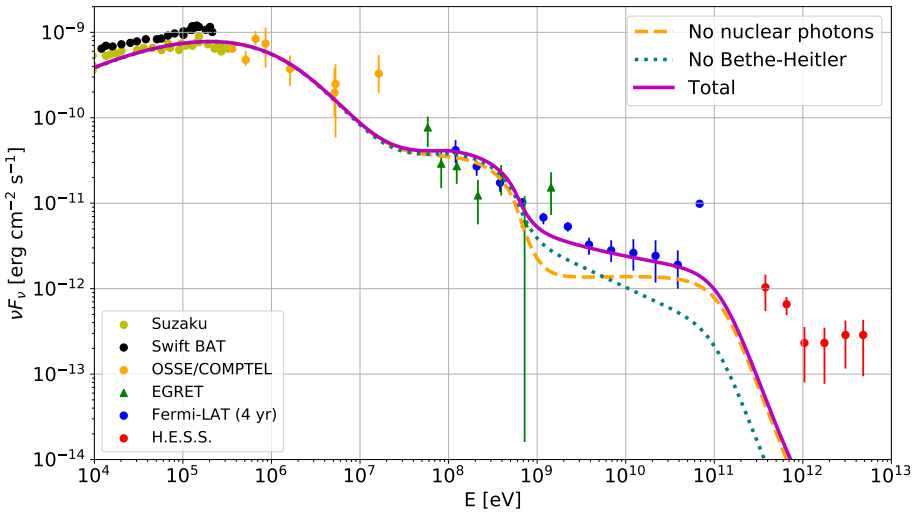

Figure 5.12: Close-up at high energies of the result of figure Figure 5.9 (magenta). Overlaid are the results of the same simulation but without accounting for photons from unstable nuclei (dashed), and without emission of electron-position pairs by the nuclei (dotted). The former process dominates the emission from 1-30 GeV, and the latter dominates above 30 GeV, and is responsible for an overall spectral hardening above GeV. Figure to be included in Rodrigues et al. (in development).

By taking into account nonlinear processes in the source, such as pair-induced electromagnetic cascades, with a fully numerical approach, and by treating photon emission from nuclear de-excitation and decay with input from nuclear interaction models, this study has shown that VHE photon emission from Cen A cannot easily be explained with the acceleration of ^{56}Fe in the source, as previously proposed by Kundu and Gupta (2014). This again illustrates the importance of data-driven models and nuclear physics insights in astrophysical studies of cosmic-ray interactions.

The recent publication H. E. S. S. Collaboration et al. (2020) improved the spatial resolution of the jet and found that the TeV emissions span an extended region than that considered here. The consequences of these findings in the context of this thesis were not investigated due to time constraints, and are left for following publications(Rodrigues et al., in development).

5.5 Conclusions and outlook

This chapter focused on the emission of photons as a result of the photodisintegration of nuclei. The physical picture was described and contrasted with the treatment in astrophysical simulations. I have presented a new model for simulating the disintegration photoproduction (DisPhot), whose methods and assumptions were elaborated. The number of parameters is reduced and the cross sections are based on analytical expressions derived from experimental values. The model was also implemented in the NeuCosmA software, and presented examples of computation results. Alternative photodisintegration models were also presented based on the Talys and Fluka codes, and the differences in the results were discussed (see also Appendix B).

I have also incorporated DisPhot into a coupled AM^3 / NeuCosmA code developed in parallel by my collaborators (Rodrigues et al., in development). This larger piece of software can be used to model self-consistently the photo-hadronic and electromagnetic processes undergone by electrons, nuclei and nucleons co-accelerated in a blazar AGN.

This astrophysical code was applied to the galaxy Centaurus A, in order to estimate the impact of DisPhot compared to the results of other works. The differences in the approach to treat the disintegration photoproduction were detailed. The improvements in DisPhot in contrast with the earlier work are: a more realistic cross section, a photoproduction spectrum with multiple values of the relative energy, an inclusion of all secondary nuclei and their disintegration photons. Additionally, the coupled code includes other competing interactions ignored in previous studies, such as Bethe-Heitler pair-production.

The improvements in the description of disintegration photoproduction by applying this more sophisticated model show that the mechanism proposed does not explain anymore all the high energy photons. The realistic interaction rates lead to features in the spectrum that were ignored previously: namely, the cascading interactions of the high-energy photons attenuate the high energy photons, failing to explain gamma-ray observations through this mechanism. Finally, it was shown that the contributions from Bethe-Heitler pair production dominate the photon fluxes at the highest energies, and therefore need to be considered in a complete treatment.

This study also shows that in order to self-consistently explain the VHE gamma-ray observations from Centaurus A, other assumptions may be necessary. For example, the escape of accelerated nuclei from the source can lead to photodisintegration with the cosmic photon backgrounds, which would not be so severely attenuated as inside the source itself. Other possibilities for photon production inside the jet should in principle involve different characteristics of the emission region, such as a lower optical thickness to photons in the VHE regime. This, however, has implications for the photon emission at other wavelengths, which must be included in the analysis. Such considerations are beyond the scope of this thesis and are therefore left for future

work on this topic.

Chapter 6

Superheavy UHECR in the context of intergalactic propagation

The observed increase of mass in the composition of UHECRs at the highest energies (Section 2.1.2) is compelling evidence that nuclei survive acceleration and transport through the intergalactic medium. This was a prediction since the first estimations were performed (Stecker, 1969), where it was found that iron nuclei of 100 GeV could survive for about 3 Gpc distance (10^{10} years). This estimate however did not account for the redshift dependence of the CMB photon density, which increases the interaction rates (*i.e.* reduces the survival distance).

There is a considerable amount of studies (Farrar and Piran, 2014, Alves Batista et al., 2019a, Muzio et al., 2019, Heinze et al., 2019, among others) that achieve a fit of the UHECR spectrum by assuming different compositions in the source. In all these studies, only the elements up to iron are considered. The central argument for not including heavier nuclei is that they are much less abundant, as evidenced by studies of solar system (SoS, Lodders, 2010) and extra-galactic (Kirby, 2011) composition. However, this evidence relies mostly on star compositions, while nucleosynthesis sites, like binary neutron star mergers, are characterized by larger fractions of heavier nuclides (see Chapter 2.2.2).

On the other hand, the methods for estimating the composition of UHECRs do leave room for the presence of heavier nuclei, since the mass estimates are the result of averaging multiple air shower events of comparable total energy. As discussed in Section 2.1.2, estimating the composition of UHECRs is achieved by comparing $\langle X_{\rm max}\rangle$ and $\sigma(X_{\rm max})$ with measured values. The values of $\langle X_{\rm max}\rangle$ can be reproduced by a single mass composition or by a mixed composition, but including also $\sigma(X_{\rm max})$ can help break this ambiguity (Abreu et al., 2013).

Additionally, the maximum mass that can be inferred from air showers is limited, since the hadronic interaction models required have not been explored for masses heavier than iron. It is therefore currently not clear how these models would extrapolate to higher masses. On the other hand, including larger masses allows to explore other possible scenarios, like that the observed UHECRs at the highest energies can be produced by interactions of even heavier nuclei during their propagation. As it will be discussed in this chapter, there are energy ranges where

nuclei heavier than iron actually have longer interaction lengths in the intergalactic medium. Furthermore, the energy loss of a cosmic ray nucleus of a given energy due to interactions with the cosmological radiation backgrounds is generally lower the higher its mass, because of the proportional decrease in the nucleus' Lorentz boost.

This chapter considers the possibility that nuclei heavier than iron are present in the UHECR spectrum observed. These nuclei will be hereon referred to as *superheavy*. The interactions of superheavy nuclei are discussed in the context of their extragalactic propagation. The propagation of superheavy nuclei is performed for the first time and is found in agreement with approximate relations derived from the interaction rates. These results represent the theoretical groundwork for a project on this topic, currently in preparation (Morejon et al., in development).

6.1 Methods: Preparing interaction tables for propagation codes

PriNCe (Heinze et al., 2019) is an efficient UHECR propagation code that solves the transport equations Eq. 3.15 using a vectorized approach to considerably reduce computation time. The code has been designed with extensibility and modularity in mind, allowing easy variation of model inputs such as interaction models and photon fields.

The propagation of superheavy nuclei was achieved by constructing interaction models and collecting experimental data to extend PriNCe simulation capabilities to superheavy nuclei. The mass range considered here includes all nuclei up to mass number $A = 208$ (*cf.* Figure 3.3). This means an addition of more than 2100 nuclides to the default number of nuclides in PriNCe , which originally only covered nuclei with masses up to $A = 208$ (*e.g.* iron-56).

The data for spontaneous decays was compiled into an input decay table as required by PriNCe . The source of the data are the Atomic Mass Evaluation (AME2016) files (Huang et al., 2017, Wang et al., 2017) and from the ENSDF files (ENSDF, 2019). The presentation of the main decay types for these nuclei appears in Chapter 3 (see Figure 3.1 and Figure 3.3).

Additionally, cross section tables were produced for photonuclear processes like photodisintegration and photomeson interactions. The photodisintegration cross sections were extracted by running the code Talys . Software tools were produced for parsing the output (interaction products of each nucleus at each photon energy in the photodisintegration regime, see Figure 3.6). The cross sections for the photomeson regime were modeled using the newly developed Empirical Model presented in Section 4.2. These cross section tables although discussed here in the propagation context, are applicable to any astrophysical scenario where superheavy nuclei are present, including source simulations where superheavy UHECR interactions are of interest.

Although interaction tables and decays were implemented for all 2765 nuclei presented in Figure 3.3, the simulations discussed in the following sections here employed the highest time

cut-off possible (*i.e.* only stable nuclei were transported and the excluded species were assumed to decay immediately after production). This was necessary due to the large memory required for the interaction kernel of 2765 species. Therefore, studies of evaluating the impact of the time cut-off on the propagation are deferred to future works when PriNCe can be fully tested and optimized to run with a more inclusive nuclear cascade. The stable nuclei propagated are represented in Figure 3.1 which employed only 255 nuclear species.

PriNCe propagates nuclei in one dimension and it is not suitable for studying the effect of magnetic fields in the propagation. To facilitate such studies CRPropa 3 can be employed. CRPropa 3 (Alves Batista et al., 2016) is a versatile simulation tool designed to describe the propagation of cosmic rays and their secondary products over cosmological distances. It uses Monte Carlo methods to generate the primary particles and simulate their interactions, producing the spectra, compositions and arrival directions of secondaries resulting from the effect of all relevant energy-loss processes and magnetic deflections. The interaction models produced here are being implemented in CRPropa 3 in collaboration with the CRPropa 3 authors. Studies of the impact of magnetic fields are deferred to future works until the implementation is completed.

6.2 Limitations in predicting the UHECR composition

Before the impact of heavy nuclei in the propagation can be studied and compared to measured data, it is necessary to update the existing hadronic interaction codes used for air shower simulations which are used to estimate the dependence of $\langle X_{\rm max} \rangle$ and $\sigma(X_{\rm max})$ with $\ln A$. Currently, such relations have only been studied for nuclear masses up to $A = 56$ (Abreu et al., 2013) which exclude all superheavy nuclei. $\langle X_{\rm max} \rangle$ is found to be proportional to $\ln A$ and it is expected that this is also the case for superheavy nuclei, but for $\sigma(X_{\rm max})$ the situation is less clear. Figure 6.1 shows $\sigma(X_{\rm max})$ as a function of the mass A using the relations published by (Abreu et al., 2013) for different hadronic interaction codes. $\sigma(X_{\rm max})$ dependence on $\ln A$ was expressed by two components: a variance due to the composition and a variance due to the shower fluctuations. The latter component is a quadratic function fitted to EAS Monte Carlo simulations and represented by solid lines in Figure 6.1. The gray area has not been explored with EAS simulations and thus, the extrapolation of the fit is possibly unphysical. The increase of variance with A is inconsistent with the behavior for light nuclei, where an increase of the mass leads to a decrease of the variance. The reasoning is that for the first interaction the cross section is roughly A times larger than for a proton, and the nucleus can be considered as multiple nucleons moving independently and creating their own showers. In such scenario, the EAS of the nucleus is roughly the average of A proton showers, and a reduced variance would

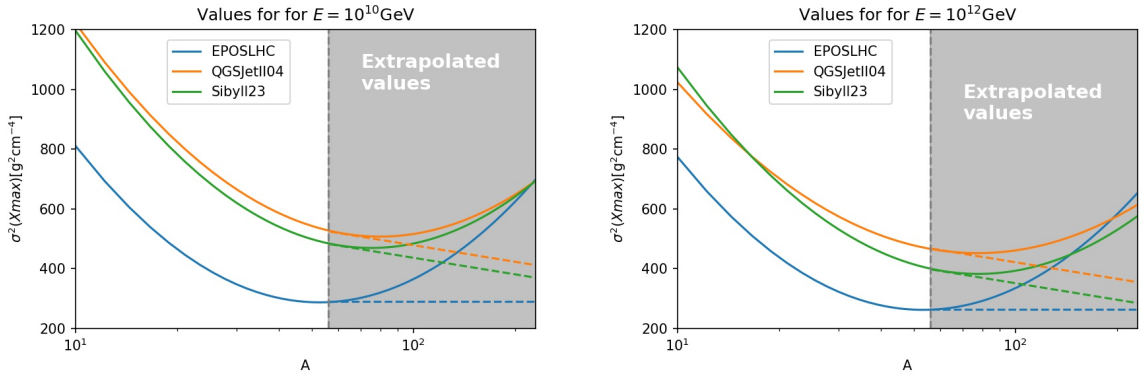

Figure 6.1: The dependence of $\sigma(X_{\max})$ on the mass as published by Abreu et al. (2013). The solid lines are quadratic fits to EAS simulations. The superheavy masses (gray region) have not studied and the validity of the extrapolation questionable. Dashed lines are linear extrapolations that keep the derivate of the curves constant above $A = 56$.

be expected. The linear extrapolations, shown with dashed lines, are obtained by preserving the slope of the curves for iron mass. These values could be used as a lower limit to the variance for superheavy nuclei and be employed in future composition studies in the absence of shower simulations for the needed nuclear masses.

6.3 Photonuclear interactions of superheavy nuclei

Figure 6.2 shows on the left the inelastic interaction cross section for different nuclei (indicated by the color of the curve), obtained from Talys . The species chosen have been used in the literature as 'surrogates' to represent different mass groups up to $A = 56$ (Heinze et al., 2019, Farrar and Piran, 2014). Each mass group includes all nuclei with mass between two consecutive surrogates (including the heavier one and excluding the lighter one), *e.g.* ^{14}N represents all nuclei with masses in the range $4 < A \leq 14$. The mass groups are chosen to cover approximately equal ranges of $\ln A$, because the observables $\langle X_{\max} \rangle$ and $\sigma(X_{\max})$ are mainly sensitive to this quantity. The surrogates for lighter mass groups $\{^{1}$H, ^{4}He, ^{14}N, ^{28}Si, ^{56}Fe$\}$ used in other works (Heinze et al., 2019, Farrar and Piran, 2014) are extended here by two extra mass groups with surrogates ^{92}Mo and ^{208}Pb, covering the range of superheavy nuclei, while keeping the logarithmic intervals.

As discussed in Chapter 3, the photodisintegration cross section is dominated by the GDR, and has a scaling remarkably close to proportionality with A. The similarities in the cross section per nucleon can be appreciated in the left panel of Figure 6.2. The theoretical reasoning was presented by Levinger and Bethe (1950) who applied the Thomas-Reiche-Kuhn sum rule to

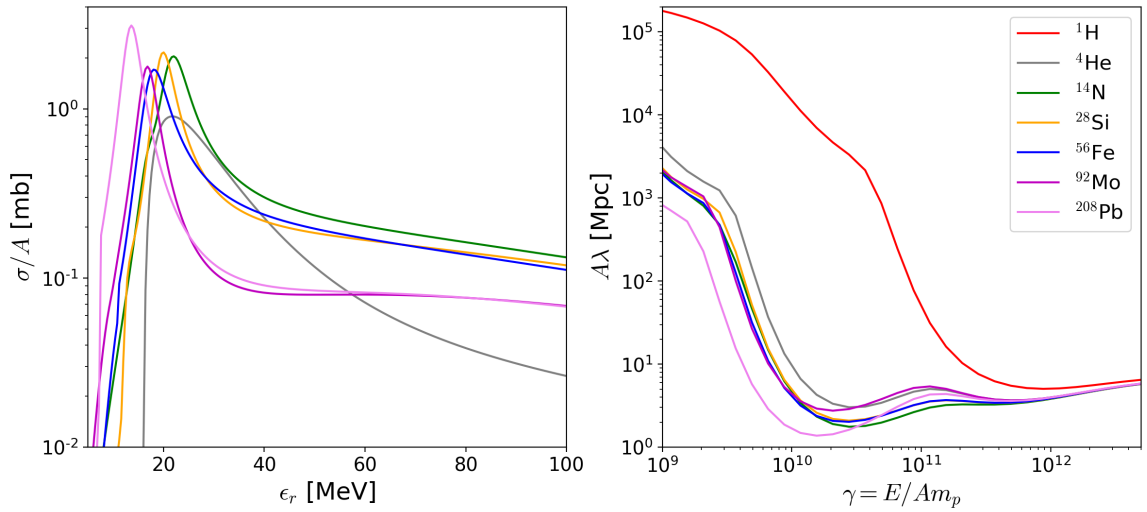

Figure 6.2: Left: photonuclear inelastic cross section per nucleon as a function of the photon energy in the nucleus rest frame. The cross sections are sampled from Talys (Koning et al., 2007). Right: interaction length per nucleon as a function of its Lorentz factor. The target photon spectrum includes both CMB and EBL photon fields (see Section 3.1.1) at redshift $z = 0$. The colors indicate different nuclear species, as shown in the legend.

nuclear photoabsorption, and found that the energy-integrated cross section $\int \sigma(\epsilon) d\epsilon \propto \frac{ZN}{A} \propto A$. Nevertheless, there are slight differences, *e.g.* the peak energy decreases approximately with $A^{-\frac{1}{3}}$. These relations are reflected also in the interaction rates.

In the right panel of Figure 6.2 we can see the interaction lengths scaled by the nucleon number as a function of the Lorentz boost. The interaction rates were calculated using Eq. 3.16, and the interaction lengths are inversely proportional to the rates:

$$\lambda_i(E_i, z) = 1/\Gamma_i(E_i, z), \tag{6.1}$$

where the dependency on the redshift z comes from the cosmological evolution of the target photon density spectrum. Figure 6.3 represents the CMB and EBL spectra, which constitute the main interaction target for UHECRs propagating in the intergalactic medium. The redshift values considered here are $0 \leq z \leq 1$, which cover distances up to over 3 Gpc (using the cosmological parameters given by Hinshaw et al., 2013). Such distances are large enough that all nuclei with Lorentz factor $\gamma \approx 10^{10}$ disintegrate completely.

The mass-scaled interaction lengths in Figure 6.2 reflect the mass dependence of the cross section per nucleon because the target photon spectrum looks the same in the cosmic-ray rest frame for nuclei with the same Lorentz factor. For ^{208}Pb, for example, the cross section peaks at

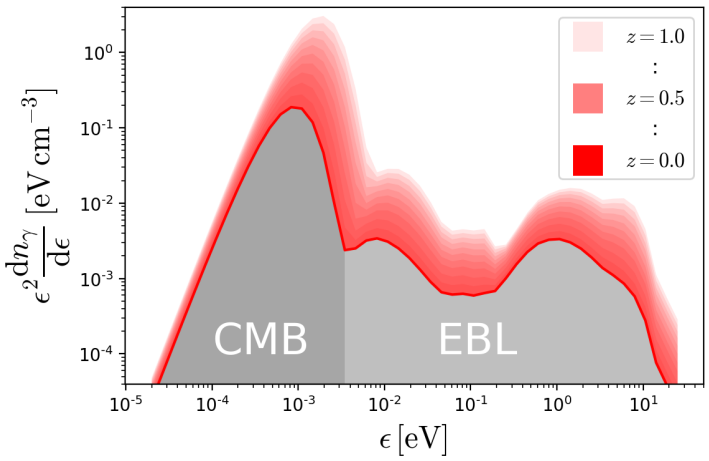

Figure 6.3: Extragalactic target photon spectrum and its dependence on the redshift z (different shades of red). The EBL model is based on Gilmore et al. (2012).

lower photon energies compared to other nuclei, and this reflects in the mass-scaled interaction length minimum positioned at a reduced value of the Lorentz factor relative to other nuclei. Additionally, nuclei with higher peaks in the cross section per nucleon exhibit deeper minima in the scaled interaction length. The minimum length (maximum interaction rate) occurs for the boost that superposes the CMB peak ($\epsilon^{\rm max}_{\rm CMB} \approx$ meV) and the GDR peak ($\epsilon^{\rm max}_{\rm GDR} \approx 10$ MeV), that is $\epsilon^{\rm max}_{\rm GDR}/\epsilon^{\rm max}_{\rm CMB} = \gamma \approx 10^{10}$. The conclusion from this is that the interaction lengths for two nuclei with the same boost are approximately reciprocal to the ratio of the masses

$$\frac{\lambda_{A_1}(\gamma)}{\lambda_{A_2}(\gamma)} \approx \frac{A_2}{A_1}. \tag{6.2}$$

This relation becomes exact for $\gamma \gtrsim 3 \cdot 10^{11}$ because of the onset of photomeson interactions, where the cross section per nucleon is universal for nuclei (see Chapter 4). In terms of total energy $E = \gamma A m_p$, the interaction lengths are shifted to higher energies for heavier nuclei, so for instance ^{28}Si has its minimum interaction length at an energy two times larger compared to ^{14}N.

Taking into account that the main disintegration channel for photodisintegrations of nuclei through the GDR is the loss of a nucleon, we can estimate the distance related to a certain mass loss as it propagates through the IGM. Starting with a nucleus of boost γ, mass A_k and interaction length λ_{A_k}, it is likely to interact after a distance $\lambda_{A_k} = \lambda_{A_k}(\gamma)$ with the loss of one nucleon (*i.e.* the mean interaction length). The product (with mass $A_k - 1$) subsequently would interact after a distance λ_{A_k-1}. Given Eq. 6.2 the relation $\lambda_{A_k-1} = \lambda_{A_k} \frac{A_k}{A_k-1}$ holds, given that photodisintegration products preserve the boost of the parent (see Section 4.2.3).

Subsequently, the product of the second interaction with mass $A_k - 2$ will interact in average after $\lambda_{A_k-2} = \lambda_{A_k-1}\frac{A_k-1}{A_k-2} = \lambda_{A_k}\frac{A_k}{A_k-2}$. By inference, the total average distance Λ for the loss of N_k nucleons is:

$$\Lambda(A_k, A_k - N_k) = \lambda_A + \lambda_{A_k}\frac{A_k}{A_k - 1} + \lambda_{A_k}\frac{A_k}{A_k - 2} + \cdots + \lambda_{A_k}\frac{A_k}{A_k - N_k} \tag{6.3}$$

$$= A_k\lambda_{A_k}(H_{A_k} - H_{A_k-N_k-1}), \tag{6.4}$$

where $H_n = \sum_{m=1}^{n}\frac{1}{m}$ is the nth harmonic number. This relation shows that heavier nuclei travel a longer distance until full disintegration. Additionally, if we define $\Lambda_A = \Lambda(A, 1) = A\lambda_A H_A$ as the full disintegration distance, Eq. 6.4 can be written as

$$\Lambda(A_k, A_k - N_k) = A_k\lambda_{A_k}(H_{A_k} - H_{A_k-N_k-1}) = \Lambda_{A_k} - \Lambda_{A_k-N_k}, \tag{6.5}$$

$$\Lambda_{A_k} = \Lambda_{A_k-N_k} + \Lambda(A_k, A_k - N_k). \tag{6.6}$$

Equation 6.6 leads to the conclusion that the distance for full disintegration is the addition of the distance required to lose N_k nucleons and the distance to fully disintegrate the remaining nucleus. Given two nuclei with masses related as $A_k > A_l$, and using the notation $\Lambda_A = \Lambda(A, 1)$ for the full disintegration distance of species with mass A, we can write:

$$\frac{\Lambda_{A_k}}{\Lambda_{A_l}} = \frac{A_k\lambda_{A_k}H_{A_k}}{A_l\lambda_{A_l}H_{A_l}} \tag{6.7}$$

$$\frac{\Lambda_{A_k}}{\Lambda_{A_l}} \approx \frac{H_{A_k}}{H_{A_l}} > 1 \tag{6.8}$$

$$\frac{\Lambda_{A_k}}{\Lambda_{A_l}} \approx \frac{\mathrm{g} + \ln A_k}{\mathrm{g} + \ln A_l}, \tag{6.9}$$

where Eq. 6.2 was employed, as well as the approximation $H_A = \mathrm{g} + \ln A$, where g=0.5772... is the Euler-Mascheroni constant. This relation is limited to cases where Eq. 6.2 holds, or where it is bound to

$$\frac{A_k\lambda_{A_k}}{A_l\lambda_{A_l}} < \frac{H_{A_l}}{H_{A_k}}. \tag{6.10}$$

The approximation for H_A can be used in Eq. 6.6 to obtain a simpler relation for the loss of

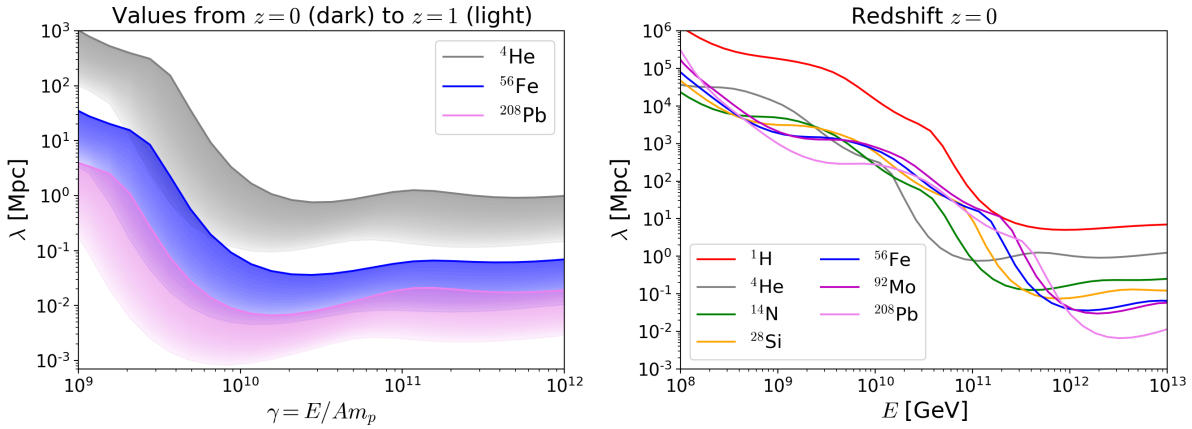

Figure 6.4: Left: Interaction lengths for different nuclides as function of the boost, with the dependence on redshift given by the darkness of the color (darkest is $z = 0$, lightest is $z = 1$). The redshift dependence preserves the ratios of the rates. Right: Interaction lengths as a function of the total UHECR energy.

nucleons,

$$\Lambda(A_k, A_k - N_k) = A_k \lambda_{A_k} \ln\left(\frac{A_k}{A_k - N_k}\right) \tag{6.11}$$

It should be noted that as the disintegration products lose mass, their energy will scale down proportionally due to boost conservation since $(\frac{E_{A_k - N_k}}{E_{A_k}} = \frac{A_k - N_k}{A_k})$. For the distances around Λ_A, the injected nucleus appears as a number A of free nucleons with the same boost, or energy $E_p = E_{A_k}/A_k$. This means that nuclei of the same boost factor will ultimately disintegrate and contribute to proton spectra at the same energy, regardless of the starting mass. Further propagation will lead to additional energy loss.

The redshift dependence of the interaction lengths does not change the relations obtained above. As Figure 6.3 shows, the shape of the SED is preserved for larger redshifts, with slight shift to higher energies. Nuclei with the same boost 'see' the same target photon spectrum regardless of the species, and their interaction rates are related in the same manner as for local redshift $z = 0$. This is verified in Figure 6.4 (left): increasing redshift decreases the interaction length for different species in the same degree, preserving roughly the relative ratios.

Figure 6.4 (right) shows a comparison of the interaction rates in terms of the total cosmic-ray energy. In contrast to the right panel of Figure 6.2, the curves are now shifted in energy by A (energy-boost relation), while the rates are shifted by $1/A$. These effects move the curves roughly along $E^{-2} \propto A^{-2}$, as visible in the relative positions of the minima. Such ordering of the rates would cause a mass-dependent *photodisintegration cutoff* on the flux spectra of the

isotopes, similarly to a rigidity-dependent cutoff often assumed for the spectra ejected from the astrophysical source, due to the limitations of sources to confine magnetically particles above a certain rigidity (Farrar and Piran, 2014, Muzio et al., 2019, Heinze et al., 2019). Indeed, assuming constant injection of UHECR nuclei with a power-law spectrum, after propagation the spectra would show cutoffs at the energies where the interaction lengths show a steep decrease due to the onset of interactions with the CMB. Such cutoffs would appear at higher energies for larger mass species, reflecting the A-scaling of the interaction lengths. The rigidity-dependent cutoff works similarly because the cutoff energy scales as $E_{\rm cut} = R_Z Z$ (R_Z being the rigidity), and the charge in nuclei is proportional to the mass.

In addition, this effect creates regions of energy where light nuclei have shorter interaction lengths compared to heavier ones. From energy $7 \cdot 10^9$ GeV, iron and molybdenum have the largest interaction lengths up to around $3 \cdot 10^{11}$ GeV. This means that if a mixed composition is injected by a source at such energies, the average composition will become heavier as the cosmic rays propagate away from the source. For example, at 10^{11} GeV helium and nitrogen have lengths just below 1 Mpc Figure 6.4, while for iron and molybdenum it is ten times larger. The relative amounts of helium and molybdenum at this energy would then evolve with distance d as

$$\frac{J_4(d)}{J_{92}(d)} = \frac{J_4(0)}{J_{92}(0)} \exp\left(-d\left(\frac{1}{\lambda_4} - \frac{1}{\lambda_{92}}\right)\right) \approx \frac{J_4(0)}{J_{92}(0)} \exp\left(-\frac{9}{10}d\right), \tag{6.12}$$

where $J_k(0)$ is the intensity emitted by the source and $J_k(d)$ is the intensity at distance d from the source. Therefore, after 10 Mpc the relative intensity would have decreased by a factor 10^{-4} (becomes 10^4 times heavier). If we consider the neutron star merger GW170817, which occurred in a galaxy at a distance of 40 Mpc (Abbott et al., 2017b), and assume an emitted cosmic-ray composition like that of the SoS light-to-superheavy fraction ($\frac{J_4(0)}{J_{92}(0)} \approx 10^9$), UHECRs of energies 10^{11} GeV would have a much higher content of heavy nuclei intensity at Earth ($\frac{J_4(40\ \mathrm{M}pc)}{J_{92}(40\ \mathrm{M}pc)} \approx 10^{-7}$). This illustrates how in the case of superheavy nuclei, propagation may act as a 'mass filter' that can distort considerably the composition leaving the source in favor of heavier nuclei. This effect may also be studied among other lighter species, *e.g.* nitrogen and iron at 10^{11} GeV. We should point out that these differences in rates originate from different interaction regimes, *i.e.* helium at 10^{11} GeV is interacting with the CMB while iron at 10^{11} GeV is interacting with the EBL. It can be foreseen that measuring the composition precisely at these energies could allow for a verification of EBL models. Admittedly, we would also need an estimate of the compositions in the sources and it might be difficult to reach the required precision.

An important point is that at an energy around $2 \cdot 10^{11}$ GeV (near the GZK limit) molybdenum

has an interaction rate similar to protons, although the latter interacts through photomeson production. If we compare the typical inelasticities, a proton loses about 20% of its energy per interaction (see Chapter 3), while a molybdenum nucleus will lose only $1/92 \approx 1\%$. This also implies that in the vicinity of the source, injected protons will lose energy faster than superheavy nuclei around the molybdenum mass, leading to an increase of average mass at those energies. However, this effect would disappear further from the source because secondaries injected by molybdenum have the same boost and are injected at energies where the proton losses are much smaller in comparison.

Finally, a comment on the interaction rates of superheavy nuclei. At present date, UHECR energies up to $3{\cdot}10^{11}$ GeV have been measured but the composition has been estimated only up to about $4 \cdot 10^{10}$ GeV. If superheavy nuclei are being injected in the sources, as we hypothesize, the imprints could appear in the energy ranges where we have not measured the composition (beyond $4 \cdot 10^{10}$ GeV). This is because if iron is present in the highest energies (as supported by studies that fit the spectrum and composition) it could be a product of superheavy disintegrations. If so, the relations between interaction rates would imply correlations between the composition at $4 \cdot 10^{10}$ GeV and higher energies, which could be predicted using propagation codes such as PriNCe .

6.4 Propagation of superheavy nuclei using PriNCe

This section presents the full simulations for the transport of superheavy nuclei with PriNCe where all nuclear interactions and productions channels are included up to superheavy masses. The cases considered only one species injected from the source and at a unique energy (*i.e.* the spectrum 'injected' in the propagation calculation is a delta function of the energy). These scenarios are suitable for comparison with the relations found in the previous section, and therefore ease the interpretation of the results.

As the injected nucleus propagates and interacts, secondary nuclei are produced at the same boost and will further disintegrate at an equivalent regime (see Figure 6.2). At sufficiently large distances, full disintegration occurs and only protons would remain. At intermediate distances, the secondaries are distributed over the injected mass and $A = 1$. The mass and energy will be correlated because of the narrow energy distribution of the injection and the boost conservation of secondaries. Figure 6.5 represents the mass evolution during propagation (up to 10 Mpc) where each panel corresponds to a different mass group surrogate injected. The injection boost is $\gamma = 2{\cdot}10^{10}$, which corresponds to the maximum interaction rate (minimum interaction length) for all mass group as seen in Figure 6.2. Thus the corresponding injection energies are: $5.6 \cdot 10^{11}$ GeV for silicon, $1.12 \cdot 10^{12}$ GeV for iron, $1.84 \cdot 10^{12}$ GeV for molybdenum and $4.16 \cdot 10^{12}$ GeV for

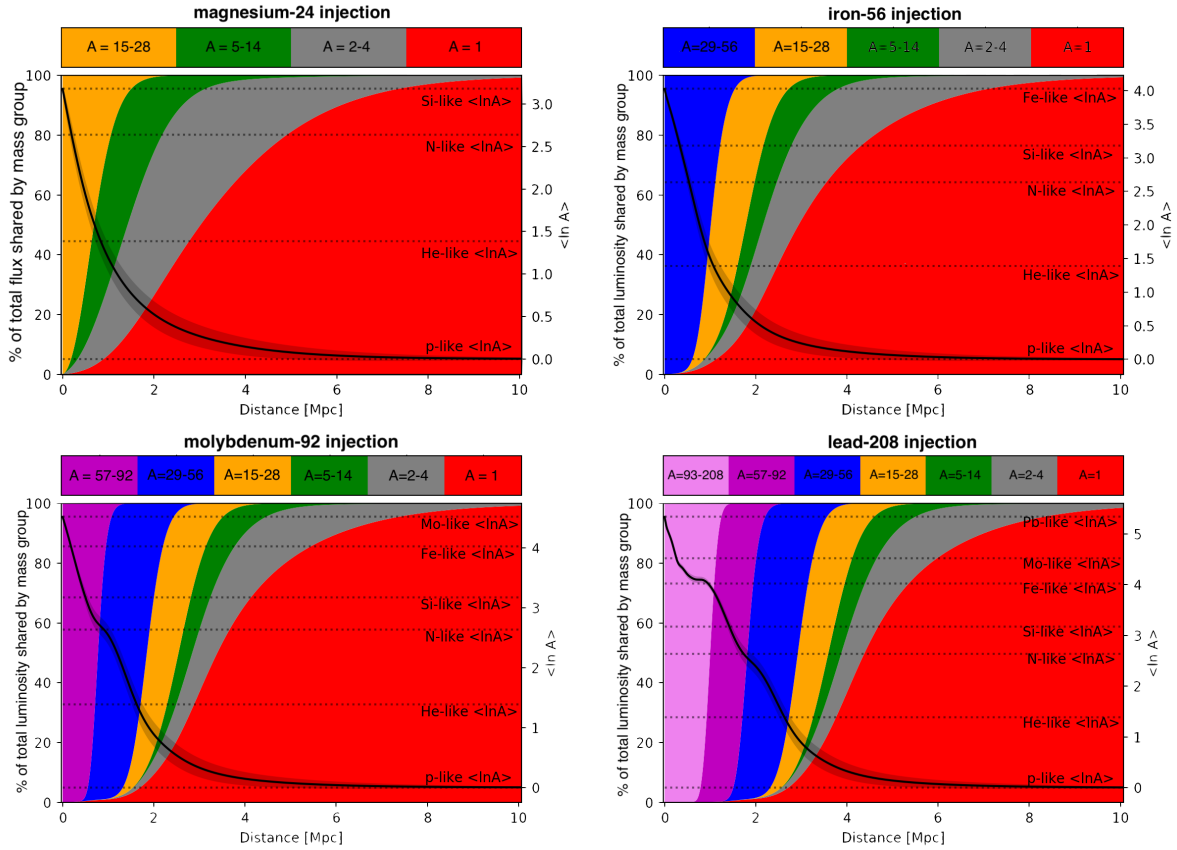

Figure 6.5: Evolution of the mass composition of cosmic rays with propagation. In each plot, a single species is emitted by a source art 10 Mpc, whose initial spectrum is assumed to be a delta function in Lorentz boost, $\gamma = 2 \cdot 10^{10}$. The injected isotope in each case is silicon (top left), iron (top right), molybdenum (bottom left), and lead (bottom right). The stacked plots represent the relative luminosity of each mass group (given on the y axis on the left hand side), while the black curve represents $\langle \ln A \rangle$ and the shaded region represents its spread, $\sigma_{\ln A}$ (given on the y axis on the right hand side).

lead.

The color-shaded regions show stacked plots where the corresponding heights represent the share of the total luminosity taken by each mass group. The variation of the limits between regions follow the redistribution of luminosity resulting from the disintegrations of the injected species and also the decay products. The percentages of luminosity are indicated by the left y-axis, and the mass-group colors are indicated above each figure. The black curve is quantified by the right y-axis, and describes the values of $\langle \ln A \rangle$ as a function of the distance. The shadow surrounding the black curve quantifies the corresponding $\sigma_{\ln A}$. It should be noted this $\ln A$ is computed with nuclei at different energies (in the range γm_p - $\gamma A m_p$). In order to be comparable

to the values reported by PAO, the averaging energy range needs to correspond to the reported energy bins.

The most striking feature is that groups are populated in sequence of heavier to lighter. This is notable because the disintegration of nuclei can produce secondaries of multiple masses, and when all secondaries are disintegrating, it could be possible intermediate nuclei like helium receive multiple injections. Instead, Figure 6.5 is compatible with a photodisintegration process that injects with higher probability nuclei in the mass-vicinity of the parent. This is because in the photodisintegration of nuclei, one nucleon emission is the process with highest probability for most species, and consequently the remainder $A-1$ product as well. Therefore, production of a given intermediate species is most important when the intensity of its immediate neighbors of heavier-mass is maximal. We can call this a 'disciplined disintegration' (DD) effect, where heavy nuclei produce predominantly immediate mass neighbors, and the lightest nuclei can only be produced sizeably once all heavier species have disintegrated.

This is consistent with the relations found in the previous section. Indeed, from Eq. 6.11 and Eq. 6.6 we obtain

$$\frac{\Lambda_{A_k}}{\Lambda_{A_j}} = \frac{\ln A_k}{\ln A_j} \tag{6.13}$$

which reflects the notion that heavier nuclei propagate further than lighter nuclei with the same Lorentz boost. However, the difference in distance is not very large: for lead is only 1.6 times that of silicon. The simulation is roughly in agreement with the approximate relations.

The DD effect also occurs for Lorentz boosts corresponding to the photomeson interactions $\gamma \gtrsim 3 \cdot 10^{11}$ because nucleon emission is also the dominant mechanism. This is the case for both the SpM and the EM models of photomeson interaction (see Chapter 4). The DD effect is evidenced also in results found with an analytical approach to propagation (Hooper et al., 2008) which also assumes only one nucleon emission in the disintegration of nuclei.

6.5 Outlook on future applications of the model

Nuclei heavier than iron (superheavy) are expected to be present in extragalactic UHECR accelerators where compositions heavier than SoS-like could potentially be found (see Section 2.2). If superheavy nuclei are accelerated in the source into the ultra-high-energy regime, they can in principle escape and be emitted as superheavy UHECRs, provided that the source is optically thin to photointeractions up to the highest energies.

In this chapter I have presented the extension of current interaction models of UHECRs to include superheavy nuclides. This was achieved by collecting decay data, sampling Talys , and

producing a new photomeson model (see Chapter 4). The extension up to mass $A = 208$ adds more than 2100 nuclides to the existing interaction models in PriNCe , and would amount to a comparable addition in other existing propagation codes, all of which only consider masses up to $A = 56$. The interaction tables have been created with reproducibility in mind, and can be implemented in other propagation codes employed by the community as well as simulations of UHECR sources. The mass range limitations of current $\sigma(X_{\max})$ fits, creates difficulties in performing UHECR spectrum and composition using superheavy nuclei. We would therefore recommend EAS studies with superheavy nuclei, in order to extend the mass range of $\sigma(X_{\max})$ relations, to allow evaluation of the impact of superheavy in the UHECR composition.

The interaction lengths for propagation of nuclei (including superheavy) through the intergalactic medium have been calculated by estimating the interaction with the CMB and EBL photons. Approximate relations were obtained by noting that for nuclei with the same Lorentz boost, their interaction lengths are in reciprocal relation to their masses. Additionally the full disintegration was estimated and it was found that for two nuclei with the same Lorentz boost the total disintegration lengths are in proportional relation to the ratio of the natural logarithm of their masses. These relations hold not only for superheavy nuclei, but for all nuclear masses. Finally we have identified UHECR energies where superheavy nuclei have larger interaction distances than lighter nuclei. This effect is connected to the relative photon densities in the CMB and the EBL. The composition changes with energy could be used as an indicator for the relative strength of the CMB and EBL, by comparing the relative disintegration of nuclei with different masses, given assumptions of injection by the sources. These energies are potential places where to test the presence of superheavy isotopes in the composition of UHECR because of the differences in disintegration rate impact directly the composition.

The propagation of superheavy nuclei was performed with PriNCe and compared to propagation of lighter nuclei. The effect of disciplined disintegration (DD) was defined in this work in order to describe the way in which nuclei disintegrate predominantly into species of nearby masses. This effect produces a cascade that moves smoothly from the injected mass to the lighter species. This is not a trivial result, given that many different disintegration channels are present in the interaction tables, including multiple nucleon losses per interaction. The DD effect is also expected to occur for UHECR photomeson interactions with the extragalactic medium. The simulations with PriNCe have been found in agreement with the approximate relations.

These findings, together with the implementation of superheavy elements in a numerical framework, can potentially lay the groundwork for future studies involving new fits to the UHECR spectrum and composition, for which softwares like PriNCe and CRPropa 3 can be used, provided that EAS simulations are available. Another step is the impact of magnetic fields on the propagation of superheavy nuclei for which CRPropa 3 would be more suitable.

Chapter 7

Conclusion and Outlook

In this thesis I have introduced models that improve the current treatment in three different fronts of high-energy astronuclear research. The main distinctive aspect of these models compared to others employed in current phenomenological UHECR studies is that they draw from insights of theoretical and experimental nuclear physics. Such emphasis on the accuracy of astronuclear models is strongly motivated by the ever-increasing amount of astrophysical data on diverse messengers such as cosmic rays, neutrinos and gamma rays. Photo-nuclear interactions at high energies are the connecting link between these messengers, and therefore an accurate modeling of the physics behind these interactions is of crucial importance.

After introducing in Chapter 2 some core concepts relevant for the astrophysical discussion, Chapter 3 detailed the relevant interactions and the modeling tools. Chapter 4 revisited the model used conventionally in the literature for photointeractions of Ultra-High Energy Cosmic Rays leading to meson production (photomeson interactions), and a disagreement was found compared to experimental data. It was shown that this treatment overestimates the production of pions and underestimates the disintegration of nuclei in photomeson interactions. I have introduced a new photomeson model (Empirical Model, EM) that improves on these issues by using a combination of experimental data, empirical relations and theoretical considerations. This model is thus better in describing experimental data and provides a more realistic picture of photomeson production by UHECR nuclei.

I have implemented the EM in the code NeuCosmA and tested its impact in examples of two extragalactic sources thought to be potential candidates for UHECR sources, namely Tidal Disruption Events (TDEs) and Gamma-Ray Bursts (GRBs). The impact of the model showed that neutrino production from photomeson interactions of nuclei is reduced, and the disintegration of nuclei occurs more efficiently, when compared to the standard photomeson model used. The EM predictions are sensitive to the mass composition injected in the source, which is a feature not accounted before. In the TDE example the neutrino flux was reduced by 50%. In the GRB example, the impact of the model was dependent on the efficiency of the disintegration, and the maximum impact was found when nuclei did not disintegrate fully, thus

contributing more to meson production. The EM has been published (Morejon et al., 2019a) and the software made available (Morejon, 2019b) for facilitating the reproducibility of results and facilitating its implementation in other existing codes and calculation frameworks in High Energy Particle Astrophysics.

Chapter 5 focused on photon production from photodisintegration of nuclei. I produced tools to compile available data related to photoemission and employ a more sophisticated approach compared to state-of-the-art models. I then integrated this model into a numerical software for astrophysics, developed in parallel by my collaborators at DESY. This new piece of software was built from a coupling of two previously existing codes: NeuCosmA (Baerwald et al., 2013), and AM^3 (Gao et al., 2017), with the addition of the present photodisintegration photon model.

In order to test the improvement factor of the model in a specific astrophysical scenario, we modeled the multi-wavelength emission from the core of the galaxy Centaurus A in a lepto-hadronic framework including the presence of high-energy cosmic-ray iron nuclei, assumed to be co-accelerated with electrons in the jet (Rodrigues et al., in development). The improvements introduced by this new model compared to the current literature can be summarized as follows: *(a)*the total cross section is approximated as a energy-dependent curve following known trends across nuclear isotopes; *(b)* the rate of photodisintegration is given explicitly as a function of the energy of the nucleus; *(c)* the photons emitted by nuclei have a distribution in energy; *(d)* the entire nuclear cascade of lighter isotopes is computed (and not only the accelerated iron); *(e)* the gamma rays that are emitted by unstable isotopes are allowed to re-interact in the source, which the study concludes is optically thick to these photon energies; and *(f)* the electron-position production from hadronic species is considered, leading to additional electrons that contribute to the overall photon emission.

Unlike the conclusions of other works that use simpler models, this study has shown that such a complex set of interactions leads to a final photon spectrum that differs from the observations. Firstly, this emphasizes the importance in astrophysics of self-consistent numerical modeling of sources and of nuclear physics insights. Secondly, it shows that the specific case of Centaurus A cannot be easily explained by a simple power-law acceleration of nuclei. Instead, other more complex source characteristics must be considered in future works to potentially explain these observations.

Finally, Chapter 6 introduced for the first time the interactions of UHECR nuclei heavier than iron (superheavy) in the context of propagation. I have produced tables for the interactions and implemented them in PriNCe. The additions include the disintegration data for such nuclei. The contribution amounts to more than 2100 species for which the main decay mode, the interactions cross sections and the production channels were collected experimentally or derived from models. The photodisintegration interactions were obtained by sampling interactions in

TALYS , and the photomeson model used was the EM presented in Chapter 4. For reproducibility of these results and implementation in other propagation frameworks, this model is now available as a software tool that generates the interaction tables.

The discussion of the interaction rates for propagation of superheavy nuclei through the intergalactic medium lead to deriving approximate relations for the total disintegration length. Notably it was determined for nuclei with the same Lorentz boost, that their interaction lengths are in reciprocal relation to their masses, and that the estimated full disintegration length are proportional to the ratio of the natural logarithm of their masses. UHECR energy ranges were identified where superheavy nuclei propagate further than lighter nuclei. The estimation of this effect was performed using the approximate relations and it was predicted that it would produce a propagation-induced enhancement of the intensities of superheavy isotopes as they leave the source.

The concept of disciplined disintegration (DD) is also introduced, whereby nuclei disintegrate predominantly into species of nearby masses, leading to a smooth transition of the luminosity from the injected mass to the lighter species, always respecting the mass hierarchy. This effect is most visible in the propagation of superheavy nuclei, due to the large number of isotopes in the disintegration chain. I then employed the code PRINCE, which I have extended to superheavy masses in order to calculate the propagation of superheavy nuclei numerically, which has not yet been done in other works. The results of the numerical propagation were in agreement with the analytical formulas derived.

The implementation of the interactions in CRPROPA 3 is also planned in the future. This will allow us to estimate for the first time the role of magnetic fields in the propagation of superheavy nuclei. Additionally, fits to the UHECR spectrum and composition are left as proposals for future works, once the EAS models include superheavy masses and predictions on the observables can be performed.

This thesis focused on improving three aspects of state-of-the-art multimessenger research: neutrino production through photomeson interactions of cosmic-ray nuclei; photon production from cosmic-ray photodisintregration; and superheavy UHECR isotopes, for which the first numerical tool was introduced in this work. The results obtained have demonstrated that more realistic nuclear models are an essential component of astrophysical studies aiming to constrain the physics behind the UHECR phenomenon.

At the same time, the new models contain simplifications that allow their usage in the codes employed here, which means future refinements may be necessary. In the case of the photomeson model, specific comparison to the yields of nuclear fragments is not overall satisfactory. This is partly because the model employs expressions for the mean production cross section, which may deviate from individual cases. As for the photoproduction models, the main shortcoming

is the common parameters for different nuclei, which does not improve substantially on existing treatments. Nevertheless, the compiled data can be employed to prepare improved versions of the model in the future if the simulation codes or the astrophysical scenario would require it. The propagation of superheavy nuclei suggests interesting results, and several approximate relations with analytical form were obtained. However, such simulations are computationally expensive and will require optimizations, possibly reducing the number of species considerably. This limits currently the practical usage of this model for larger scale studies such as a fit to the cosmic ray spectrum.

These new models have been published as open-source software, in hope that future phenomenological astrophysics studies will be able to make use of these improved tools.

Bibliography

A. Aab, P. Abreu, et al. Testing hadronic interactions at ultrahigh energies with air showers measured by the pierre auger observatory. *Phys. Rev. Lett.*, 117:192001, Oct 2016. doi: 10.1103/PhysRevLett.117.192001. URL https://link.aps.org/doi/10.1103/PhysRevLett.117.192001.

A. Aab et al. Muons in air showers at the Pierre Auger Observatory: Mean number in highly inclined events. *Physical Review D - Particles, Fields, Gravitation and Cosmology*, 91(3): 1–12, 2015a. ISSN 15502368. doi: 10.1103/PhysRevD.91.032003.

A. Aab et al. The Pierre Auger Cosmic Ray Observatory. *Nucl. Instrum. Meth.*, A798:172–213, 2015b. doi: 10.1016/j.nima.2015.06.058.

A. Aab et al. Observation of a Large-scale Anisotropy in the Arrival Directions of Cosmic Rays above 8×10^{18} eV. *Science*, 357(6537):1266–1270, 2017. doi: 10.1126/science.aan4338.

A. Aab et al. An Indication of anisotropy in arrival directions of ultra-high-energy cosmic rays through comparison to the flux pattern of extragalactic gamma-ray sources. *Astrophys. J.*, 853(2):L29, 2018. doi: 10.3847/2041-8213/aaa66d.

M. G. Aartsen et al. Evidence for High-Energy Extraterrestrial Neutrinos at the IceCube Detector. *Science*, 342:1242856, 2013. doi: 10.1126/science.1242856.

M. G. Aartsen et al. Extending the Search for Muon Neutrinos Coincident with Gamma-Ray Bursts in IceCube Data. *The Astrophysical Journal*, 843(2):112, jul 2017a. ISSN 1538-4357. doi: 10.3847/1538-4357/aa7569. URL https://iopscience.iop.org/article/10.3847/1538-4357/aa7569.

M. G. Aartsen et al. The IceCube Neutrino Observatory: Instrumentation and Online Systems. *JINST*, 12(03):P03012, 2017b. doi: 10.1088/1748-0221/12/03/P03012.

M. G. Aartsen et al. Extending the search for muon neutrinos coincident with gamma-ray bursts in IceCube data. *Astrophys. J.*, 843(2):112, 2017c. doi: 10.3847/1538-4357/aa7569.

M. G. Aartsen et al. Astrophysical neutrinos and cosmic rays observed by IceCube. *Advances in Space Research*, 62(10):2902–2930, nov 2018a. ISSN 18791948. doi: 10.1016/j.asr.2017.05.030. URL https://www.sciencedirect.com/science/article/pii/S0273117717303757.

M. G. Aartsen et al. Multimessenger observations of a flaring blazar coincident with high-energy neutrino IceCube-170922A. *Science*, 361(6398):eaat1378, 2018b. doi: 10.1126/science.aat1378.

R. U. Abbasi et al. Search for EeV protons of galactic origin. *Astroparticle Physics*, 86:21–26, jan 2017. ISSN 09276505. doi: 10.1016/j.astropartphys.2016.11.001.

R. U. Abbasi et al. Depth of Ultra High Energy Cosmic Ray Induced Air Shower Maxima Measured by the Telescope Array Black Rock and Long Ridge FADC Fluorescence Detectors and Surface Array in Hybrid Mode. *The Astrophysical Journal*, 858(2):76, may 2018. ISSN 1538-4357. doi: 10.3847/1538-4357/aabad7. URL http://stacks.iop.org/0004-637X/858/i=2/a=76?key=crossref.d43b9130aaa7e70efed1703ceb0c527c.

B. P. Abbott et al. Multi-messenger Observations of a Binary Neutron Star Merger. *Astrophys. J.*, 848(2):L12, 2017a. doi: 10.3847/2041-8213/aa91c9.

B. P. Abbott et al. GW170817: Observation of Gravitational Waves from a Binary Neutron Star Inspiral. *Phys. Rev. Lett.*, 119(16):161101, 2017b. doi: 10.1103/PhysRevLett.119.161101.

A. Abdo et al. Fermi Large Area Telescope View of the Core of the Radio Galaxy Centaurus A. *Astrophys. J.*, 719:1433–1444, 2010a. doi: 10.1088/0004-637X/719/2/1433.

A. A. Abdo et al. Fermi Gamma-ray Imaging of a Radio Galaxy. *Science*, 328:725–729, 2010b. doi: 10.1126/science.1184656.

P. Abreu et al. Interpretation of the Depths of Maximum of Extensive Air Showers Measured by the Pierre Auger Observatory. *JCAP*, 1302:026, 2013. doi: 10.1088/1475-7516/2013/02/026.

T. Abu-Zayyad et al. The surface detector array of the Telescope Array experiment. *Nucl. Instrum. Meth.*, A689:87–97, 2013. doi: 10.1016/j.nima.2012.05.079.

M. Ackermann et al. Constraining the High-Energy Emission from Gamma-ray Bursts with Fermi. *Astrophys. J.*, 754:121, 2012. doi: 10.1088/0004-637X/754/2/121.

S. Adrián-Martínez et al. Letter of intent for KM3NeT 2.0. *Journal of Physics G: Nuclear and Particle Physics*, 43(8):084001, jun 2016. ISSN 13616471. doi: 10.1088/0954-3899/43/8/084001. URL https://iopscience.iop.org/article/10.1088/0954-3899/43/8/084001https://iopscience.iop.org/article/10.1088/0954-3899/43/8/084001/meta.

O. Adriani et al. PAMELA Measurements of Cosmic-ray Proton and Helium Spectra. *Science*, 332:69–72, 2011. doi: 10.1126/science.1199172.

M. Ageron et al. ANTARES: The first undersea neutrino telescope. *Nuclear Instruments and Methods in Physics Research, Section A: Accelerators, Spectrometers, Detectors and Associated Equipment*, 656(1):11–38, nov 2011. ISSN 01689002. doi: 10.1016/j.nima.2011.06.103.

M. Aguilar et al. First Result from the Alpha Magnetic Spectrometer on the International Space Station: Precision Measurement of the Positron Fraction in Primary Cosmic Rays of 0.5–350 GeV. *Phys. Rev. Lett.*, 110:141102, 2013. doi: 10.1103/PhysRevLett.110.141102.

F. Aharonian and A. M. Taylor. Limitations on the photo-disintegration process as a source of VHE photons. *Astroparticle Physics*, 34(5):258–266, 2010. ISSN 09276505. doi: 10.1016/j.astropartphys.2010.08.004. URL http://dx.doi.org/10.1016/j.astropartphys.2010.08.004.

F. Aharonian et al. Discovery of the binary pulsar PSR B1259-63 in very-high-energy gamma rays around periastron with H.E.S.S. *Astron. Astrophys.*, 442:1, 2005. doi: 10.1051/0004-6361:20052983.

F. Aharonian et al. Discovery of very high energy gamma-ray emission from Centaurus A with H.E.S.S. *Astrophys. J.*, 695:L40–L44, 2009. doi: 10.1088/0004-637X/695/1/L40.

A. Airapetian et al. Quark fragmentation to $\pi\pm$, $\pi 0$, $k\pm$, p and $\bar{p}$ in the nuclear environment. *Physics Letters B*, 577(1):37 – 46, 2003. ISSN 0370-2693. doi: https://doi.org/10.1016/j.physletb.2003.10.026. URL http://www.sciencedirect.com/science/article/pii/S0370269303015740.

A. Airapetian et al. Hadronization in semi-inclusive deep-inelastic scattering on nuclei. *Nuclear Physics B*, 780(1):1 – 27, 2007. ISSN 0550-3213. doi: https://doi.org/10.1016/j.nuclphysb.2007.06.004. URL http://www.sciencedirect.com/science/article/pii/S055032130700466X.

A. Airapetian et al. and The HERMES Collaboration. Hadron formation in deep-inelastic positron scattering in a nuclear environment. *The European Physical Journal C - Particles and Fields*, 20(3):479–486, May 2001. ISSN 1434-6052. doi: 10.1007/s100520100697. URL https://doi.org/10.1007/s100520100697.

R. Aloisio, V. Berezinsky, P. Blasi, A. Gazizov, S. Grigorieva, and B. Hnatyk. A dip in the UHECR spectrum and the transition from galactic to extragalactic cosmic rays. *Astropart. Phys.*, 27:76–91, 2007. doi: 10.1016/j.astropartphys.2006.09.004.

R. Aloisio, V. Berezinsky, and A. Gazizov. Ultra High Energy Cosmic Rays: The disappointing model. *Astropart. Phys.*, 34:620–626, 2011. doi: 10.1016/j.astropartphys.2010.12.008.

R. Aloisio, V. Berezinsky, and A. Gazizov. Transition from galactic to extragalactic cosmic rays. *Astroparticle Physics*, 39-40:129–143, dec 2012. ISSN 0927-6505. doi: 10.1016/J.ASTROPARTPHYS.2012.09.007. URL https://www.sciencedirect.com/science/article/pii/S092765051200182X?via{%}3Dihub.

R. Aloisio, D. Boncioli, A. Di Matteo, A. F. Grillo, S. Petrera, and F. Salamida. SimProp v2r4: Monte Carlo simulation code for UHECR propagation. *JCAP*, 1711(11):009, 2017. doi: 10.1088/1475-7516/2017/11/009.

R. Alves Batista and J. Silk. Ultrahigh-energy cosmic rays from tidally-ignited white dwarfs. *Phys. Rev. D*, 96:103003, Nov 2017. doi: 10.1103/PhysRevD.96.103003. URL https://link.aps.org/doi/10.1103/PhysRevD.96.103003.

R. Alves Batista, D. Boncioli, A. di Matteo, A. van Vliet, and D. Walz. Effects of uncertainties in simulations of extragalactic UHECR propagation, using CRPropa and SimProp. *JCAP*, 1510(10):063, 2015. doi: 10.1088/1475-7516/2015/10/063.

R. Alves Batista, A. Dundovic, M. Erdmann, K.-H. Kampert, D. Kuempel, G. Müller, G. Sigl, A. van Vliet, D. Walz, and T. Winchen. CRPropa 3 - a Public Astrophysical Simulation Framework for Propagating Extraterrestrial Ultra-High Energy Particles. *JCAP*, 1605(05):038, 2016. doi: 10.1088/1475-7516/2016/05/038.

R. Alves Batista, R. M. de Almeida, B. Lago, and K. Kotera. Cosmogenic photon and neutrino fluxes in the Auger era. *JCAP*, 1901(01):002, 2019a. doi: 10.1088/1475-7516/2019/01/002.

R. Alves Batista et al. Secondary neutrino and gamma-ray fluxes from SimProp and CRPropa. *Journal of Cosmology and Astroparticle Physics*, 2019(5):006, may 2019b. doi: 10.1088/1475-7516/2019/05/006.

R. Alves Batista et al. Open Questions in Cosmic-Ray Research at Ultrahigh Energies. *Front. Astron. Space Sci.*, 6:23, 2019c. doi: 10.3389/fspas.2019.00023.

M. Amenomori et al. First Detection of Photons with Energy Beyond 100 TeV from an Astrophysical Source. *Phys. Rev. Lett.*, 123(5):051101, 2019. doi: 10.1103/PhysRevLett.123.051101.

L. A. Anchordoqui. Ultra-High-Energy Cosmic Rays. *Phys. Rep.*, 801:1–93, 2019. doi: 10.1016/j.physrep.2019.01.002.

L. A. Anchordoqui and J. F. Soriano. Evidence for UHECR origin in starburst galaxies. In *36th International Cosmic Ray Conference (ICRC 2019) Madison, Wisconsin, USA, July 24-August 1, 2019*, 2019.

L. A. Anchordoqui, J. F. Beacom, H. Goldberg, S. Palomares-Ruiz, and T. J. Weiler. TeV γ^- rays and neutrinos from photo-disintegration of nuclei in Cygnus OB2. *Phys. Rev. D*, 75: 063001, 2007. doi: 10.1103/PhysRevD.75.063001.

L. A. Anchordoqui, D. Hooper, S. Sarkar, and A. M. Taylor. High energy neutrinos from astrophysical accelerators of cosmic ray nuclei. *Astroparticle Physics*, 29(1):1–13, feb 2008. ISSN 09276505. doi: 10.1016/j.astropartphys.2007.10.006. URL https://www.sciencedirect.com/science/article/pii/S0927650507001491?via{%}3Dihub.

M. Anghinolfi, V. Lucherini, P. Rossi, N. Bianchi, et al. Behavior of the Be and C total photonuclear cross section in the nucleon resonance region. *Physical Review C*, 47(3):R922–R925, mar 1993. ISSN 0556-2813. doi: 10.1103/PhysRevC.47.R922. URL https://link.aps.org/doi/10.1103/PhysRevC.47.R922.

M. Arnould and S. Goriely. Astronuclear Physics: A tale of the atomic nuclei in the skies, 2020. ISSN 01466410.

G. Audi, F. G. Kondev, M. Wang, W. Huang, and S. Naimi. The NUBASE2016 evaluation of nuclear properties. *Chinese Physics C*, 41(3):030001, mar 2017. ISSN 1674-1137. doi: 10.1088/1674-1137/41/3/030001. URL http://stacks.iop.org/1674-1137/41/i=3/a=030001?key=crossref.05045a4e9903d0710551e7df47cdd312.

P. Auger, P. Ehrenfest, R. Maze, J. Daudin, and A. F. Robley. Extensive cosmic ray showers. *Rev. Mod. Phys.*, 11:288–291, 1939. doi: 10.1103/RevModPhys.11.288.

P. Baerwald, M. Bustamante, and W. Winter. UHECR escape mechanisms for protons and neutrons from GRBs, and the cosmic ray-neutrino connection. *Astrophys. J.*, 768:186, 2013. doi: 10.1088/0004-637X/768/2/186.

C. Baixeras, D. Bastieri, C. Bigongiari, et al. Commissioning and first tests of the MAGIC telescope. In *Nuclear Instruments and Methods in Physics Research, Section A: Accelerators, Spectrometers, Detectors and Associated Equipment*, volume 518, pages 188–192. North-Holland, feb 2004. doi: 10.1016/j.nima.2003.10.057. URL https://www.sciencedirect.com/science/article/pii/S0168900203027694?via{%}3Dihub.

T. W. Baumgarte, S. L. Shapiro, and M. Shibata. On the Maximum Mass of Differentially Rotating Neutron Stars. *The Astrophysical Journal*, 528(1):L29–L32, 2000. ISSN 0004637X. doi: 10.1086/312425.

A. Bauswein, S. Goriely, and H. T. Janka. Systematics of dynamical mass ejection, nucleosynthesis, and radioactively powered electromagnetic signals from neutron-star mergers. *Astrophysical Journal*, 773(1), 2013. ISSN 15384357. doi: 10.1088/0004-637X/773/1/78.

J. Bellido. Depth of maximum of air-shower profiles at the Pierre Auger Observatory: Measurements above $10^{17.2}$ eV and Composition Implications. In *Proceedings of the 35th International Cosmic Ray Conference*, page 506. POS, 2017a.

J. Bellido. Depth of maximum of air-shower profiles at the Pierre Auger Observatory: Measurements above 1017.2 eV and composition implications. *Proceedings of Science*, pages 0–7, 2017b. ISSN 18248039. doi: 10.22323/1.301.0506.

P. Beniamini, M. Petropoulou, R. B. Duran, and D. Giannios. A lesson from GW170817: Most neutron star mergers result in tightly collimated successful GRB jets. *Monthly Notices of the Royal Astronomical Society*, 483(1):840–851, 2019. ISSN 13652966. doi: 10.1093/mnras/sty3093.

V. Berezinsky, A. Gazizov, and S. Grigorieva. On astrophysical solution to ultrahigh energy cosmic rays. *Physical Review D*, 74(4):043005, aug 2006a. ISSN 1550-7998. doi: 10.1103/PhysRevD.74.043005. URL https://link.aps.org/doi/10.1103/PhysRevD.74.043005.

V. Berezinsky, A. Z. Gazizov, and S. I. Grigorieva. On astrophysical solution to ultrahigh-energy cosmic rays. *Phys. Rev.*, D74:043005, 2006b. doi: 10.1103/PhysRevD.74.043005.

V. S. Berezinsky and S. I. Grigor'eva. A Bump in the ultrahigh-energy cosmic ray spectrum. *Astron. Astrophys.*, 199:1–12, 1988.

R. Bernabei, A. Incicchitti, M. Mattioli, P. Picozza, D. Prosperi, L. Casano, S. D'Angelo, M. P. De Pascale, C. Schaerf, G. Giordano, G. Matone, S. Frullani, and B. Girolami. Total Cross Section for Deuteron Photodisintegration between 15 and 75 MeV. *Physical Review Letters*, 57(13):1542–1545, sep 1986. ISSN 0031-9007. doi: 10.1103/PhysRevLett.57.1542. URL https://link.aps.org/doi/10.1103/PhysRevLett.57.1542.

H. Bethe and W. Heitler. On the Stopping of fast particles and on the creation of positive electrons. *Proc. Roy. Soc. Lond.*, A146:83–112, 1934. doi: 10.1098/rspa.1934.0140.

N. Bianchi, V. Muccifora, et al. Absolute measurement of the total photoabsorption cross section for carbon in the nucleon resonance region. *Physics Letters B*, 309(1):5 – 9, 1993. ISSN 0370-2693. doi: https://doi.org/10.1016/0370-2693(93)91494-8. URL http://www.sciencedirect.com/science/article/pii/0370269393914948.

N. Bianchi, V. Muccifora, E. De Sanctis, A. Fantoni, P. Levi Sandri, E. Polli, A. R. Reolon, P. Rossi, M. Anghinolfi, P. Corvisiero, M. Ripani, M. Sanzone, M. Taiuti, and A. Zucchiatti. Total hadronic photoabsorption cross section on nuclei in the nucleon resonance region. *Physical Review C*, 54(4):1688–1699, oct 1996. ISSN 0556-2813. doi: 10.1103/PhysRevC.54.1688. URL https://link.aps.org/doi/10.1103/PhysRevC.54.1688.

N. Bianchi, E. De Sanctis, M. Mirazita, and V. Muccifora. Shadowing in nuclear photoabsorption above the resonance region. *Phys. Rev. C*, 60:064617, Nov 1999. doi: 10.1103/PhysRevC.60.064617. URL https://link.aps.org/doi/10.1103/PhysRevC.60.064617.

D. Biehl, D. Boncioli, A. Fedynitch, and W. Winter. Cosmic ray and neutrino emission from gamma-ray bursts with a nuclear cascade. *Astronomy & Astrophysics*, 611(A101), 2018a. doi: 10.1051/0004-6361/201731337. URL https://doi.org/10.1051/0004-6361/201731337.

D. Biehl, D. Boncioli, A. Fedynitch, and W. Winter. Cosmic-Ray and Neutrino Emission from Gamma-Ray Bursts with a Nuclear Cascade. *Astron. Astrophys.*, 611:A101, 2018b. doi: 10.1051/0004-6361/201731337.

D. Biehl, D. Boncioli, C. Lunardini, and W. Winter. Tidally disrupted stars as a possible origin of both cosmic rays and neutrinos at the highest energies. *Scientific Reports*, 8(1):10828, 2018c. ISSN 2045-2322. doi: 10.1038/s41598-018-29022-4. URL https://doi.org/10.1038/s41598-018-29022-4.

D. Biehl, D. Boncioli, C. Lunardini, and W. Winter. Tidally disrupted stars as a possible origin of both cosmic rays and neutrinos at the highest energies. *Sci. Rep.*, 8(1):10828, 2018d. doi: 10.1038/s41598-018-29022-4.

D. Bird et al. Detection of a cosmic ray with measured energy well beyond the expected spectral cutoff due to cosmic microwave radiation. *Astrophys. J.*, 441:144–150, 1995. doi: 10.1086/175344.

P. Blasi. The Origin of Galactic Cosmic Rays. *Astron. Astrophys. Rev.*, 21:70, 2013. doi: 10.1007/s00159-013-0070-7.

P. Blasi, R. I. Epstein, and A. V. Olinto. Ultrahigh-energy cosmic rays from young neutron star winds. *Astrophys. J.*, 533:L123, 2000. doi: 10.1086/312626.

F. Bloch, J. Ahrens, J. R. Annand, R. Beck, et al. Double pion photoproduction off 40 Ca. *European Physical Journal A*, 32(2):219–228, may 2007. ISSN 14346001. doi: 10.1140/epja/i2006-10383-2. URL http://link.springer.com/10.1140/epja/i2006-10383-2.

E. Bloom. Determination of the total photon - proton cross-section from high-energy inelastic electron scattering. Technical report, SLAC, 1969. URL https://www-public.slac.stanford.edu/sciDoc/docMeta.aspx?slacPubNumber=SLAC-PUB-0653.

G. R. Blumenthal. Energy loss of high-energy cosmic rays in pair-producing collisions with ambient photons. *Phys. Rev.*, D1:1596–1602, 1970. doi: 10.1103/PhysRevD.1.1596.

D. Boncioli, A. Fedynitch, and W. Winter. Nuclear Physics Meets the Sources of the Ultra-High Energy Cosmic Rays. *Sci. Rep.*, 7(1):4882, 2017. doi: 10.1038/s41598-017-05120-7.

D. Boncioli, D. Biehl, and W. Winter. On the Common Origin of Cosmic Rays across the Ankle and Diffuse Neutrinos at the Highest Energies from Low-luminosity Gamma-Ray Bursts. *Astrophys. J.*, 872(1):110, Feb. 2019. doi: 10.3847/1538-4357/aafda7.

A. M. Brown, C. Bœ hm, J. Graham, T. Lacroix, P. Chadwick, and J. Silk. Discovery of a new extragalactic population of energetic particles. *Phys. Rev. D*, 95(6):063018, 2017. doi: 10.1103/PhysRevD.95.063018.

O. Buss, T. Gaitanos, K. Gallmeister, H. van Hees, M. Kaskulov, O. Lalakulich, A. Larionov, T. Leitner, J. Weil, and U. Mosel. Transport-theoretical description of nuclear reactions. *Physics Reports*, 512(1–2):1 – 124, 2012. ISSN 0370-1573. doi: http://dx.doi.org/10.1016/j.physrep.2011.12.001. URL http://www.sciencedirect.com/science/article/pii/S0370157311003619.

D. O. Caldwell, V. B. Elings, W. P. Hesse, R. J. Morrison, F. V. Murphy, B. W. Worster, and D. E. Yount. Total hadronic (γ, p) and (γ, d) cross sections from 4 to 18 GeV. *Physical Review Letters*, 25(9):609–612, aug 1970. ISSN 00319007. doi: 10.1103/PhysRevLett.25.609. URL https://link.aps.org/doi/10.1103/PhysRevLett.25.609.

D. O. Caldwell, J. P. Cumalat, A. M. Eisner, A. Lu, R. J. Morrison, F. V. Murphy, S. J. Yellin, P. J. Davis, M. G. Donnelly, R. M. Egloff, G. J. Luste, J. F. Martin, J. D. Prentice, and T. Nash. Measurement of Shadowing in Photon-Nucleus Total Cross Sections from 20 to 185 GeV. *Physical Review Letters*, 42(9):553–556, feb 1979. ISSN 0031-9007. doi: 10.1103/PhysRevLett.42.553. URL https://link.aps.org/doi/10.1103/PhysRevLett.42.553.

J. Candia, L. N. Epele, and E. Roulet. Cosmic ray photodisintegration and the knee of the spectrum. *Astroparticle Physics*, 17(1):23–33, apr 2002. ISSN 09276505. doi: 10.

1016/S0927-6505(01)00131-1. URL https://www.sciencedirect.com/science/article/pii/S0927650501001311.

J. n. Candia, S. Mollerach, and E. Roulet. Cosmic ray spectrum and anisotropies from the knee to the second knee. *Journal of Cosmology and Astroparticle Physics*, 2003(05):003–003, may 2003. ISSN 1475-7516. doi: 10.1088/1475-7516/2003/05/003. URL https://iopscience.iop.org/article/10.1088/1475-7516/2003/05/003.

D. Caprioli. "Espresso" Acceleration of Ultra-high-energy Cosmic Rays. *Astrophys. J.*, 811(2): L38, 2015. doi: 10.1088/2041-8205/811/2/L38.

M. Chiaberge, A. Capetti, and A. Celotti. The bl lac heart of centaurus a. *Mon. Not. Roy. Astron. Soc.*, 324:L33, 2001. doi: 10.1046/j.1365-8711.2001.04642.x.

G. W. Clark, J. Earl, W. L. Kraushaar, J. Linsley, B. B. Rossi, F. Scherb, and D. W. Scott. Cosmic-ray air showers at sea level. *Phys. Rev.*, 122:637–654, Apr 1961. doi: 10.1103/PhysRev.122.637. URL https://link.aps.org/doi/10.1103/PhysRev.122.637.

A. J. Cole. *Statistical Models for Nuclear Decay: From Evaporation to Vaporization*. Institute of Physics Pub, 2010. ISBN 9781420033472. URL https://inis.iaea.org/search/search.aspx?orig{_}q=RN:32002933.

P. S. Cowperthwaite et al. The Electromagnetic Counterpart of the Binary Neutron Star Merger LIGO/Virgo GW170817. II. UV, Optical, and Near-infrared Light Curves and Comparison to Kilonova Models. *Astrophys. J.*, 848(2):L17, 2017. doi: 10.3847/2041-8213/aa8fc7.

J. Crank and P. Nicolson. A practical method for numerical evaluation of solutions of partial differential equations of the heat-conduction type [reprint of MR0019410 (8,409b)]. *Advances in Computational Mathematics*, 6(1):207–226, Dec. 1996. ISSN 1019-7168 (print), 1572-9044 (electronic). doi: https://doi.org/10.1007/BF02127704. URL http://link.springer.com/article/10.1007/BF02127704. John Crank 80th birthday special issue.

D. De Marco, P. Blasi, and A. V. Olinto. On the Statistical significance of the GZK feature in the spectrum of ultrahigh-energy cosmic rays. *Astropart. Phys.*, 20:53–65, 2003. doi: 10.1016/S0927-6505(03)00148-8.

A. Deppman, S. B. Duarte, G. Silva, O. A. Tavares, S. Anéfalos, J. D. Arruda-Neto, and T. E. Rodrigues. The CRISP package for intermediate- and high-energy photonuclear reactions. *Journal of Physics G: Nuclear and Particle Physics*, 30(12):1991–2002, dec 2004. ISSN 09543899. doi: 10.1088/0954-3899/30/12/016. URL http://stacks.iop.org/0954-3899/30/i=12/a=016?key=crossref.a00c589581bf0fb91300340fbbedebe3.

V. di Napoli and M. L. Terranova. The (γ, 2p 3n) reaction in light nuclei at intermediate energy. *Journal of Inorganic and Nuclear Chemistry*, 36(12):3633–3637, dec 1974. ISSN 00221902. doi: 10.1016/0022-1902(74)80140-5.

V. di Napoli, G. Rosa, F. Salvetti, M. L. Terranova, H. G. de Carvalho, J. B. Martins, and O. A. Tavares. Photodisintegration of light and medium-weight nuclei at intermediate energies-II Photoproduction of 11C and 7Be from 40Ca. *Journal of Inorganic and Nuclear Chemistry*, 38(1):1–5, jan 1976. ISSN 00221902. doi: 10.1016/0022-1902(76)80038-3.

V. di Napoli, F. Salvetti, M. Terranova, H. de Carvalho, J. Martins, and O. Tavares. Photodisintegration of light and medium-weight nuclei at intermediate energies—III: Spallation of vanadium, manganese, iron and cobalt. *Journal of Inorganic and Nuclear Chemistry*, 40(2):175–182, jan 1978. ISSN 0022-1902. doi: 10.1016/0022-1902(78)80106-7. URL https://www.sciencedirect.com/science/article/pii/0022190278801067.

M. Dieterle et al. Photoproduction of -pairs off protons and off neutrons. *European Physical Journal A*, 51(11), 2015. ISSN 1434601X. doi: 10.1140/epja/i2015-15142-8. URL https://link.springer.com/content/pdf/10.1140/epja/i2015-15142-8.

C. L. Doherty, P. Gil-Pons, L. Siess, and J. C. Lattanzio. Super-AGB Stars and their Role as Electron Capture Supernova Progenitors. *Publications of the Astronomical Society of Australia*, 34(May), 2017. ISSN 1323-3580. doi: 10.1017/pasa.2017.52.

A. Dominguez et al. Extragalactic Background Light Inferred from AEGIS Galaxy SED-type Fractions. *Mon. Not. Roy. Astron. Soc.*, 410:2556, 2011. doi: 10.1111/j.1365-2966.2010.17631.x.

M. Dominik, K. Belczynski, C. Fryer, D. E. Holz, E. Berti, T. Bulik, I. Mandel, and R. O'Shaughnessy. Double compact objects. I. the significance of the common envelope on merger rates. *Astrophysical Journal*, 759(1):52, nov 2012. ISSN 15384357. doi: 10.1088/0004-637X/759/1/52. URL https://iopscience.iop.org/article/10.1088/0004-637X/759/1/52.

M. T. Dova, L. N. Epele, and J. D. Swain. Massive relic neutrinos in the galactic halo and the knee in the cosmic ray spectrum, 2001.

M. R. Drout, A. L. Piro, B. J. Shappee, C. D. Kilpatrick, et al. Light curves of the neutron star merger GW170817/SSS17a: Implications for R-process nucleosynthesis. *Science*, 358(6370):1570–1574, 2017. ISSN 10959203. doi: 10.1126/science.aaq0049.

R. Engel. Photoproduction within the two component dual parton model. 1. Amplitudes and cross-sections. *Z. Phys.*, C66:203–214, 1995. doi: 10.1007/BF01496594.

ENSDF. Nuclear data published by the national nuclear data center, brookhaven national laboratory in the form of evaluated nuclear structure data file (ensdf), November 2019. URL https://nndc/bnl.gov/ensarchivals/.

K. Fang, K. Kotera, and A. V. Olinto. Newly-born pulsars as sources of ultrahigh energy cosmic rays. *Astrophys. J.*, 750:118, 2012. doi: 10.1088/0004-637X/750/2/118.

G. R. Farrar and T. Piran. Tidal disruption jets as the source of Ultra-High Energy Cosmic Rays. *arXiv preprint*, 2014.

A. Fassò, A. Ferrari, and P. R. Sala. Total giant resonance photonuclear cross sections for light nuclei. *Proc. SATIF-3, Sendai, Japan*, pages 61–74, 1997.

A. Fassò, A. Ferrari, and P. R. Sala. Photonuclear reactions in fluka: Cross sections and interaction models. *AIP Conference Proceedings*, 769(1):1303–1306, 2005.

E. Fermi. On the Origin of the Cosmic Radiation. *Phys. Rev.*, 75:1169–1174, 1949. doi: 10.1103/PhysRev.75.1169.

E. Fermi. Galactic Magnetic Fields and the Origin of Cosmic Radiation. *Astrophys. J.*, 119:1–6, 1954. doi: 10.1086/145789.

A. Ferrari, P. R. Sala, A. Fasso, and J. Ranft. FLUKA: A multi-particle transport code (Program version 2005). *CERN-2005-010*, 2005.

R. P. R. P. Feynman. *Photon-hadron interactions*. Frontiers in physics. Westview Press, 1972. ISBN 0-8053-2510-7, 0-8053-2511-5 (paperback).

S. Fuji. Note on the Quasi-Deuteron Model lor Nuclear Photo-Disintegration . *Il Nuovo Cimento*, XXV(5), 1962.

S. Gao, M. Pohl, and W. Winter. On the direct correlation between gamma-rays and PeV neutrinos from blazars. *Astrophys. J.*, 843(2):109, 2017. doi: 10.3847/1538-4357/aa7754.

S. Gao, A. Fedynitch, W. Winter, and M. Pohl. Modelling the coincident observation of a high-energy neutrino and a bright blazar flare. *Nat. Astron.*, 3(1):88–92, 2019. doi: 10.1038/s41550-018-0610-1.

J.-J. Geng, B. Zhang, A. Kölligan, R. Kuiper, and Y.-F. Huang. Propagation of a Short GRB Jet in the Ejecta: Jet Launching Delay Time, Jet Structure, and GW170817/GRB 170817A. *The Astrophysical Journal*, 877(2):L40, jun 2019. ISSN 2041-8213. doi: 10.3847/2041-8213/ab224b. URL https://iopscience.iop.org/article/10.3847/2041-8213/ab224b.

R. C. Gilmore, R. S. Somerville, J. R. Primack, and A. Dominguez. Semi-analytic modeling of the EBL and consequences for extragalactic gamma-ray spectra. *Mon. Not. Roy. Astron. Soc.*, 422:3189, 2012. doi: 10.1111/j.1365-2966.2012.20841.x.

S. Goriely and N. Mowlavi. Neutron-capture nucleosynthesis in AGB stars. Technical report, 2000. URL http://www-astro.ulb.ac.be.

R. J. Gould. Neutron-Photon Scattering in the Early Universe. *The Astrophysical Journal*, 417: 12, nov 1993. ISSN 0004-637X. doi: 10.1086/173287.

W. Greiner and J. A. Maruhn. *Nuclear Models*. Springer Berlin Heidelberg, 1996. ISBN 9783642609701.

K. Greisen. End to the cosmic ray spectrum? *Phys. Rev. Lett.*, 16:748–750, 1966. doi: 10.1103/PhysRevLett.16.748.

H. E. S. S. Collaboration et al. Resolving acceleration to very high energies along the jet of Centaurus A. *Nature*, 582(7812):356–359, June 2020. doi: 10.1038/s41586-020-2354-1.

G. Halevi and P. Mösta. r-Process nucleosynthesis from three-dimensional jet-driven core-collapse supernovae with magnetic misalignments. *Monthly Notices of the Royal Astronomical Society*, 477(2):2366–2375, 2018. ISSN 13652966. doi: 10.1093/mnras/sty797.

J. Heinze, D. Boncioli, M. Bustamante, and W. Winter. Cosmogenic Neutrinos Challenge the Cosmic Ray Proton Dip Model. *Astrophys. J.*, 825(2):122, 2016. doi: 10.3847/0004-637X/825/2/122.

J. Heinze, A. Fedynitch, D. Boncioli, and W. Winter. A new view on Auger data and cosmogenic neutrinos in light of different nuclear disintegration and air-shower models. *Astrophys. J.*, 873 (1):88, 2019. doi: 10.3847/1538-4357/ab05ce.

C. Heiter, D. Kuempel, D. Walz, and M. Erdmann. Production and propagation of ultra-high energy photons using CRPropa 3. *Astroparticle Physics*, 102:39–50, 2018. ISSN 0927-6505. doi: https://doi.org/10.1016/j.astropartphys.2018.05.003. URL http://www.sciencedirect.com/science/article/pii/S0927650518300069.

V. F. Hess. Über Beobachtungen der durchdringenden Strahlung bei sieben Freiballonfahrten. *Phys. Z.*, 13:1084–1091, 1912.

A. M. Hillas. The Origin of Ultrahigh-Energy Cosmic Rays. *Ann. Rev. Astron. Astrophys.*, 22: 425–444, 1984. doi: 10.1146/annurev.aa.22.090184.002233.

G. Hinshaw, D. Larson, E. Komatsu, et al. Nine-year wilkinson microwave anisotropy probe (WMAP) observations: Cosmological parameter results. *Astrophysical Journal, Supplement Series*, 208(2), 2013. ISSN 00670049. doi: 10.1088/0067-0049/208/2/19.

J. Hinton. The status of the HESS project. *New Astronomy Reviews*, 48(5-6):331–337, Apr 2004. ISSN 1387-6473. doi: 10.1016/j.newar.2003.12.004. URL http://dx.doi.org/10.1016/j.newar.2003.12.004.

G. Ho ohler, S. Fl ugge, F. Hund, and E. A. Niekisch. *Electron and Photon Interactions at High Energies : Invited Papers Presented at the International Symposium Hamburg, June 8-12, 1965*. Springer Berlin Heidelberg, 1965. ISBN 9783540371427.

D. Hooper, S. Sarkar, and A. M. Taylor. Intergalactic propagation of ultrahigh energy cosmic ray nuclei: An analytic approach. *Physical Review D - Particles, Fields, Gravitation and Cosmology*, 77(10):1–7, 2008. ISSN 15507998. doi: 10.1103/PhysRevD.77.103007.

W. J. Huang, G. Audi, M. Wang, F. G. Kondev, S. Naimi, and X. Xu. The AME2016 atomic mass evaluation (I). Evaluation of input data; And adjustment procedures. *Chinese Physics C*, 41(3):030002, mar 2017. ISSN 16741137. doi: 10.1088/1674-1137/41/3/030002. URL http://stacks.iop.org/1674-1137/41/i=3/a=030002?key=crossref.c5ac715502743b64b763cf8c555c73d2.

S. Hummer, M. Ruger, F. Spanier, and W. Winter. Simplified models for photohadronic interactions in cosmic accelerators. *Astrophys. J.*, 721:630–652, 2010. doi: 10.1088/0004-637X/721/1/630.

G. D. Ihongo and C. H. T. Wang. The effects of solar wind on galactic cosmic ray flux at Earth. *Astrophysics and Space Science*, 361:44, Jan. 2016. doi: 10.1007/s10509-015-2628-5.

F. Israel. Centaurus a - ngc 5128. *Astron. Astrophys. Rev.*, 8:237, 1998. doi: 10.1007/s001590050011.

J. C. Joshi and N. Gupta. Testing Hadronic Models of Gamma Ray Production at the Core of Cen A. *Phys. Rev. D*, 87(2):023002, 2013. doi: 10.1103/PhysRevD.87.023002.

A. B. Kaidalov. Regge Poles in QCD and Heavy-Ion Collisions. In *QCD Perspectives on Hot and Dense Matter*, pages 159–205. Springer Netherlands, 2002. doi: 10.1007/978-94-010-0267-7_5.

O. E. Kalashev and E. Kido. Simulations of Ultra High Energy Cosmic Rays propagation. *J. Exp. Theor. Phys.*, 120(5):790–797, 2015. doi: 10.1134/S1063776115040056.

K.-H. Kampert and M. Unger. Measurements of the Cosmic Ray Composition with Air Shower Experiments. *Astropart. Phys.*, 35:660–678, 2012. doi: 10.1016/j.astropartphys.2012.02.004.

K.-H. Kampert, A. A. Watson, and A. A. Watson. Extensive Air Showers and Ultra High-Energy Cosmic Rays: A Historical Review. *Eur. Phys. J.*, H37:359–412, 2012. doi: 10.1140/epjh/e2012-30013-x.

K.-H. Kampert, J. Kulbartz, L. Maccione, N. Nierstenhoefer, P. Schiffer, G. Sigl, and A. R. van Vliet. CRPropa 2.0 – a Public Framework for Propagating High Energy Nuclei, Secondary Gamma Rays and Neutrinos. *Astropart. Phys.*, 42:41–51, 2013. doi: 10.1016/j.astropartphys.2012.12.001.

A. I. Karakas and J. C. Lattanzio. The Dawes Review 2: Nucleosynthesis and stellar yields of low-and intermediate-mass single stars. *Publications of the Astronomical Society of Australia*, 31(12), 2014. ISSN 14486083. doi: 10.1017/pasa.2014.21.

J. Kataoka et al. A Study of high-energy emission from the TeV blazar Mrk 501 during multi-wavelength observations in 1996. *Astrophys. J.*, 514:138, 1999. doi: 10.1086/306918.

D. Kazanas and A. Nicolaidis. Cosmic Ray "Knee": A Herald of New Physics?, 2001.

D. Kazanas and A. Nicolaidis. Cosmic Rays and Large Extra Dimensions. *General Relativity and Gravitation*, 35(6):1117–1123, 2003. ISSN 00017701. doi: 10.1023/A:1024077103557.

E. Kirby. The Elemental Abundance Distributions of Milky Way Satellite Galaxies. *EAS Publications Series*, 48:19–25, nov 2011. ISSN 1633-4760. doi: 10.1051/eas/1148003. URL http://arxiv.org/abs/1011.1530http://dx.doi.org/10.1051/eas/1148003.

K. Kobayakawa, Y. S. Honda, and T. Samura. Acceleration by oblique shocks at supernova remnants and cosmic ray spectra around the knee region. *Phys. Rev. D*, 66:083004, Oct 2002. doi: 10.1103/PhysRevD.66.083004. URL https://link.aps.org/doi/10.1103/PhysRevD.66.083004.

J. H. Koch, E. J. Moniz, and N. Ohtsuka. Nuclear photoabsorption and Compton scattering at intermediate energy. *Annals of Physics*, 154(1):99–160, 1984. ISSN 0003-4916. doi: https:

//doi.org/10.1016/0003-4916(84)90141-6. URL http://www.sciencedirect.com/science/article/pii/0003491684901416.

W. Kolhorster, I. Matthes, and E. Weber. Gekoppelte Höhenstrahlen. *Naturwissenschaften*, 26: 576, 1938.

A. J. Koning, M. C. Duijvestijn, and S. Hilaire. Talys: Comprehensive nuclear reaction modeling, 5 2005. ISSN 0094-243X. URL https://www.osti.gov/biblio/20722384. Code version released in 2015.

A. J. Koning, S. Hilaire, and M. C. Duijvestijn. TALYS 1.0. In *Proceedings, International Conference on Nuclear Data for Science and Tecnology*, pages 211–214, 2007.

P. Kroupa, C. A. Tout, and G. Gilmore. The Distribution of low mass stars in the galactic disc. *Mon. Not. Roy. Astron. Soc.*, 262:545, 1993.

B. Krusche. Photoproduction of mesons off nuclei, sep 2011. ISSN 19516355. URL http://www.springerlink.com/index/10.1140/epjst/e2011-01491-2.

B. Krusche, J. Lehr, J. Ahrens, et al. Photoproduction of πmesons from nuclei. *The European Physical Journal A*, 22(2):277–291, nov 2004a. ISSN 1434-6001. doi: 10.1140/epja/i2004-10033-9. URL http://link.springer.com/10.1140/epja/i2004-10033-9.

B. Krusche, J. Lehr, F. Bloch, M. Kotulla, V. Metag, U. Mosel, and S. Schadmand. Surface and volume effects in the photoabsorption of nuclei. *European Physical Journal A*, 22(3):347–351, dec 2004b. ISSN 14346001. doi: 10.1140/epja/i2004-10098-4. URL http://link.springer.com/10.1140/epja/i2004-10098-4.

E. Kundu and N. Gupta. Photo-Disintegration of Heavy Nuclei at the Core of Cen A. *JCAP*, 04:030, 2014. doi: 10.1088/1475-7516/2014/04/030.

B. C. Lacki and T. A. Thompson. The Physics of the FIR-Radio Correlation: II. Synchrotron Emission as a Star-Formation Tracer in High-Redshift Galaxies. *Astrophys. J.*, 717:196–208, 2010. doi: 10.1088/0004-637X/717/1/196.

J. H. Lacy, C. H. Townes, and D. J. Hollenbach. The nature of the central parsec of the Galaxy. *Astrophys. J.*, 262:120–134, Nov. 1982. doi: 10.1086/160402.

K. Langanke, G. Martinez-Pinedo, and A. Sieverding. Neutrino nucleosynthesis: An overview. *arXiv e-prints*, art. arXiv:1901.03741, Jan. 2019.

T.-S. H. Lee and R. P. Redwine. P ION -N UCLEUS I NTERACTIONS. *Annual Review of Nuclear and Particle Science*, 52(1):23–63, dec 2002. ISSN 0163-8998. doi: 10.1146/annurev.nucl.52.050102.090713. URL http://www.annualreviews.org/doi/10.1146/annurev.nucl.52.050102.090713.

J. S. Levinger and H. A. Bethe. Dipole transitions in the nuclear photo-effect. *Physical Review*, 78(2):115–129, 1950. ISSN 0031899X. doi: 10.1103/PhysRev.78.115.

J. Linsley. Evidence for a primary cosmic-ray particle with energy 10^{20} ev. *Phys. Rev. Lett.*, 10:146–148, Feb 1963. doi: 10.1103/PhysRevLett.10.146. URL https://link.aps.org/doi/10.1103/PhysRevLett.10.146.

J. Linsley and A. A. Watson. Validity of scaling to 10^{20} ev and high-energy cosmic-ray composition. *Phys. Rev. Lett.*, 46:459–463, Feb 1981. doi: 10.1103/PhysRevLett.46.459. URL https://link.aps.org/doi/10.1103/PhysRevLett.46.459.

K. Lodders. Solar System Abundances of the Elements. In A. Goswami and B. E. Reddy, editors, *Principles and Perspectives in Cosmochemistry*, pages 379–417, Berlin, Heidelberg, 2010. Springer Berlin Heidelberg. ISBN 978-3-642-10352-0.

M. MacCormick, J. Habermann, J. Ahrens, et al. Total photoabsorption cross section for 4 He from 200 to 800 MeV. *Physical Review C*, 55(3):1033–1038, mar 1997. ISSN 0556-2813. doi: 10.1103/PhysRevC.55.1033. URL https://link.aps.org/doi/10.1103/PhysRevC.55.1033.

A. Mastichiadis, I. Florou, E. Kefala, S. S. Boula, and M. Petropoulou. A roadmap to hadronic supercriticalities: a comprehensive study of the parameter space for high-energy astrophysical sources. *Monthly Notices of the Royal Astronomical Society*, 495(2):2458–2474, 05 2020. ISSN 0035-8711. doi: 10.1093/mnras/staa1308. URL https://doi.org/10.1093/mnras/staa1308.

J. Matthews. Highlights from the Telescope Array Experiment. *PoS*, ICRC2017:1096, 2018. doi: 10.22323/1.301.1096.

T. Mertens, I. Jaegle, et al. Photoproduction of η-mesons off nuclei for Eγ 2.2 GeV. *European Physical Journal A*, 38(2):195–207, nov 2008. ISSN 14346001. doi: 10.1140/epja/i2007-10667-y. URL http://link.springer.com/10.1140/epja/i2007-10667-y.

A. Mizuta and K. Ioka. Opening angles of collapsar jets. *The Astrophysical Journal*, 777(2):162, oct 2013. ISSN 0004-637X. doi: 10.1088/0004-637X/777/2/162. URL https://iopscience.iop.org/article/10.1088/0004-637X/777/2/162.

L. Morejon. AstroPhoMes: Photomeson models for UHECR interactions with photons, 2019b. URL https://doi.org/10.5281/zenodo.2600177.

L. Morejon, A. Fedynitch, D. Boncioli, D. Biehl, and W. Winter. Improved photomeson model for interactions of cosmic ray nuclei. *Journal of Cosmology and Astroparticle Physics*, 2019 (11):007–007, 2019a. ISSN 1475-7516. doi: 10.1088/1475-7516/2019/11/007. URL https://iopscience.iop.org/article/10.1088/1475-7516/2019/11/007.

L. Morejon, J. Heinze, A. Fedynitch, and W. Winter. (tentative author order) Extragalactic propagation of super-heavy UHECR nuclei (working title). in development.

A. Mucke and R. Protheroe. A Proton synchrotron blazar model for flaring in Markarian 501. *Astropart. Phys.*, 15:121–136, 2001. doi: 10.1016/S0927-6505(00)00141-9.

A. Mucke, R. Engel, J. P. Rachen, R. J. Protheroe, and T. Stanev. SOPHIA: Monte Carlo simulations of photohadronic processes in astrophysics. *Comput. Phys. Commun.*, 124:290–314, 2000. doi: 10.1016/S0010-4655(99)00446-4.

K. Murase and J. F. Beacom. Very-high-energy gamma-ray signal from nuclear photodisintegration as a probe of extragalactic sources of ultrahigh-energy nuclei. *Phys. Rev. D*, 82:043008, Aug 2010. doi: 10.1103/PhysRevD.82.043008. URL https://link.aps.org/doi/10.1103/PhysRevD.82.043008.

K. Murase, K. Ioka, S. Nagataki, and T. Nakamura. High Energy Neutrinos and Cosmic-Rays from Low-Luminosity Gamma-Ray Bursts? *Astrophys. J.*, 651:L5–L8, 2006. doi: 10.1086/509323.

K. Murase, K. Ioka, S. Nagataki, and T. Nakamura. High-energy cosmic-ray nuclei from high- and low-luminosity gamma-ray bursts and implications for multimessenger astronomy. *Phys. Rev. D*, 78:023005, Jul 2008. doi: 10.1103/PhysRevD.78.023005. URL https://link.aps.org/doi/10.1103/PhysRevD.78.023005.

K. Murase, C. D. Dermer, H. Takami, and G. Migliori. Blazars as Ultra-High-Energy Cosmic-Ray sources: Implications for TeV gamma-ray observations. *The Astrophysical Journal*, 749(1):63, apr 2012. ISSN 0004-637X. doi: 10.1088/0004-637X/749/1/63. URL https://iopscience.iop.org/article/10.1088/0004-637X/749/1/63.

K. Murase, Y. Inoue, and C. D. Dermer. Diffuse Neutrino Intensity from the Inner Jets of Active Galactic Nuclei: Impacts of External Photon Fields and the Blazar Sequence. *Phys. Rev.*, D90(2):023007, 2014. doi: 10.1103/PhysRevD.90.023007.

A. Murguia-Berthier, G. Montes, E. Ramirez-Ruiz, F. De Colle, and W. H. Lee. Necessary conditions for short gamma-ray burst production in binary neutron star mergers. *The Astrophysical Journal*, 788(1):L8, may 2014. ISSN 2041-8205. doi: 10.1088/2041-8205/788/1/L8. URL https://iopscience.iop.org/article/10.1088/2041-8205/788/1/L8.

M. S. Muzio, M. Unger, and G. R. Farrar. Progress towards characterizing ultrahigh energy cosmic ray sources. *Physical Review D*, 100(10):103008, nov 2019. ISSN 24700029. doi: 10.1103/PhysRevD.100.103008. URL https://link.aps.org/doi/10.1103/PhysRevD.100.103008.

H. Nagakura, K. Hotokezaka, Y. Sekiguchi, M. Shibata, and K. Ioka. Jet collimation in the ejecta of double neutron star mergers: A new canonical picture of short gamma-ray bursts. *The Astrophysical Journal*, 784(2):L28, mar 2014. ISSN 2041-8205. doi: 10.1088/2041-8205/784/2/L28. URL https://iopscience.iop.org/article/10.1088/2041-8205/784/2/L28.

A. Nagl, V. Devanathan, and H. Überall. *Nuclear Pion Photoproduction*, volume 120 of *Springer Tracts in Modern Physics*. Springer Berlin Heidelberg, Berlin, Heidelberg, 1991. ISBN 978-3-540-50671-3. doi: 10.1007/BFb0048454. URL http://link.springer.com/10.1007/BFb0048454.

N. Nishimura, T. Takiwaki, and F. K. Thielemann. The r-process nucleosynthesis in the various jet-like explosions of magnetorotational core-collapse supernovae. *Astrophysical Journal*, 810 (2):109, 2015. ISSN 15384357. doi: 10.1088/0004-637X/810/2/109. URL http://dx.doi.org/10.1088/0004-637X/810/2/109.

A. C. Odian, P. C. Stein, A. Wattenberg, B. T. Feld, and R. Weinstein. Photoejection of high-energy nucleons from nuclei and the quasi-deuteron model. I. Cross sections and angular distributions. *Physical Review*, 102(3):837–843, 1956. ISSN 0031899X. doi: 10.1103/PhysRev.102.837.

D. E. Osterbrock. *Astrophysics of gaseous nebulae and active galactic nuclei*. University Science Books, 1989.

N. Otuka et al. Towards a More Complete and Accurate Experimental Nuclear Reaction Data Library (EXFOR): International Collaboration Between Nuclear Reaction Data Centres (NRDC). *Nucl. Data Sheets*, 120:272–276, 2014. doi: 10.1016/j.nds.2014.07.065.

D. Pacini. La radiazione penetrante alla superficie ed in seno alle acque. *Il Nuovo Cimento (1911-1923)*, 3(1):93–100, 1912. ISSN 1827-6121. doi: 10.1007/BF02957440. URL https://doi.org/10.1007/BF02957440https://arxiv.org/abs/1808.02927.

A. Perego, S. Rosswog, R. M. Cabezón, O. Korobkin, R. Käppeli, A. Arcones, and M. Liebendörfer. Neutrino-driven winds from neutron star merger remnants. *Monthly Notices of the Royal Astronomical Society*, 443(4):3134–3156, 2014. ISSN 13652966. doi: 10.1093/mnras/stu1352.

M. Petropoulou, E. Lefa, S. Dimitrakoudis, and A. Mastichiadis. One-zone synchrotron self-Compton model for the core emission of Centaurus A revisited. *Astron. Astrophys.*, 562:A12, 2014. doi: 10.1051/0004-6361/201322833.

E. Pian, P. D'Avanzo, S. Benetti, et al. Spectroscopic identification of r-process nucleosynthesis in a double neutron-star merger. *Nature*, 551(7678):67–70, 2017. ISSN 14764687. doi: 10.1038/nature24298. URL http://dx.doi.org/10.1038/nature24298.

V. A. Plujko, O. M. Gorbachenko, V. M. Bondar, and R. Capote. Renewed database of GDR parameters for atomic nuclei. *Journal of the Korean Physical Society*, 59(23):1514–1517, aug 2011. ISSN 03744884. doi: 10.3938/jkps.59.1514.

J. L. Puget, F. W. Stecker, and J. H. Bredekamp. Photonuclear Interactions of Ultrahigh-Energy Cosmic Rays and their Astrophysical Consequences. *Astrophys. J.*, 205:638–654, 1976. doi: 10.1086/154321.

J. P. Rachen. *Interaction Processes and Statistical Properties of the Propagation of Cosmic Rays in Photon Backgrounds*. PhD thesis, MPIfR Bonn, Germany, 1996.

T. Rauscher, A. Heger, R. D. Hoffman, and S. E. Woosley. Nucleosynthesis in Massive Stars with Improved Nuclear and Stellar Physics. *The Astrophysical Journal*, 576(1):323–348, sep 2002. ISSN 0004-637X. doi: 10.1086/341728.

M. J. Rees. Tidal disruption of stars by black holes of $10^6 - 10^8$ solar masses in nearby galaxies. *Nature*, 333(6173):523–528, 1988. ISSN 00280836. doi: 10.1038/333523a0. URL https://www.nature.com/articles/333523a0.

E. Regener. Der Energiestrom der Ultrastrahlung. *Zeitschrift für Physik*, 80(9):666–669, 1933. ISSN 0044-3328. doi: 10.1007/BF01335703. URL https://doi.org/10.1007/BF01335703.

RIPL-2. *Handbook for Calculations of Nuclear Reaction Data, RIPL-2*. Number 1506 in TECDOC Series. INTERNATIONAL ATOMIC ENERGY AGENCY, Vienna, 2006. ISBN 92-0-105206-5. URL https://www.iaea.org/publications/7129/handbook-for-calculations-of-nuclear-reaction-data-ripl-2.

L. F. Roberts, D. Kasen, W. H. Lee, and E. Ramirez-Ruiz. Electromagnetic transients powered by nuclear decay in the tidal tails of coalescing compact binaries. *Astrophysical Journal Letters*, 736(1):1–5, 2011. ISSN 20418205. doi: 10.1088/2041-8205/736/1/L21.

X. Rodrigues, A. Fedynitch, S. Gao, D. Boncioli, and W. Winter. Neutrinos and Ultra-High-Energy Cosmic-Ray Nuclei from Blazars. *Astrophys. J.*, 854(1):54, 2018. doi: 10.3847/1538-4357/aaa7ee.

X. Rodrigues, S. Gao, A. Fedynitch, A. Palladino, and W. Winter. Leptohadronic Blazar Models Applied to the 2014–2015 Flare of TXS 0506+056. *Astrophys. J.*, 874(2):L29, 2019. doi: 10.3847/2041-8213/ab1267.

X. Rodrigues, L. Morejon, A. Rudolph, S. Gao, and W. Winter. (tentative author order) Nuclear gamma-ray emission from Centaurus A revisited with numerical models (working title). in development.

D. Santonocito and Y. Blumenfeld. Evolution of the giant dipole resonance properties with excitation energy. In *European Physical Journal A*, volume 30, pages 183–202. Società Italiana di Fisica, oct 2006. doi: 10.1140/epja/i2006-10116-7. URL http://link.springer.com/10.1140/epja/i2006-10116-7.

D. Schildknecht. Vector meson dominance. In *Acta Physica Polonica B*, volume 37, pages 595–607, nov 2006. doi: 10.1007/3-540-52981-0_1. URL https://arxiv.org/abs/hep-ph/0511090.

N. Senno, P. Mészáros, K. Murase, P. Baerwald, and M. J. Rees. Extragalactic star-forming galaxies with hypernovae and supernovae as high-energy neutrino and gamma-ray sources: the case of the 10 TeV neutrino data. *Astrophys. J.*, 806(1):24, 2015. doi: 10.1088/0004-637X/806/1/24.

L. J. Shingles, C. L. Doherty, A. I. Karakas, R. J. Stancliffe, J. C. Lattanzio, and M. Lugaro. Evolution and nucleosynthesis of helium-rich asymptotic giant branch models. *Monthly Notices of the Royal Astronomical Society*, 452(3):2804–2821, 2015. ISSN 13652966. doi: 10.1093/mnras/stv1489.

D. M. Siegel, R. Ciolfi, and L. Rezzolla. Magnetically driven winds from differentially rotating neutron stars and x-ray afterglows of short gamma-ray bursts. *Astrophysical Journal Letters*, 785(1), 2014. ISSN 20418213. doi: 10.1088/2041-8205/785/1/L6.

D. M. Siegel, J. Barnes, and B. D. Metzger. Collapsars as a major source of r-process elements. *Nature*, 569(7755):241–244, 2019. ISSN 14764687. doi: 10.1038/s41586-019-1136-0. URL http://dx.doi.org/10.1038/s41586-019-1136-0.

F. W. Stecker. Photodisintegration of ultrahigh-energy cosmic rays by the universal radiation field. *Physical Review*, 180(5):1264–1266, apr 1969. ISSN 0031899X. doi: 10.1103/PhysRev.180.1264. URL https://link.aps.org/doi/10.1103/PhysRev.180.1264.

F. W. Stecker, C. Done, M. H. Salamon, and P. Sommers. High-energy neutrinos from active galactic nuclei. *Phys. Rev. Lett.*, 66:2697–2700, 1991. doi: 10.1103/PhysRevLett.66.2697,10.1103/PhysRevLett.69.2738. [Erratum: Phys. Rev. Lett.69,2738(1992)].

A. D. Supanitsky. Implications of gamma-ray observations on proton models of ultrahigh energy cosmic rays. *Phys. Rev.*, D94(6):063002, 2016. doi: 10.1103/PhysRevD.94.063002.

W. F. Swann. A mechanism of acquirement of cosmic-ray energies by electrons. *Physical Review*, 43(4):217–220, 1933. ISSN 0031899X. doi: 10.1103/PhysRev.43.217.

N. R. Tanvir, A. J. Levan, A. S. Fruchter, J. Hjorth, K. Wiersema, R. Tunnicliffe, and A. de Ugarte Postigo. A "kilonova" associated with short-duration gamma-ray burst 130603B. *Nature*, 500:547, 2013. doi: 10.1038/nature12505.

M. L. Terranova and O. A. P. Tavares. Total nuclear photoabsorption cross-section in the range 0.2-GeV - 1-GeV for nuclei throughout the periodic table. *Phys. Scripta*, 49:267–279, 1994. doi: 10.1088/0031-8949/49/3/004.

M. L. Terranova, D. A. De Lima, and J. D. Pinheiro Filho. Evaluation of total nuclear photoabsorption cross-sections by the modified quasi-deuteron model. *Epl*, 9(6):523–526, 1989. ISSN 12864854. doi: 10.1209/0295-5075/9/6/005.

The A2 Collaboration. Photoproduction of $\eta\pi$ pairs off nucleons and deuterons. *European Physical Journal A*, 52(9), 2016. ISSN 1434601X. doi: 10.1140/epja/i2016-16272-1. URL https://link.springer.com/content/pdf/10.1140/epja/i2016-16272-1.

H. Tokuno et al. New air fluorescence detectors employed in the Telescope Array experiment. *Nucl. Instrum. Meth.*, A676:54–65, 2012. doi: 10.1016/j.nima.2012.02.044.

R. Ulrich, J. Blümer, R. Engel, F. Schüssler, and M. Unger. On the measurement of the proton-air cross section using air shower data. *New Journal of Physics*, 11, 2009. ISSN 13672630. doi: 10.1088/1367-2630/11/6/065018.

M. Unger. Highlights from the Pierre Auger Observatory. *PoS*, ICRC2017:1102, 2018. doi: 10.22323/1.301.1102. [35,1102(2017)].

M. Unger, G. R. Farrar, and L. A. Anchordoqui. Origin of the ankle in the ultrahigh energy cosmic ray spectrum, and of the extragalactic protons below it. *Phys. Rev.*, D92(12):123001, 2015. doi: 10.1103/PhysRevD.92.123001.

A. Van Der Woude. Giant resonances. *Progress in Particle and Nuclear Physics*, 18:217–293, 1987. ISSN 0146-6410. doi: https://doi.org/10.1016/0146-6410(87)90011-1. URL http://www.sciencedirect.com/science/article/pii/0146641087900111.

D. Veberic, editor. *The Pierre Auger Observatory: Contributions to the 35th International Cosmic Ray Conference (ICRC 2017)*, 2017.

S. Vercellone. The next generation Cherenkov Telescope Array observatory: CTA. *Nuclear Instruments and Methods in Physics Research, Section A: Accelerators, Spectrometers, Detectors and Associated Equipment*, 766:73–77, 2014. ISSN 01689002. doi: 10.1016/j.nima.2014.04.015.

W. Wagner. Design and realisation of a new AMANDA data acquisition system with transient waveform recorders. In *Design and realisation of a new AMANDA data acquisition system with transient waveform recorders*, 2005.

S. Wanajo, H. T. Janka, and B. Müller. Electron-capture supernovae as the origin of elements beyond iron. *Astrophysical Journal Letters*, 726(2 PART II):2–5, 2011. ISSN 20418213. doi: 10.1088/2041-8205/726/2/L15.

S. Wanajo, Y. Sekiguchi, N. Nishimura, K. Kiuchi, K. Kyutoku, and M. Shibata. Production of all the r-process nuclides in the dynamical ejecta of neutron star mergers. *Astrophysical Journal Letters*, 789(2), 2014. ISSN 20418213. doi: 10.1088/2041-8205/789/2/L39.

S. Wanajo, B. Müller, H.-T. Janka, and A. Heger. Nucleosynthesis in the Innermost Ejecta of Neutrino-driven Supernova Explosions in Two Dimensions. *The Astrophysical Journal*, 852(1): 40, jan 2018. ISSN 1538-4357. doi: 10.3847/1538-4357/aa9d97. URL https://iopscience.iop.org/article/10.3847/1538-4357/aa9d97.

M. Wang, G. Audi, F. G. Kondev, W. J. Huang, S. Naimi, and X. Xu. The AME2016 atomic mass evaluation (II). Tables, graphs and references. *Chinese Physics C*, 41(3):030003, mar 2017. ISSN 16741137. doi: 10.1088/1674-1137/41/3/030003. URL http://stacks.iop.org/1674-1137/41/i=3/a=030003?key=crossref.cbf64c2ee5251915f252c1f31e5f8e05.

X.-Y. Wang and R.-Y. Liu. Tidal disruption jets of supermassive black holes as hidden sources of cosmic rays: Explaining the IceCube TeV-PeV neutrinos. *Phys. Rev. D*, 93(8):083005, Apr. 2016. doi: 10.1103/PhysRevD.93.083005.

D. Watson, C. J. Hansen, J. Selsing, et al. Identification of strontium in the merger of two neutron stars. *Nature*, 574(7779):497–500, 2019. ISSN 14764687. doi: 10.1038/s41586-019-1676-3. URL http://dx.doi.org/10.1038/s41586-019-1676-3.

E. Waxman and J. N. Bahcall. High-energy neutrinos from cosmological gamma-ray burst fireballs. *Phys. Rev. Lett.*, 78:2292–2295, 1997. doi: 10.1103/PhysRevLett.78.2292.

T. Weekes, H. Badran, S. Biller, I. Bond, S. Bradbury, J. Buckley, D. Carter-Lewis, M. Catanese, S. Criswell, W. Cui, and et al. VERITAS: the Very Energetic Radiation Imaging Telescope Array System. *Astroparticle Physics*, 17(2):221–243, May 2002. ISSN 0927-6505. doi: 10.1016/s0927-6505(01)00152-9. URL http://dx.doi.org/10.1016/S0927-6505(01)00152-9.

W. Weise. Hadronic aspects of photon-nucleus interactions. *Physics Reports*, 13(2):53 – 92, 1974. ISSN 0370-1573. doi: http://dx.doi.org/10.1016/0370-1573(74)90005-2. URL http://www.sciencedirect.com/science/article/pii/0370157374900052.

R. A. M. J. Wijers and T. J. Galama. Physical parameters of GRB 970508 and GRB 971214 from their afterglow synchrotron emission. *Astrophys. J.*, 523:177–186, 1999. doi: 10.1086/307705.

G. T. Zatsepin and V. A. Kuzmin. Upper limit of the spectrum of cosmic rays. *JETP Lett.*, 4: 78–80, 1966. [Pisma Zh. Eksp. Teor. Fiz.4,114(1966)].

B. T. Zhang, K. Murase, F. Oikonomou, and Z. Li. High-energy cosmic ray nuclei from tidal disruption events: Origin, survival, and implications. *Phys. Rev. D*, 96:063007, Sep 2017. doi: 10.1103/PhysRevD.96.063007. URL https://link.aps.org/doi/10.1103/PhysRevD.96.063007.

W. Zhang, S. E. Woosley, and A. I. MacFadyen. Relativistic Jets in Collapsars. *The Astrophysical Journal*, 586(1):356–371, mar 2003. ISSN 0004-637X. doi: 10.1086/367609. URL https://iopscience.iop.org/article/10.1086/367609.

Appendix A

Empirical formulas

A.1 Photomeson model based on empirical formulas

To construct the photomeson model it is necessary to obtain for each nuclear species j:

- $\sigma_j = \sigma_j(\epsilon_r)$ the absorption photonuclear cross section as function of the photon energy in the nucleus rest frame ϵ_r.
- $\sigma^{\rm incl}_{j\to k} = \sigma^{\rm incl}_{j\to k}(\epsilon_r)$ the inclusive photonuclear cross section for producing each of the k-th possible product particles (pions, nucleons, nuclear fragments).

The form of sigma$_j$ in the EM model is presented in Section 4.2.1 and summarized in Tab. 4.1. The expressions for the inclusive cross sections are presented in Section 4.2.2 for pions and in Section 4.2.3 for nucleons and nuclear fragments. The following sections detail the calculation of $\sigma^{\rm incl}_{j\to k}$ for nuclear fragments. The energy redistribution of the secondaries is calculated using Eq. 4.2 for the fragments of the nuclear remnant, while for direct interactions of the photon with a nucleon it is obtained from SOPHIA using Eq. 3.20 (see Appendix A.1.2).

A.1.1 Formulas for the inclusive cross sections

The inclusive cross sections for producing nucleons and nuclear fragments are based on the formulas discussed in sections below. The following relations are used in our model:

$$\sigma^{\rm incl}_{j\to {\rm p}} = \sigma^{\rm dir}_{\rm p} + \sigma^{\rm sp}_{\rm p} \ , \tag{A.1}$$

$$\sigma^{\rm incl}_{j\to {\rm n}} = \sigma^{\rm dir}_{\rm n} + \sigma^{\rm sp}_{\rm n} + \sum_{x=2}^{x_{\rm max}} x\sigma^{\rm mul}_{x{\rm n}} \ , \ \ x_{\rm max} = \lfloor 1.4\, A^{0.457} \rfloor \ , \tag{A.2}$$

$$\sigma^{\rm incl}_{j\to k} = \begin{cases} \sigma^{\rm dir}_{\rm p} & \text{for nucleus } k = (Z-1,\ A-1) \\ \sigma^{\rm dir}_{\rm n} & \text{for nucleus } k = (Z,\ A-1) \\ \sigma^{\rm mul}_{x{\rm n}} & \text{for nucleus } k \in (Z,\ A-x) \\ \sigma^{\rm sp}_{k} & \text{for nucleus } k \in (Z_k \in [1,...,Z-1],\ A_k \in [1,...,A-2]) \end{cases} , \tag{A.3}$$

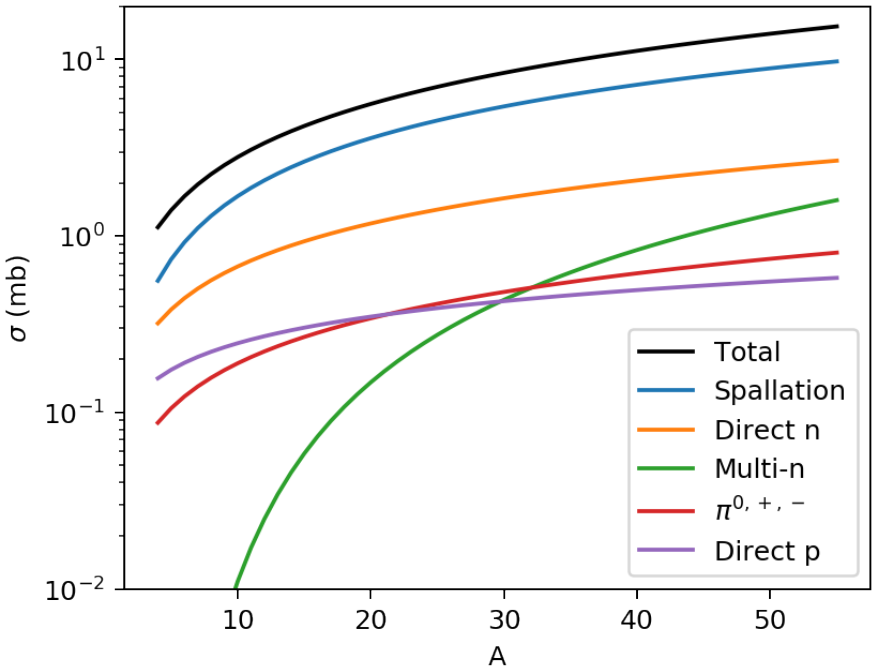

Figure A.1: Cross sections (in milibarn) versus the mass of the interacting nucleus A, for the relevant processes included in the EM. This is a partial reproduction of Fig. 8 by Terranova and Tavares (1994).

where the expressions for $\sigma_{\mathrm{p}}^{\mathrm{dir}}$, $\sigma_{x\mathrm{n}}^{\mathrm{dir}}$, $\sigma_{\mathrm{n}}^{\mathrm{mul}}$, and σ_{k}^{sp} are obtained using empirical relations, derived from data in the energy range $0.2 - 1\,\mathrm{GeV}$ by Terranova and Tavares (1994). Here we adapt the naming convention and remark that these relations do not correspond to the microscopic nuclear processes, but instead give a reasonable representation of data.

For simplicity and due to the sparsity of data, we assume they hold constant for all photon energies in the photomeson regime (see Figure 4.2). Below are the processes and their expressions reproduced from Terranova and Tavares (1994):

- **Direct proton production ($\sigma_{\mathrm{p}}^{\mathrm{dir}}$)** Reactions producing only one proton (γ, p) and a residual nucleus of mass $A - 1$:

$$\sigma_{\mathrm{p}}^{\mathrm{dir}} = 0.078\, A^{0.50}\ \mathrm{mb}\ . \tag{A.4}$$

- **Direct neutron production ($\sigma_{\mathrm{n}}^{\mathrm{dir}}$)** Reactions producing only one proton (γ, n) and a

residual nucleus of mass $A-1$:

$$\sigma_{\rm n}^{\rm dir} = 0.104\,A^{0.81}\ {\rm mb}\ . \tag{A.5}$$

- **Multi-neutron production ($\sigma_{x\mathbf{n}}^{\mathbf{mul}}$)** Reactions producing $x>1$ neutrons (γ, xn) and the corresponding residual nucleus with mass A $-$ xn:

$$\sigma_{\rm ntot}^{\rm mul} = \sum_{x=2}^{x_{\rm max}} \sigma_{x\rm n}^{\rm mul}\ {\rm mb},\ \ \text{where } x_{\rm max} = \lfloor 1.4\,A^{0.457} \rfloor \text{ and} \tag{A.6}$$

$$\sigma_{x\rm n}^{\rm mul} = 0.187\,A^{0.684}\,e^{-37\,A^{-0.924}\,(x-1)^{5/4}}\ {\rm mb}\ . \tag{A.7}$$

- **Spallation ($\sigma_{x\mathbf{p},\,y\mathbf{n}}^{\mathbf{sp}}$)** Spallation reactions where a nominal loss of $x>1$ protons and $y>1$ neutrons occurs ($\gamma, x{\rm p}+y{\rm n}$) and the corresponding residual nucleus with mass $A_r = A - x{\rm p} - y{\rm n} \geq A/2$ is produced:

$$\sigma_{x{\rm p},\,y{\rm n}}^{\rm sp} = 15.7\,{\rm E}^{-1.356}\,e^{-3.03\,{\rm E}^{-1.06}(x-1)-0.466\,(x-C\,\alpha\,y)^2}\ {\rm mb}\ ,\ \textit{where} \tag{A.8}$$
$${\rm E} = 446/{\rm A}\ ,\ C\ =\ 2.3\,\alpha - 1.044\ ,\ \text{and } \alpha = Z/(A-Z)\ .$$

- **Pion production ($\sigma_{\pi}^{\mathbf{prod}}$)** Reactions producing pions (π^0, $\pi+$, π^-) and one nucleon (γ, $\pi+\mathcal{N}$). This contribution is only used in the EM for normalizing the spallation in Eq. A.10. The relations for pion production in the EM are discussed in Section 4.2.2:

$$\sigma_{\pi}^{\rm prod} = 0.027\,A^{0.847}\ {\rm mb}\ . \tag{A.9}$$

- **Fission** It is only important for nuclei with mass above the Iron ^{56}Fe). It estimated from theoretical considerations since there is no exclusive experimental data for this process (Terranova and Tavares, 1994).

These relations are represented graphically in Figure A.1, except for the spallation curve which is strongly dependent on the mass and nucleons emitted, thus $\sigma^{\rm sp}$ is represented as the remainder of the total cross section $\sigma^{\rm tot} = 0.28A$ mb Terranova and Tavares (see 1994) after subtracting all contributions

$$\sigma^{\rm sp} = \sigma^{\rm tot} - \left(\sigma_{\pi}^{\rm prod} + \sigma_{\rm p}^{\rm dir} + \sigma_{\rm n}^{\rm dir} + \sigma_{\rm ntot}^{\rm mul}\right)\ . \tag{A.10}$$

To obtain the inclusive cross sections used in EM it is necessary to multiply the formulas above by the number of respective particles produced. For example, in the inclusive contributions

from direct proton and direct neutron production ($\sigma_{\mathrm{p}}^{\mathrm{dir}}$ and $\sigma_{\mathrm{n}}^{\mathrm{dir}}$) only one nucleon and one large fragment ($Z-1$, A) or (Z, $A-1$) are produced. In the case of the multi-neutron process the cross section $\sigma_{x\mathrm{n}}^{\mathrm{mul}}$ for the emission of x neutrons contributes to the inclusive cross section for neutron emission as $x\sigma_{x\mathrm{n}}^{\mathrm{mul}}$ (see Eq. A.2), *i.e.* :

$$\sigma_{\mathrm{n}}^{\mathrm{mul}} = \sum_{x=2}^{x_{\max}} x\sigma_{x\mathrm{n}}^{\mathrm{mul}} \ . \tag{A.11}$$

In the case of spallation, only one fragment species k with mass $A/2 \leq A_k \leq A-2$ is produced and the inclusive cross section is just $\sigma_{x\mathrm{p}y\mathrm{n}}^{\mathrm{sp}}$. We have made additional considerations to group the produced nucleons (x protons and y neutrons) into fragments with masses $A_k \in [1..4]$

$$\sigma_k^{\mathrm{sp}} = \begin{cases} \sigma_l^{\mathrm{sp}} & A_k \in [1...4] \\ \sigma_{x\mathrm{p},\,y\mathrm{n}}^{\mathrm{sp}} & A_k \in [A/2...A-2] \end{cases} \ . \tag{A.12}$$

Where σ_l^{sp} stands for any light fragment produced ($\sigma_{\mathrm{n}}^{\mathrm{sp}}$, $\sigma_{\mathrm{p}}^{\mathrm{sp}}$, *etc.*). The method of estimating σ_l^{sp} is discussed in the following subsection.

A.1.2 Inclusive cross section of small fragments

In the processes considered in Section A.1.1 no fragments with masses smaller than $A/2$ are created. We assume for the EM that nucleons produced in the spallation process can be grouped into fragments of no more than four nucleons and estimated the number of those fragments with thermostatistical formulas (Cole, 2010).

For any spallation event i a number of x protons and y neutrons is lost from the interacting nucleus (Z, A) with an exclusive cross section $\sigma_{x\mathrm{p}y\mathrm{n}}$ (which in the following will be labeled as σ_i^{sp}). We consider that the total energy of left from the interaction is taken by the spalled nucleons as their kinetic energy (no internal excitation of products). The spalled nucleons can be configured in a number of small fragments, or a combination r:

$$\mathrm{C}_i^r = \left\{ \mathrm{N}_{i,\mathrm{n}}^r, \mathrm{N}_{i,\mathrm{p}}^r, ..., \mathrm{N}_{i,l}^r, ..., \mathrm{N}_{texti,\{\}alpha}^r \right\} \ \ l \in (Z_l, A_l), \ \ 1 \leq A_l \leq 4 \ , \tag{A.13}$$

where l refers to any of the nuclear species with no more than four nucleons and with a decay half life longer than the relevant timescale of the astrophysical (only common isotopes remain).

The set of all possible $\mathbb{C}_i = \{\mathrm{C}_i^r\}$ is determined by finding all mixtures of species l in the quantities $\mathrm{N}_{i,l}^r$ such that the proton and nucleon number of the combination matches the spalled

numbers:

$$x = Z_i = \sum_{\mathrm{C}_i^r} Z_l \mathrm{N}_{i,l}^r \ , \tag{A.14}$$

$$x + y = A_i = \sum_{\mathrm{C}_i^r} A_l \mathrm{N}_{i,l}^r \ . \tag{A.15}$$

An appropriate weight for each combination $\mathrm{P}_{i,r}$ allows to find the numbers of particles produced in each spallation event i with

$$\mathrm{N}_{i,l} = \sum_r \mathrm{N}_{i,l}^r \mathrm{P}_{i,r} \ . \tag{A.16}$$

By summing the numbers of particle l over all spallation configurations, the total inclusive cross section of spallation for particle l is obtained

$$\sigma_l^{\mathrm{sp}} = \sum_i \mathrm{N}_{i,l} \ \sigma_i^{\mathrm{sp}} \ , \quad l \in \mathbb{S} \ . \tag{A.17}$$

The following section details the estimation of the combination weights $\mathrm{P}_{i,r}$.

A.1.3 Evaluation of the weights of combinations

The simplest assumption is that all combinations are equiprobable, that is they all have the same weight $\mathrm{P}_{i,r} = \mathrm{P}_i$. Then the number of particles of species l (Eq. A.16) results

$$\mathrm{N}_{i,l} = \mathrm{P}_i \sum_r \mathrm{N}_{i,l}^r \ , \tag{A.18}$$

and the P_i can be found from the nucleon conservation. This means that the number of nucleons produced in all spallation events is equal to the nucleons present in the interacting nucleus

$$A \sum_i \sigma_i^{\mathrm{sp}} = \sum_k A_k \sigma_k^{\mathrm{sp}} \ , \tag{A.19}$$

where σ_k^{sp} are those in Eq. A.12 and Eq. A.17 with Eq. A.18.

The equiprobability assumption fails to account for the fact that combinations with more stable nuclei are more likely to occur. In the EM we apply statistical mechanics, assuming that the combinations are possible microstates corresponding to a certain spallation event (macrostates) within the Grand Canonical distribution. A general form of the partition function in this case

is (Cole, 2010)

$$\mathsf{Z} = \sum_{i,r} e^{-\beta(\epsilon_i - \mu n_r)} \,, \tag{A.20}$$

where ϵ_i is the energy of the macrostate, μ is the chemical potential of the elements (here only one species is included) and n_r the number of elements of a given microstate. The weight of a microstate can be expressed by the probability of the microstate

$$\mathrm{P}_{i,n} = e^{-\beta(\epsilon_i - \mu n_r)}/\mathsf{Z} \,, \tag{A.21}$$

We are interested in the relative weights of different microstates with the same energy ϵ_i since we use the normalization condition Eq. A.19. Hence, the expression for $\mathrm{P}_{i,n}$ can be rewritten grouping the factors common to a macrostate i into some normalization constant B_i

$$\mathrm{P}_{i,n_r} = \mathsf{B}_i e^{\beta \mu n_r} \,, \tag{A.22}$$

which allows estimating the weights of the macrostates without calculating the partition function. Considering each nuclear species l as a different constituent of the system, the chemical potential associated will be its ground state energy $\mu_l = m_l$ (rest mass in units of energy) which can be found in nuclear mass tables. Then the required expression of $\mathrm{P}_{i,r}$ is

$$\mathrm{P}_{i,r} = \mathsf{B}_i e^{\beta \sum\limits_l \mu_l \mathrm{N}^r_{i,l}} \,, \tag{A.23}$$

where the normalization constants B_i are found using Eq. A.19. The expression chosen for β_i is commonly used for nuclei (Cole, 2010)

$$\beta = \sqrt{\frac{A}{8\bar{\epsilon^*}}} \,, \tag{A.24}$$

where the excitation energy $\bar{\epsilon^*}$ was chosen as the average photon energy in the range where the spallation formula was obtained

$$\bar{\epsilon^*} = \int_{0.1\ \mathrm{GeV}}^{1\ \mathrm{GeV}} \sigma_j(\epsilon_r)\epsilon_r d\epsilon_r \Big/ \int_{0.1\ \mathrm{GeV}}^{1\ \mathrm{GeV}} \sigma_j(\epsilon_r) d\epsilon_r \,. \tag{A.25}$$

Appendix B

Comparing photon models

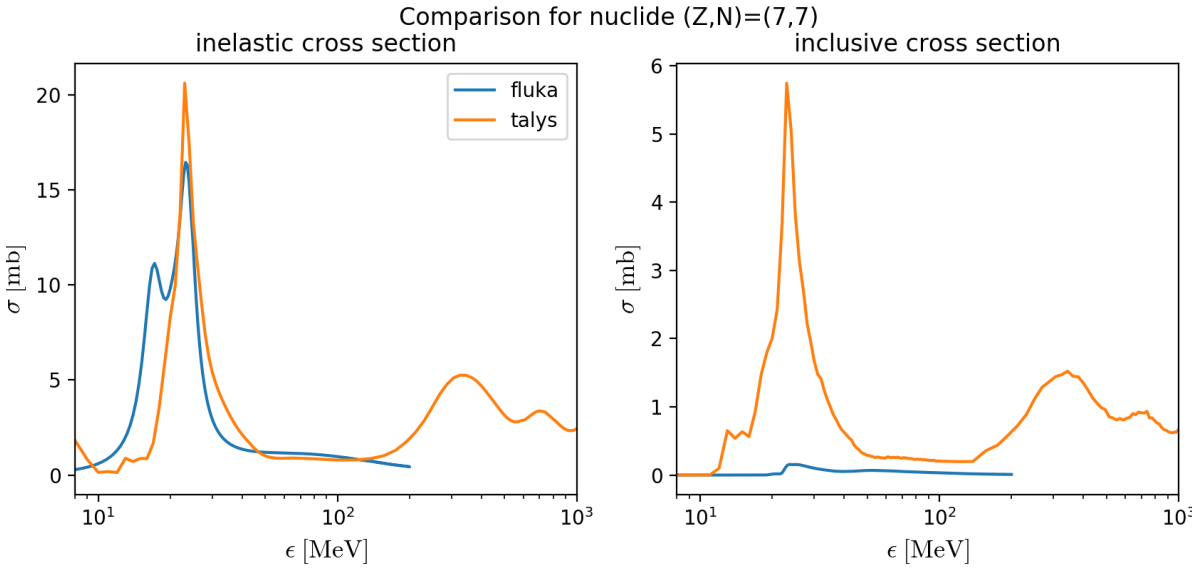

Figure B.1: Comparison of photon models created using TALYS and FLUKA : nucleus ^{14}N (below).

The models for photoproduction in photonuclear interactions are presented in Chapter 5. Two of the models are based on nuclear interaction codes: TALYS and FLUKA . The nuclei available and the photon interaction ranges differ; however, for the ranges in common the outputs should be comparable, if not identical. Figures B.1-B.4 illustrate the important differences between the models with the inelastic and the inclusive cross sections for photoproduction. The ratio of inclusive to inelastic gives the multiplicity of photons M_γ. The nuclides chosen are all stable, and expected to be abundant in astrophysical scenarios. The inelastic cross sections differ between models from just below two up to almost six times in the GDR peak, with very different shapes. The inclusive cross sections differ in a factor from just below two up to almost thirty in the GDR peak, also with striking shape differences. The multiplicities of photons also vary considerably with the range $M_\gamma = 0.3 - 3$ for TALYS and the range $M_\gamma = 0.1 - 0.3$ for FLUKA .

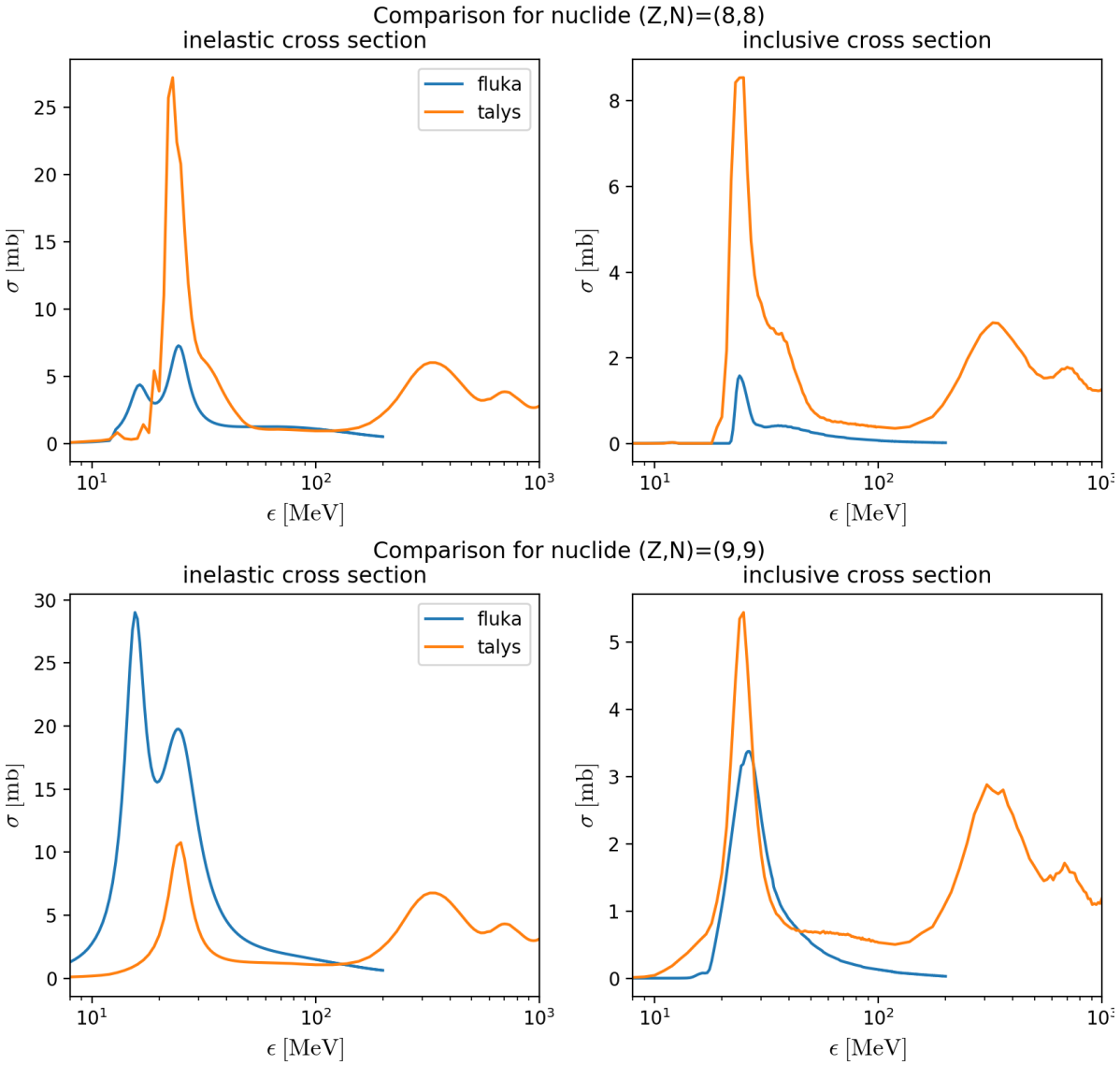

Figure B.2: Comparison of photon models created using Talys and Fluka : nuclei ^{16}O (above) and ^{18}F (below).

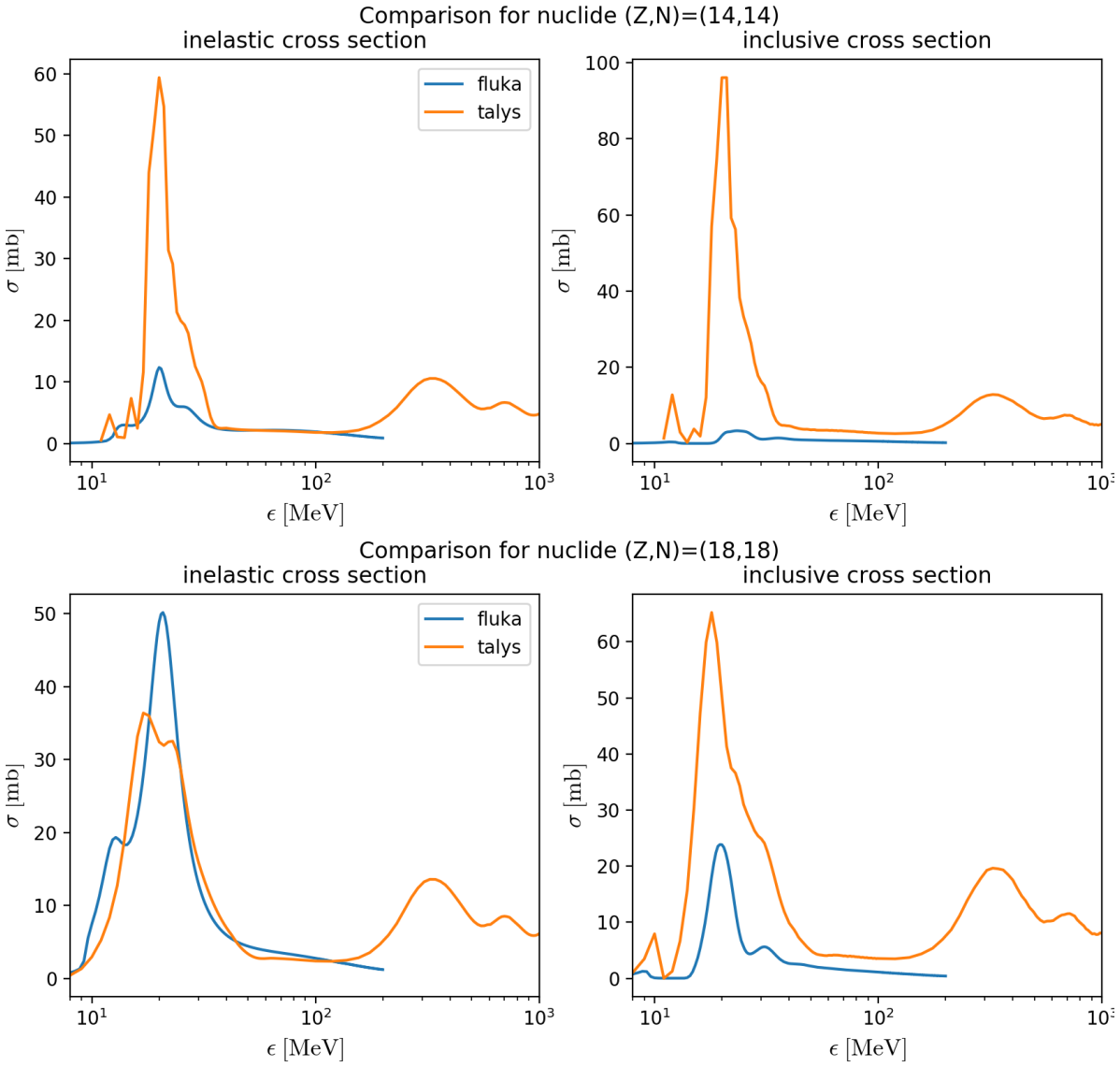

Figure B.3: Comparison of photon models created using TALYS and FLUKA : nuclei ^{28}Si (above) and ^{36}Ar (below).

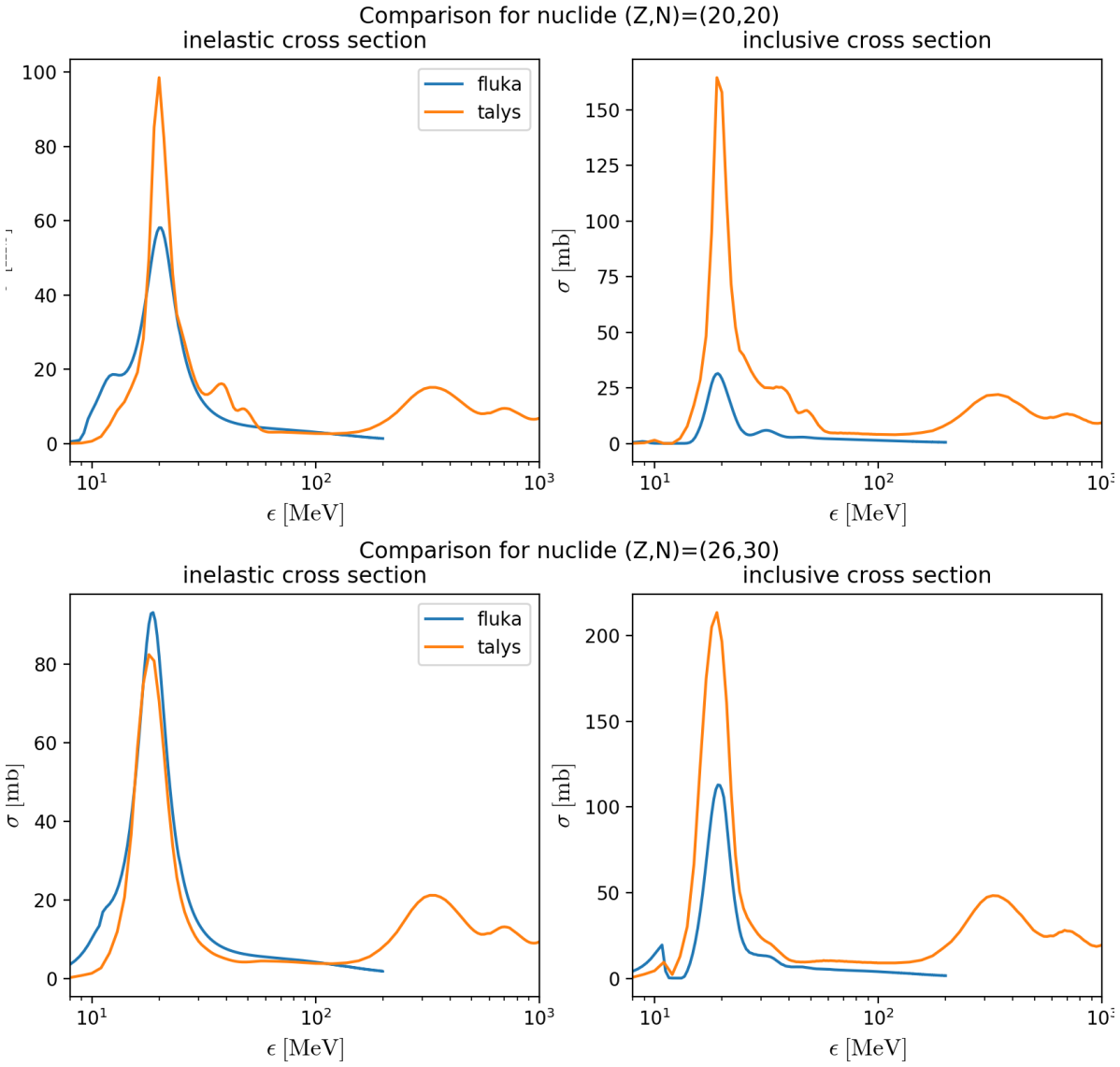

Figure B.4: Comparison of photon models created using Talys and Fluka : nuclei ^{40}Ca (above) and ^{56}Fe (below).